Politecnico di Milano

SCHOOL OF INDUSTRIAL AND INFORMATION ENGINEERING
Master of Science – Aeronautical Engineering

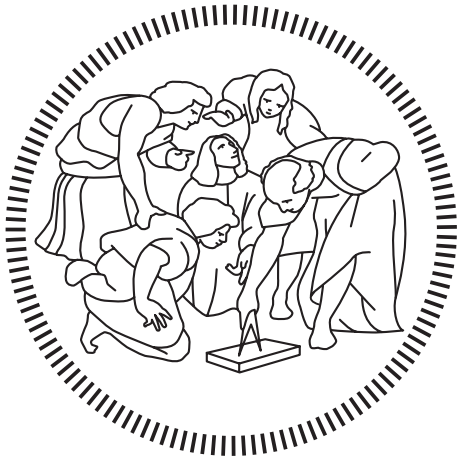

CFD modelling of conventional trains under crosswind conditions

Supervisor
Prof. PAOLO SCHITO

Co-Supervisor
ELIA BRAMBILLA

Candidate
JUAN DÍAZ ARTEAGA – 915767

Academic Year 2020 – 2021

To my parents...

Abstract

With the improvement in railway technology, trains are becoming faster and lighter, thus increasing the risk of overturning under crosswind conditions. CEN standards for railway aerodynamics (EN14067-6) were developed to cope for open track phenomena affecting railway vehicles, crosswind among others, in pursuit of Virtual Homologation (VH). To approach these challenges, guidelines on wind tunnel testing or Computational Fluid Dynamic methodologies are established. Characteristic Wind Curves (CWC) condition vehicle's lateral stability and are obtained by computing the aerodynamic moment and forces coefficients ($C_{MX,lee}$, C_{Mx}, C_{FY} and C_{FZ}). The motivation of this thesis lays on proving whether a CFD model validated with high-speed train models given in CEN norms, fulfils as well standards' $\epsilon < 15\%$ restriction. In order to achieve this, numerical simulations are performed with the open source software: OpenFOAM. RANS model in conjunction with $k - \omega$ SST turbulence model is used. Then, a sensitivity mesh analysis is accomplished to determine the best size/accuracy relationship for the grid, where ETR500 results are compared to standards to validate the model. This model is then used to study other three conventional trains: Vivalto, Regionale and Intercity. CFD results where norm compliance ($\epsilon < 15\%$) for yaw angles (β) below 30 degrees. For greater angles, inherent unsteadiness of the problem limits RANS accuracy. In the case of small β angles similar behaviour among trains was shown, where magnitude of the lateral force coefficient was directly related with vorticity magnitude of the flow at the leeward side. Vortical structures depended on nose shape, fairing geometry and underfloor bypass ratio (BPR_{eff}). For high values of β angle, trains could be grouped in two clusters depending on whether $C_{MX,lee}$ value dropped (group 1) or remained constant (group 2) with increments in yaw angle. The behaviour proved to depend on the value of (BPR_{eff}), where group 1 had a value below 1 and group 2 a value above. Lastly, minimum CEN guidelines showed not to be sufficient for conventional trains to comply with the standards in the whole range of yaw angles.

Keywords: Computational Fluid Dynamics; Crosswind; CEN; Conventional train; Virtual Homologation; Yaw angle; RANS simulation; BPR_{eff};

Acknowledgements

I would really like to appreciate my supervisor, professor Paolo Schito, for his continuous help, suggestions for improvement, kindness, great availability and comprehension from the very beginning. To Elia Brambilla, who has taught me from the start, always available to listen and to give me advices that have played a key roll in the success of this thesis. To my family for all the relentless effort that have put into my education and the priceless support I have received from them ever since. And to all my closest friends and people that have encourage me through out the years to always give my best and pursue my goals. To all of you. Thank you.

Contents

List of Figures

List of Tables

Chapter 1

Introduction and project objectives

1.1 Introduction

For the past decades and with the increase in global mobility, optimization of diverse means of transportation has become of utter importance. In particular, trains have gained a lot of presence in Europe and Eastern Asia and, with its development, the focus has been centred in obtaining faster vehicles.

This outbreak of high-speed trains has made engineers to study in more depth the aerodynamics concerning this mean of transportation, and with it, the necessity of increasing its safety.

In order to do so, defining a standard became of paramount importance, so for the past twenty years, many different projects have been accomplished to study the different aerodynamics phenomenon concerning railway transport. Specifically, *crosswind*, *slipstream*, *ballast lifting*, *tunnel overpressure* or *pressure pulse* are some of the effects that have been considered.

Regarding Europe, CEN standards [12] were established due to this necessity of increasing safety together with other specific rules, as for instance, train interoperability as stated in the *Technical Specification for Interoperability* (TSI) [17].

Moreover, these aerodynamic phenomenon were studied in projects like TRANSAERO (Transient Aerodynamics for Railway System Optimisation) [18], *Aerodynamic in Open Air* (AOA), or *AeroTRAIN* [19].

Normally these studies were conducted at full scale testing, wind tunnel testing and Computational Fluid Dynamics (CFD) testing [2]. Each methodology has its owns advantages and disadvantages, but they have achieved levels where many manufacturing companies are encouraging for developing Virtual Homologation which translates into saving time, resources and money.

CEN standards were developed studying high speed trains and its behaviour. Thus, theses guidelines already established are meant to work for high-speed railway vehicles, but it has not been proven whether they would serve as well or not for conventional trains.

1.2 Motivation

Crosswind conditions in railway vehicles is a very complex phenomenon which is yet far from being completely understood. Historically, it was not much of a concern since traction was fully carried by the locomotive, making the leading car a very heavy vehicle. Nowadays, it is not the case any more and thus, it has become of utter importance to understand its behaviour.

As stated in section 1.1, virtual homologation for trains has been thoroughly sought through out the years as it helps companies to highly reduce costs and time in the process of certification. This is achieved by means of less costly methodologies like wind tunnel testing or CFD tools. In CEN norms, guidelines to assess the crosswind problem for every type of train are given. CFD models developed are then validated by comparing the results to high-speed trains data stated in the standards.

Therefore, this project is then born with the goal of verifying the viability of being norm compliance (i.e. error below 15%) with conventional railway vehicles after having validated the CFD model with high-speed trains.

1.3 Objectives

The fulfilment of the following objectives will determine the success of this thesis. Namely, the main goals are:

1. Develop a CFD model based on CEN standards.
2. Validation of the model obtained.
3. Study different conventional train models and compare the results with experimental wind tunnel data.

1.4 Methodology

The working methodology used to achieve the objectives previously stated will consist on the following tasks:

- **Task 0**: Obtain previous knowledge to learn how to use the different softwares needed.
  - **Task 0.1**: Learn how to code in OpenFoam.
  - **Task 0.2**: Learn how to use Paraview for the qualitative post processing analysis.
- **Task 1**: Develop the CFD model according to EN norms.

  - **Task 1.1**: Treatment of the ETR500 geometry in a CAD software, in this case, SolidWorks.
  - **Task 1.2**: Develop 4 different meshes in OpenFoam with block Mesh and Snappy mesh.
  - **Task 1.3**: Sensitivity analysis for a yaw angle of 30 degrees using a Raynolds Averaged Navier Stokes equations approach with a kω-SST model for turbulence.

- **Task 2**: Comparison of CFD results with experimental data to validate the model. Error of moment and force coefficients must be below a 15% range according to CEN standards [12].

  - **Treatment of the results with MATLAB for the quantitative analysis.**
  - **Treatment of the results with Paraview for the qualitative comparison.**

- **Task 3**: Make the CFD study of crosswind for different conventional trains.

  - **Task 3.1**: Prepare all the different CAD geometries.
  - **Task 3.2**: Make the computations needed to obtain the results for different yaw angles (0, 10, 20 and 30).
  - **Task 3.3**: Compare CFD results with wind tunnel data to analyse the validity of the model.

- **Task 4**: Drafting of the document.

  - **Task 4.1**: Abstract and introduction.
  - **Task 4.2**: State of the Art.
  - **Task 4.3**: CFD simulation.
  - **Task 4.4**: CFD results analysis.
  - **Task 4.5**: Conclusions.

Chapter 2

State of the art

2.1 Crosswind phenomenon

The understanding of the crosswind problem is of utter importance, as it is the main condition that will be analysed and treated throughout the whole thesis. It is a crucial factor concerning the aerodynamics of a railway vehicle and awareness of its effects has increased during the last 15 years.

In fact, overturning accidents are the main motivation to study it, as there has been 29 wind-induced accidents [20] of trains since this kind of transport began back in Japan in 1872.

Figure 2.1. Accidents crosswind related.

Crosswind effect has a crucial influence in the lateral behaviour of the train, producing a rolling moment which could potentially induce an unloading of the

windward wheels. This effect could be even exacerbated while taking a turn as centrifugal forces sum up to crosswind forces. The limits regarding crosswind stability are synthesized in curves called *Characteristic Wind Curves* (CWC), which relates train velocity with respect to wind velocity. In turn, it defines a maximum speed for the vehicle for a given wind speed value that the car can withstand before the windward wheels unload.

Figure 2.2 shows an example of a Characteristic Wind Curve. The region above the curve becomes the unstable area and the region below the stable. To obtain the CWC of a particular vehicle, aerodynamic forces should be modelled, vehicle dynamic response shall be computed and a parametric study to observe limit conditions must be performed [2].

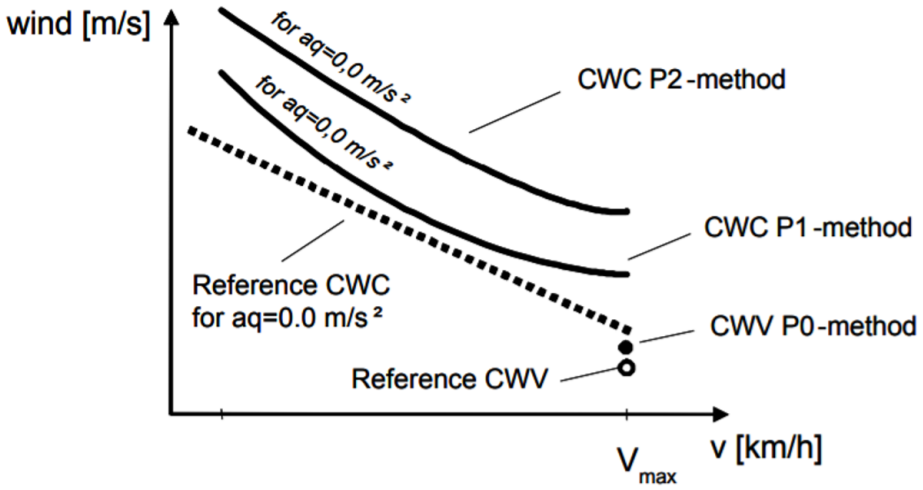

Figure 2.2. Example of CWC [1]

In figure 2.3, crosswind phenomenon is synthesized with a speed vector diagram. The vehicle moves forward with velocity V_{tr} while V_w stands for wind velocity. Wind angle measured with respect to the trajectory of the train is β_w, while the effective velocity seen by the train is the relative motion composed by train's velocity and wind's velocity vectors. This relative velocity (V_{rel}) forms an angle relative to the track β called *Yaw angle*.

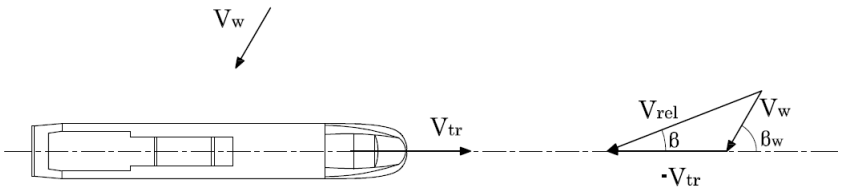

Figure 2.3. Speed vector diagram for crosswind conditions [2]

Once the nature and variables of the problem are known, the aerodynamic coeffi-

cients can be computed analytically according to equations 2.1 and 2.2.

$$F_i = \frac{1}{2}\rho A C_i(\beta) V_{rel}^2 \quad i = x, y, z \tag{2.1}$$

$$M_i = \frac{1}{2}\rho A d C_{Mi}(\beta) V_{rel}^2 \quad i = x, y, z \tag{2.2}$$

where ρ stands for air density, A is the characteristic area, d the characteristic length, C_i is the dimensionless aerodynamic coefficient for the *i-th* force, β is the yaw angle, V_{rel} the relative velocity seen by the train and C_{Mi} is the dimensionless aerodynamic coefficient for the *i-th* moment. In addition, A and d are assigned in [12] $10m^2$ and $3m$ respectively as reference values.

There are different ways to approach the estimation of moments and forces coefficients [12]. As an example, analytical predictive equations may be used. For instance, [21] applied different analytical wind models like Chinese Hat gust wind model to compute CWC. Though, restrictions regarding shape, leading end cars length or standard track gauge must be met. Then, for those cases where the problem can be tackled analytically, wind loads can be obtained from equation 2.3. Where all the parameters are given in Table 3, page 15 of [12].

$$C_{Mx,lee}(\beta) = \frac{\left(z_0 + z_1 \cdot \tilde{\beta} + z_2 \cdot \tilde{\beta}^2 + z_3 \cdot \tilde{\beta}^3\right) \cdot h_{VEH}^2 \cdot L_{VEH} \cdot f_L \cdot f_{VEH} \cdot z_4}{A_0 \cdot d_0} \tag{2.3}$$

$$with \quad \tilde{\beta} = |\arctan[\tan(\beta \cdot z_5)]| \tag{2.4}$$

It is a good and easier way of obtaining a first estimation for the coefficients. However, usually greater precision is needed and so, more complex methodologies as experimental tests (wind tunnel) or lately, CFD techniques are used. Hence, a better understanding of the latter tools will be provided in sections 2.3 and 2.4.

Regarding qualitative comprehension of crosswind phenomenon, many are the studies [3, 9, 22, 23] that can be found in the literature which explain the aerodynamic behaviour of the flow, usually for high speed trains, at a wide variety of yaw angles (normally from 0 to 90 degrees). Although the main flow field structures are known, there is very little on quantifying or understanding how these vortical structures form.

In figure 2.4, the main behaviour is presented. Typically, for small yaw angles (<30 degrees) [23], the body behaves as a streamlined body and two vortices appear at the lower and upper frontal leeward edge of the leading vehicle. They move rapidly away from the train, allowing two new vortices to be formed. One appears at the upper part of the leeward edge, and the second one appears at the bottom leeward edge. These two vortex sheets wrap around each attached to the leeward face (bottom moves clockwise and upper anticlockwise) moving downstream together creating the main vortex.

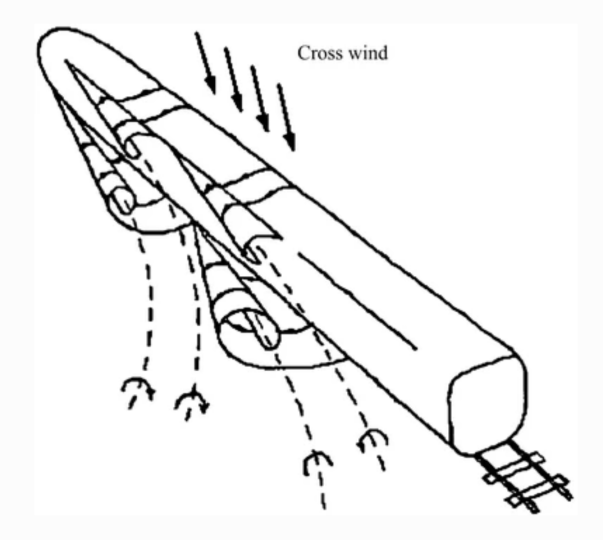

Figure 2.4. Vortical structures created under crosswind. Image reproduced from [3].

Moreover, for high yaw angles (greater than 60 degrees), the train behaves as a bluff body and a Von Kármán vortex street generates downstream as shown in figure 2.5.

In addition, it is worth recalling that is the front-end of a railway vehicle the one subjected to the highest aerodynamic loads [22], and hence, the most critical part of the train when analysing crosswind stability. This condition has worsen since traction has been transferred to every car, carrying a decrease in weight for the leading car and therefore, increasing the risk of unloading the wheels. Thus, its the critical part of the vehicle that should be studied.

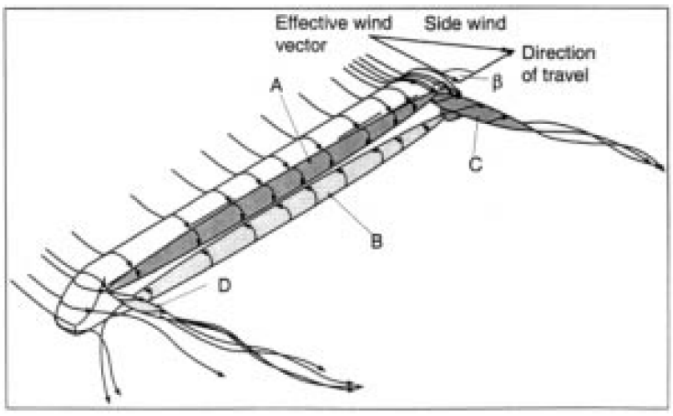

Figure 2.5. Flow structure for cross-flow case. Image reproduced from [3].

2.2 Norms and previous studies

In order to increase safety and establish a certain criteria to asses the crosswind phenomenon (among others), many studies where carried out by different companies and universities. Also not only to increase safety, but because of the increasing

connectivity between European countries, more specific rules were needed concerning every aspect that could affect, including aerodynamics. Hence, Technical Specification for Interoperability (TSI) [17] norms were developed in a way that became requirements that must be fulfilled by any new railway vehicle which is thought to run on the European high-speed line. Specifically, they define technical and operational standards that must be met by each subsystem or part of subsystem in order to meet the essential requirements and ensure the interoperability of the railway system of the European Union.

From there onwards, more projects began to pursue a deeper understanding in aerodynamic related issues. There was another experimental project called *TRANSAERO* (Transient Aerodynamics for Railway System Optimisation) [18]. In this case, three railway related companies, eight universities and some research institutions in Europe collaborated together to asses different aerodynamic phenomenon, crosswind among them.

Aerodynamics in Open Air (AOA) [24] followed same guidelines than TRANSAERO. Two topics were addressed in two sub-projects, namely underbody aerodynamics concerning ballast lifting and crosswind safety. The latter was becoming a sensitive issue for railways, not only for narrow gauge, but also as a latent endanger for high speed rail [25]. German-French cooperation "DEUFRAKO" exchanged methodologies for assessing cross-wind sensitivities of the TGV and ICE trains, generating an approach [26] for dealing with cross-wind risk. Some issues remained opened such as derivation of meteorological conditions, treatment of embankments, formulation of safety targets and the implications of cargo traffic. Hence, as vehicle and infrastructure have a direct impact on both problems (crosswind safety and underfloor aerodynamics), sharing knowledge between operators and manufacturers would allow a better understanding of the phenomenon. Therefore, nine partners from five European countries (Trenitalia, Alstom Transport SA, Bombardier or CAF among others) joined this research "Aerodynamics in Open Air" in cooperation to gain a deeper understanding on the matter.

The latest project regarding crosswind phenomenon took place in 2009 and received the name of *AeroTRAIN* [19]. Is part of a cluster of projects where *TrioTRAIN* is the name given to it. *AeroTRAIN*, *DynoTRAIN* and *PantoTRAIN* were the projects conforming it. The name is given by *Total Regulatory Acceptance for the Interoperable Network* and the main goal pursued was to develop new methodologies in the process of certification of railway vehicles in such a way that it could become a more affordable activity. Indeed, a large part of the certification process of a rail vehicle goes for testing safety, performance and to ensure infrastructure compatibility [27]. So, the objective was to speed up interoperable approvals by closing "open points" from the TSI.

In particular, *AeroTRAIN* project consisted in different packages that studied aerodynamic phenomenon related to train vehicles as: open air pressure pulses, aerodynamic loads on tracks, crosswinds, train-tunnel interaction or slip stream effect. Namely, Work Package 3 involving crosswind issues entailed the publication of three papers [28–30] where the first two call for CFD tools to predict cross wind loads, and the third present the results of a series of wind tunnel tests and computations that

quantify cross wind forces in a consistent way, and thus, the subsequent application of these forces to obtain wind characteristics.

All these projects and collaborations, made possible for the European Commission and the European Free trade Association, not only the creation of the European Standard EN 14067, which was established by the Technical Committee CEN/TC 256 "Railway Applications" in January 2010 [12], but also its continuous update and improvement. Nevertheless, although a substantial progress was achieved by *AeroTRAIN* project, more work remains to be done, specifically on ballast lifting and cross wind assessment issues [27].

2.3 Experimental approach

As seen in section 2.1, there are different ways to tackle the challenge of understanding cross wind related issues. At experimental level, tests can be performed at field with real vehicles or at wind tunnel facilities, being the latter the one normally used for crosswind testing. However, for other aerodynamic related challenges, real scale testing is normally used.

For crosswind, real scale testing becomes very challenging as variables like wind speed or yaw angle need to be under control. Hence, wind tunnel testing is preferred, as it allows researchers to control all these factors and many more, like turbulence intensity for instance. Some researches like [2, 5, 32] are great examples of crosswind testing at wind tunnels.

The procedure for crosswind experiments in wind tunnel go as follows:

1. Have a clear knowledge about the facility that is going to be used an its characteristics as not all of them produce the same boundary layer profile, have same dimensions or produce same turbulence intensity. For example, in figure 2.6 a longitudinal view of the wind tunnel at Politecnico di Milano is presented.

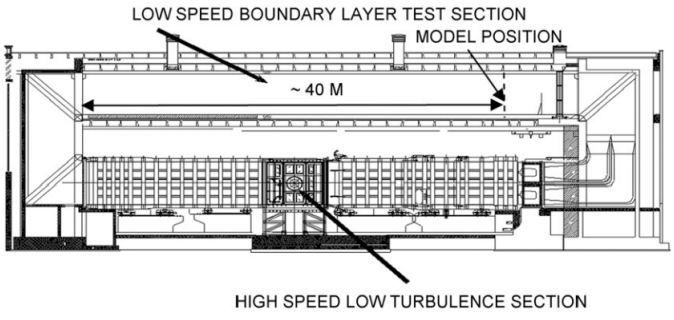

Figure 2.6. Longitudinal view of Politecnico di Milano's wind tunnel reproduced from [2]

   In this case, it is a closed circuit disposed vertically with two test chambers: a 4x4 m high-speed low turbulence section and a 14x4 m boundary layer test section [2]. These big sizes not found very commonly allow for very large scale models to be tested.

2. Verify Reynolds number independence. This means, that the model under study is tested at different speeds (i.e. Reynolds numbers) in order to check that vehicle's force coefficients are not affected or sensible to variations in incoming airspeed.

3. Then the geometry to study is selected. It might be different train models, their composition (leading car, bogies, pantographs,...), or external geometries like ballast and rail configuration, presence of embankment or any other geometry that may influence the crosswind analysis.

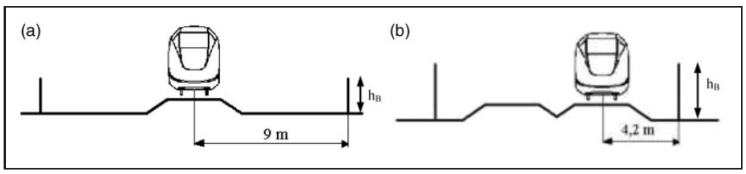

Figure 2.7. Wind tunnel tests scenarios: (a) (Single Track Ballast and Rail (STRB) and (b) Double Track Ballast and Rail (DTBR) reproduced from [5]

4. Proper instrumentation depending on the measurements pursued is placed. For instance in [2] only measurements are made for the leading car, while the trailing car is placed just to reproduce the proper boundary layer conditions. A balance is placed under ground in this case, protected from the wind. Then, it is connected directly to the model so that forces exerted on the vehicle are measured. Also, pressure taps are placed around the surface of the locomotive so that pressure field can be measured. An example of its distribution is shown in figures 2.8 and 2.9

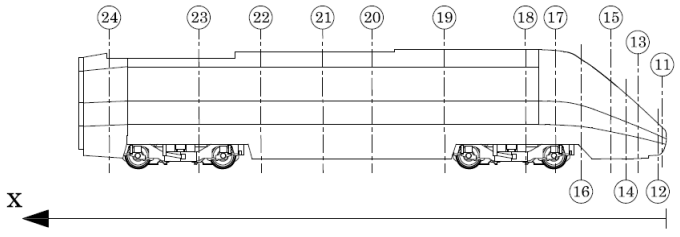

Figure 2.8. Pressure taps location along the longitudinal axis reproduced from [2]

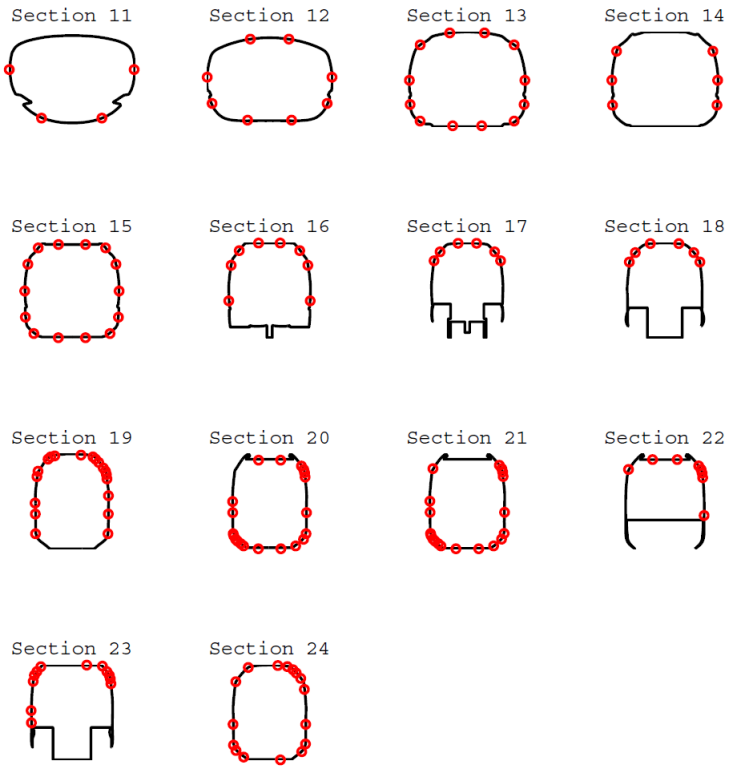

Figure 2.9. Position of pressure taps at each section reproduced from [2]

5. Then test are conducted as needed and post processing of the results is performed, where maybe modifications as, for instance, blockage corrections, are done.

It is worth highlighting as well that, although it does not imply usually crosswind tests, in others like slipstream, some times models are tested in moving rigs instead of still. In this way, relative motion between train and ground can be studied.

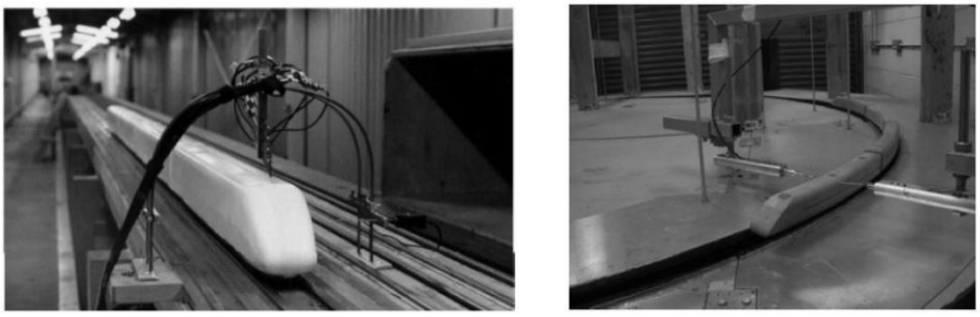

Figure 2.10. Examples of moving models reproduced from [6, 7]

Nevertheless, everything here exposed has to cope with some norms to ensure, at least, certain rigour. In particular, [12] EN14067-6 regulations must be followed. Just to get a deeper insight on what characteristics may be required, a few are listed below [12]:

- A block profile and low turbulence intensity to ensure more reliable and repeatable conditions between different wind tunnel operators.
- Measured test results for the benchmark vehicle $C_{Mx,lee,test}$ shall be compared with references values to determine validity of the results.
- Turbulence level must be ensured to be below $Tu_x \leq 0.025$.
- Total thickness of the boundary layer should be less than 30% of the vehicle height.
- For a characteristic length of 3m (divided by the scale of the model), Reynolds number should be greater than 2.5×10^5.
- Blockage ratio X_B is defined for a yaw angle equal to 30 degrees and it must be less than 15%.
- Ratio between total length of the train and wind tunnel width should not be so large so that no distortions are caused to the flow due to the presence of the walls.
- Regarding for instance measurement devices, its accuracy should be better than 2% and resolution better than 1%.
- Mean forces and moments should be measured using a force and moment balance. The accuracy of the rolling moment about the lee rail must have a precision of 5% for the lowest yaw angle needed for obtaining the CWC.

2.4 CFD approach

Computational Fluid Dynamics or CFD, is the last methodology hereby presented to obtain the aerodynamic coefficients for the characterisation of the CWCs. Wind tunnel testing allow more repeatable conditions and has its advantages already commented. However, other inconvenient exist as well. For instance, issues related to blockage effects that may lead to very small models, or the proper reproduction of the atmospheric boundary layer in way that may, for example, take into account relative motion between the train and the ground infrastructure. Also, it is an expensive technique and the information that may be obtained from the flow is limited to forces and pressure readings and flow visualization techniques.

Therefore, CFD has also its great advantages with respect to wind tunnel testing. In fact, more information may be deduced from post processing although, a proper modelling shall be done to obtain reliable data. That is why both methodologies are usually complementary to each other.

Regarding the modelling, it starts with the mesh to be used. In crosswind cases an asymmetric grid is developed. In [8] for instance, various refinement boxes were developed on the leeward side of the vehicle to capture better the vortical structures and the detachments of the flow. Figure 2.11 is an example of a mesh used.

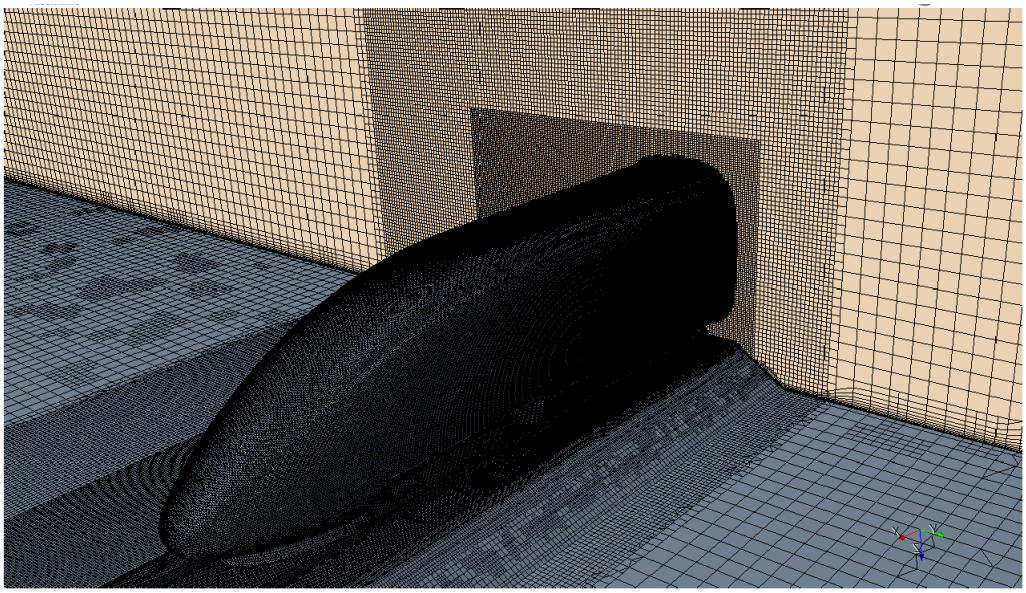

Figure 2.11. Train and STBR surface mesh of ICE3 reproduced from [8]

Then, there are many possibilities to address the problem from the mathematical point of view. Navier-Stokes equations for instance can be approach by means of RANS or URANS equations for instance. Also Detached Eddy Simulations (DES), Large Eddy Simulations (LES) or Direct Numerical Solver (DNS) are alternative strategies to tackle the CFD challenge. The flow around the vehicle is inherently unsteady, and varies with geometry and yaw angle. However, steady methods may be used if some steadiness is evident (for instance at low yaw angles).

Concerning turbulence modelling, many are the alternatives that exist (standard $k-\epsilon$, realizable $k-\epsilon$, $k-\omega$, $k-\omega$ BST, $k-\omega$ SST, etc). Depending on the technique used results and the physics of the problem will be captured with more or less accuracy.

In figure 2.12, iso-surfaces of $\lambda 2$ are shown for the same train and same environmental conditions, only modelling methodology is changed. Thus, it can be seen that results may differ in a substantial way.

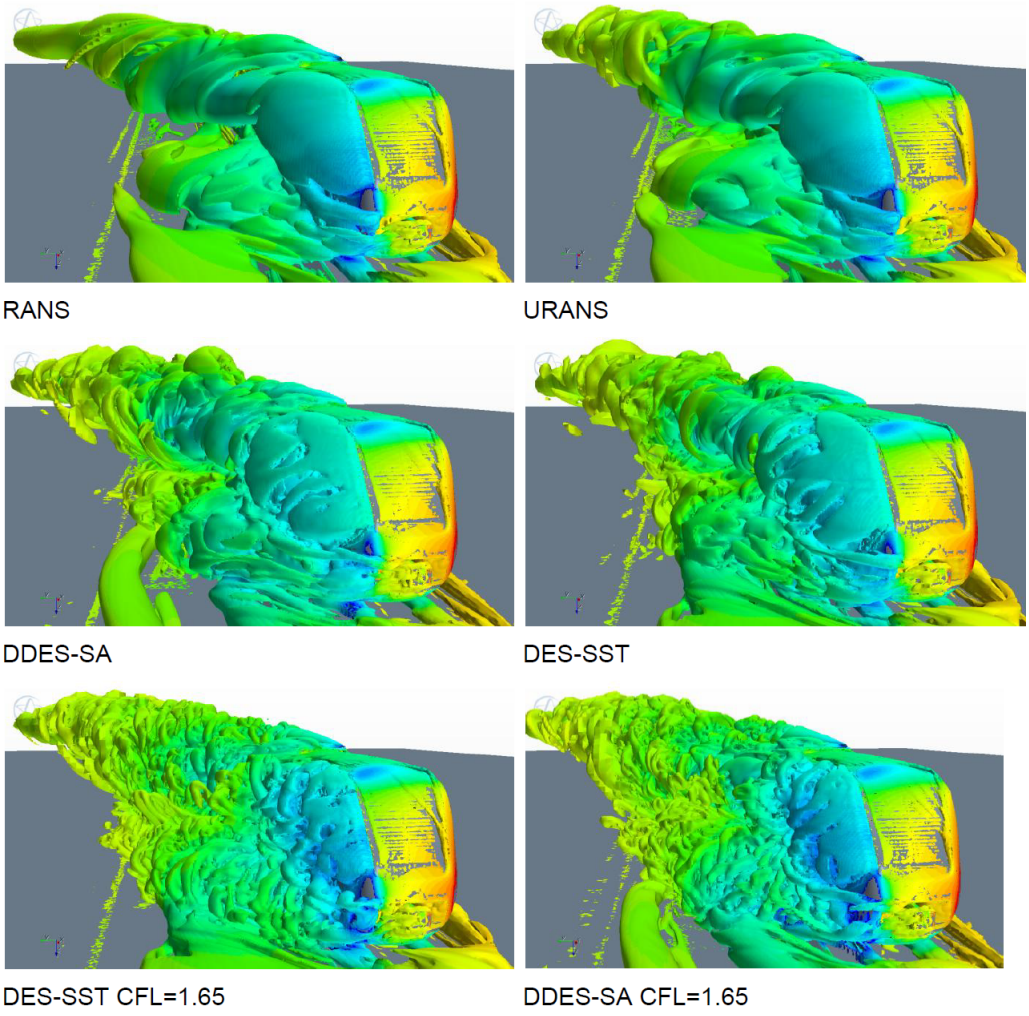

Figure 2.12. $\lambda 2$ iso-surfaces for different simulation models reproduced from [8]

In the AeroTRAIN project [8], a study was performed to analyse the influence of the model and the precision of the results. In table 2.1 these differences between a certain case and experimental data are quantified. It can be seen that, for instance, RANS equations lack a lot more in accuracy in comparison to DES. However, DES simulations require much more computational effort compared to RANS, so the decision to relay on one technique or the other is a commitment between accuracy and computational cost. The chief challenge of CFD relays then on the appropriateness of the CFD approach chosen which combines an adequate computational mesh, computational method and turbulence modelling.

Therefore, due to the differences that may be encountered between the models, CEN norms updated with AeroTRAIN project results, impose certain requirements to ensure a minimum accuracy and veracity of the results. These restrictions are [12]:

- To demonstrate the appropriateness of the CFD approach, calculations shall be made for at least one specified benchmark vehicle, in a similar fashion to that described for validating wind tunnel measurements.

Case	Yaw angle	$\Delta Cmx, lee_{EN}$	ΔCmx_{EN}	ΔCy_{EN}	ΔCz_{EN}
RANS	30	-7.7%	-3.9%	-3.6%	-15.7%
URANS	30	-7.6%	-2.9%	-2.5%	-17.6%
DES	30	-2.5%	3.7%	7.4%	-15.5%

Table 2.1. Averaged simulation results coefficients for ICE3 relative to EN14067-6 taken from [8]

- Geometrical representation of the vehicle should be done according to those restrictions imposed for wind tunnel testing (see section 2.3.
- Dimensions could be full or model scale. Domain should not interfere with the flow in any unpropitious way. And so, the domain should be extended at least 8 characteristic heights upstream and 16 downstream, where the characteristic height is defined as the distance from the top of the train to the ground (including ballast and rail). No requirements are defined for lateral or vertical distances.
- Computational method shall be able to model the viscous, turbulent, unsteady, three-dimensional and strongly separated flows. Nevertheless, steady methods may be used as well for cases were steadiness of the flow is evident.
- Calculations should involve a sensitivity test regarding mesh and turbulence modelling.
- Regarding boundary conditions, train surfaces must be treated as no-slip walls and ground may be either stationary or moving with a relative velocity. Top and lateral planes should be define to model the appropriate yaw angle configuration.
- Reynolds number requirement is the same as for wind tunnel testing.

As seen in the guideline established by CEN norms, simulations can be performed in a STILL or Moving Reference Frame (MRF). This means, that in the same manner that was exposed in the experimental case, the simulations can be performed taking into account the relative motion of the flow between infrastructure and vehicle. In fact, the most appropriate (but also more complex) way to approach the real problem would be using a MRF as in reality, the infrastructure sees the actual wind velocity where as the vehicle sees the composition between its own velocity and that of the wind.

However, regarding wind tunnel testing, [32, 33] concluded that the differences encountered between static and moving tests laid within the confidence band of experimental errors and so, static experiments were enough. In fact, still models are preferred for experimental testing because of its greater robustness and reliability. Nevertheless, it is the case for negligible infrastructures like small embankments but not for big ones where the effect of relative movement is not negligible at all.

Therefore, as at experimental levels the set-ups are much more complex, other studies like [2] analysed the effect with CFD technology in order to have a better

understanding on the matter. In this case, relative movement was considered in the boundary condition and RANS equations and $k-\omega$ SST model were used to solve the problem.

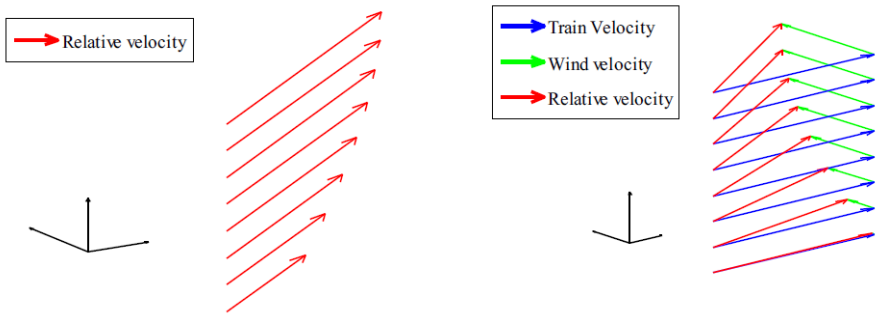

Figure 2.13. Comparison of incoming boundary conditions on a still train (left) and on a moving train (right) reproduced from [2]

They concluded that when a relative motion is considered in a STBR scenario, computed coefficients are larger for MRF. Namely less than 5% for lateral forces and moments and a bit higher for lift coefficients, which seems to be more sensible at variations in the apparent velocity. Underestimation of the coefficients in the Still case is translated also into underestimation of the CWCs. However, this underestimation in the CWCs was below 1.5%, which in turn is even less than the errors that a MRF in a wind tunnel test would imply. Lastly, in the case of a DTBR, errors were much higher, and ground structure played an important role in the relative velocity affecting considerably forces and moments coefficients. Hence, in the case of STBR, still model is preferred while a MRF approach would fit better a DTBR configuration.

Lastly, it is worth understanding a bit better the vortical structures that appear according to CFD data found in the literature. In section 2.1, a first behaviour was presented, however, different studies show certain discrepancy among the scientific community about the structure that generates at low angles of yaw.

In figure 2.4, a double structure of vortices generating from the nose and other two further downstream was shown. Nonetheless, in figure 2.14 a different behaviour was studied by [9], suggesting that the flow is composed by 3 vortices. The first one, starting at the bottom leeward edge of the nose and dissipating very quickly. A second one starting behind the first vortex downstream. And a third one starting at the upper leeward edge at the front of the leading car, and growing downstream.

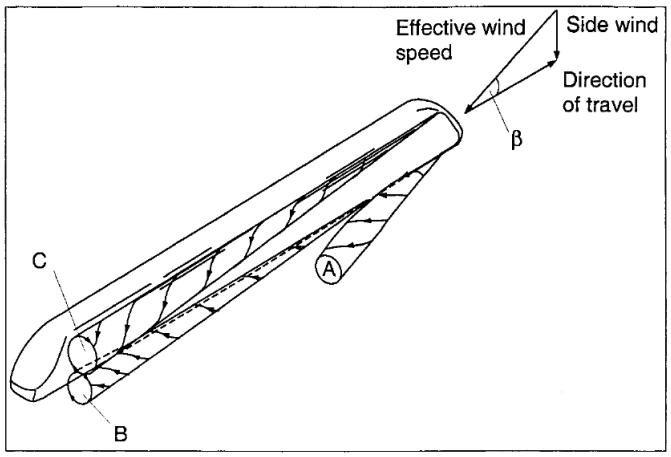

Figure 2.14. Schematic view of the flow structure for small yaw angles reproduced from [9]

However, also in results obtained from AeroTRAIN project where many different types of trains were tested, flow structure differed as well depending on the vehicle that was understudy. Figures 2.15, 2.16 and 2.17 are results obtained from the analysis they performed. They plot coloured velocity magnitude profiles against in plane velocity vectors.

Looking at these pictures, vortex cores may be indicated by points at which where velocity vectors rotate about either clockwise or anticlockwise. These are highlighted by white circles to ease its identification. Note that, the main problem from these figures and all the images usually found in the literature is that they do not show iso-vorticity lines, and hence, vortex cores must be estimated by the behaviour of the in plane tangential velocity, which is not ideal because vortex intensity is completely ignored.

Nevertheless, it can be seen that vortex location (and probably size as well), depend on the vehicle tested. The criteria and references used by AeroTRAIN consider distance $x = 0$ the middle of the leading car, thus increasing x when moving towards the nose of the vehicle. Therefore, although previous studies already mentioned stated a two vortical structure moving downstream along the whole train, these CFD results (which were computed also for different modelling methodologies) show in the 3 cases that two vortices may generate at the beginning of the leading car but, moving downstream, they come together to build what appears to be just one main core.

Lastly, it is worth highlighting as well that in results presented in [8], it can be deduced also that the CFD modelling used for the analysis may influence the velocity field magnitude, but that it does not affect the vorticity field at least in terms of in-plane tangential velocity vectors behaviour.

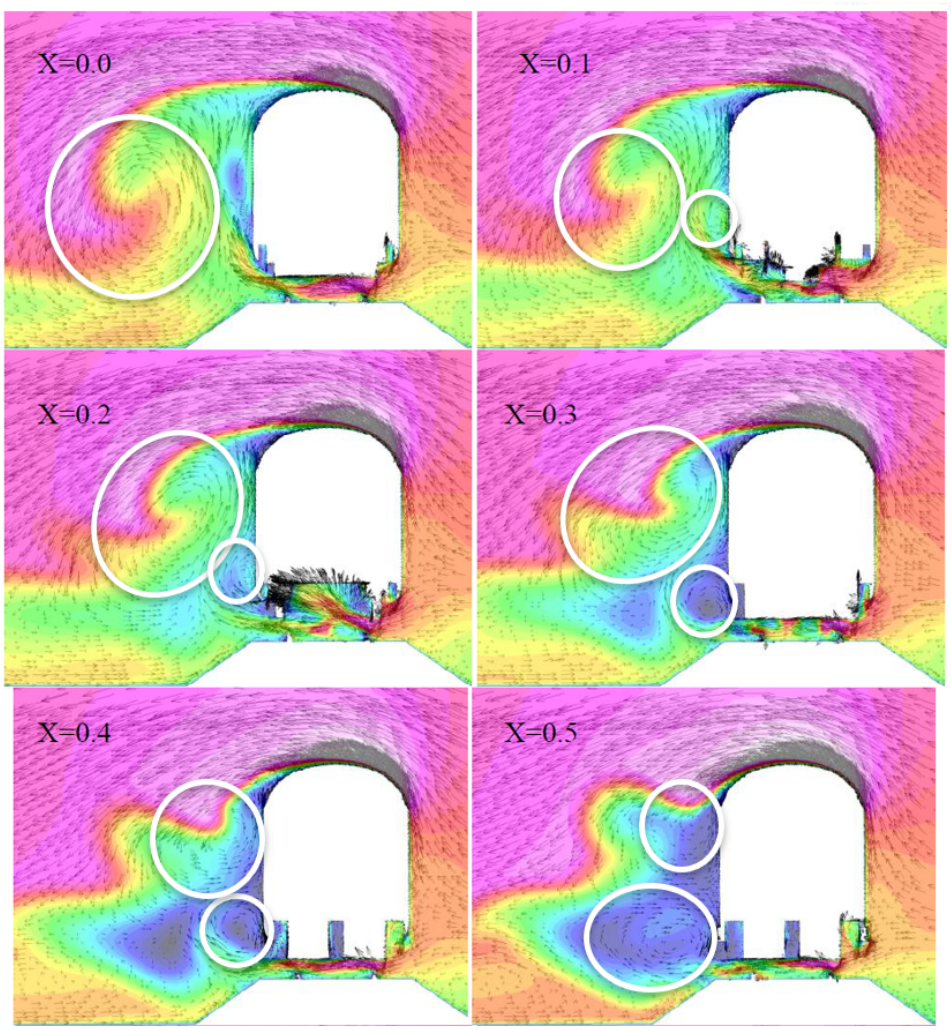

Figure 2.15. Velocity magnitude with in plane velocity vectors for RevCo train at a yaw angle of 30 degrees. Reproduced from [8]

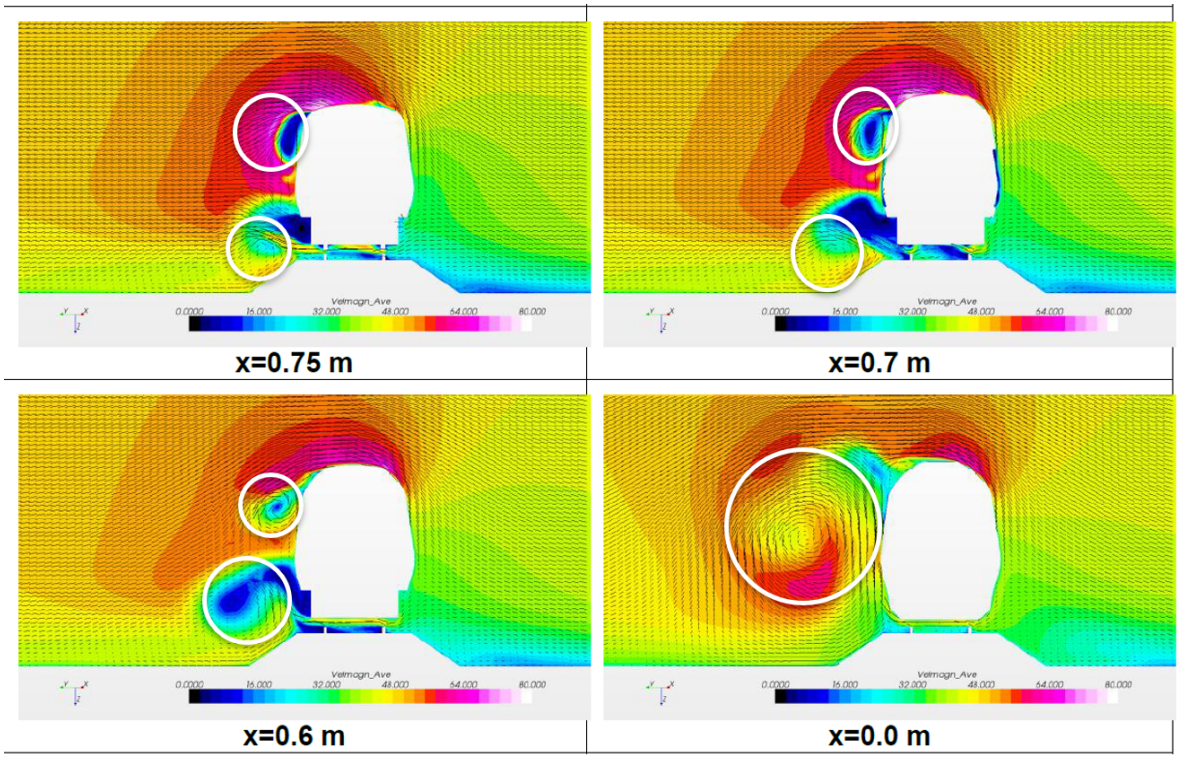

Figure 2.16. Velocity magnitude with in plane velocity vectors for IC4 train at a yaw angle of 30 degrees. Reproduced from [8]

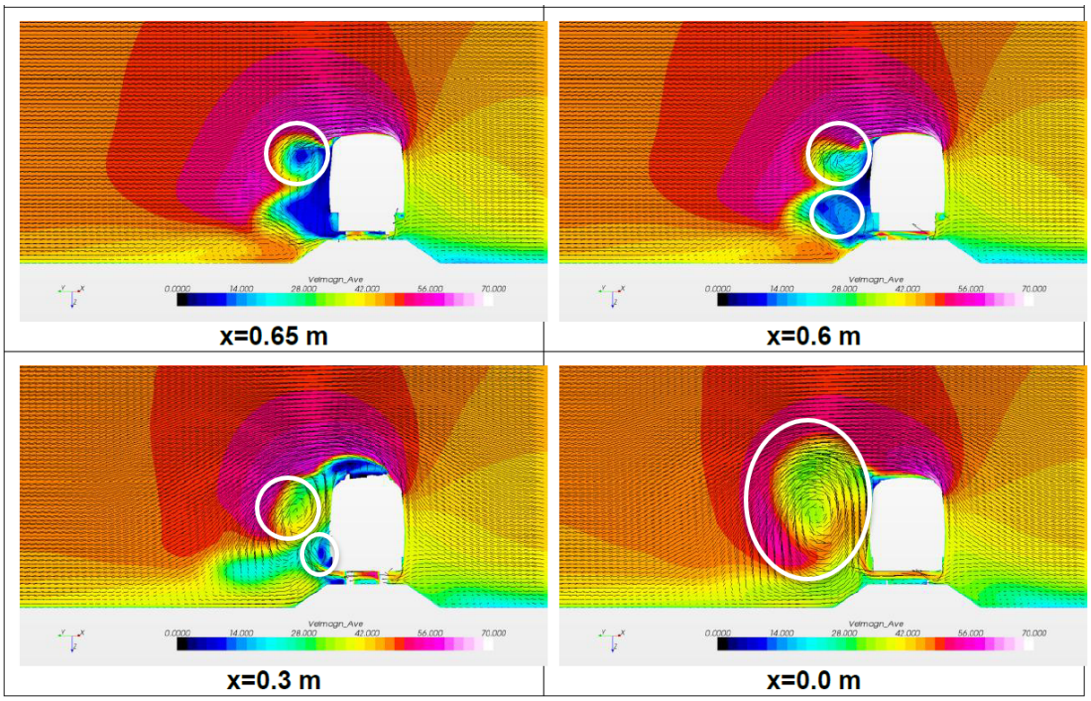

Figure 2.17. Velocity magnitude with in plane velocity vectors for VT612 train at a yaw angle of 30 degrees. Reproduced from [8]

2.5 Conclusions

In this chapter the crosswind phenomenon has been presented. In particular, is a problem concerning lateral stability of trains and is a characteristic that is certainly very important if over turning of the leading car wants to be avoided for safety. Cross Wind Curves (CWC) define the limits of the railway vehicle in terms of wind velocity and trains velocity.

To determine these curves, different methodologies may be used. From analytical equations that might give a first insight on the problem, to experimental techniques like real scale testing or wind tunnel testing, and lately, also Computational Fluid Dynamic tools (CFD).

The last two are the preferred ones so Virtual Homologation can be achieved, encouraging less costs for rail companies. However, it has been shown that is not an easy task because many variables may affect the studies. To enhance validity of the tests and comprehension of the phenomenon, wind tunnel tests are used together with CFD tools, allowing for feedback between each other.

For STBR, still models can be used either for wind tunnel testing or CFD. Also, for the sake of simplicity and less computational costs, RANS modelling can be used if some steadiness of the flow is present (i.e. small yaw angles).

Lastly, disagreement among the scientific community regarding the vortical structure present in the flow field has been proved. In fact, it is not clear how many vortex may be created during crosswind conditions. Not even the mechanism that determine size or location of the vortex. In fact, also results presented do not help to enhance understanding of the phenomenon as figures still lack some important information like vorticity field. Thus, the challenge becomes not only trying to apply CEN rules for conventional trains, but also understanding the aerodynamic mechanisms that rule the behaviour of the flow in crosswind conditions.

Chapter 3

CFD simulations

In this chapter the methodology pursued will be exposed. The geometry analysed is described together with the domain used for the simulation and the computational methodology applied. A short insight into the mathematical background that support the physical behaviour of the flow is given in appendix A. Finally, a mesh sensitivity analysis is discussed to validate the model developed for all the analysis described in chapter 4.

3.1 Geometry description

3.1.1 Description

The geometry under study in the CFD model can be decomposed in some generic parts as shown in figure 3.1. The ground configuration for the whole set of analysis is a "single track with ballast and rail" set-up. Then, the train model consists in the leading car, the bogies and a second or trailing car. Regarding the latter, the ETR500 model presents only the second car, while conventional trains present also a trailing car apart from the second (see figure 3.3). Recall that only the power car is of interest as it is the most critical part of the train under crosswind conditions, so the following cars are only of interest to ensure proper aerodynamic behaviour of the flow.

It is worth mentioning also that the vertical distance from the bottom part of the train to the rail, and from the beginning of the ballast to the nose of the leading car are set to match same conditions encountered in the wind tunnel.

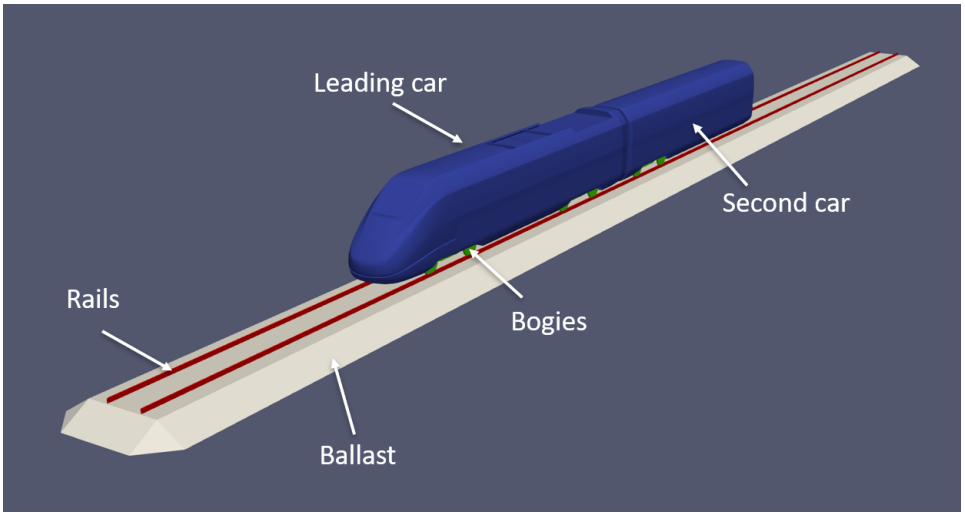

Figure 3.1. Geometry composition

Figure 3.2. Trains under study

In figure 3.2, the whole set of real trains that is going to be studied is presented. Then, in figure 3.3, the actual CAD models used for the CFD analysis are shown.

The reason to choose these trains is endorsed by the following facts:

- *ETR500* is a high-speed train already analysed during the AeroTRAIN project [19], so the CFD results will allow a proper validation of the model developed.
- *Intercity* is a conventional single-decker train which presents the bottom of the train partially faired, hence, not much irregularities affect the underfloor aerodynamics. However, is not to low so that air cannot flow more freely compared to the ETR500.

- *Regionale* is also a conventional single-decker train but it does not have the underfloor faired. It has also the nose less flat in comparison with the Intercity.
- *Vivalto* is a conventional double-decker train which has the underfloor faired and closer to the ballast and rail, so it is more similar to the ETR500 as the gap for the airflow to pass by is much smaller than in Intercity or Regionale trains.

As here exposed, this set of trains allow a good comparison between the different geometric characteristics that may have some direct effect on the aerodynamics. Thus, permitting a better understanding of the airflow behaviour under crosswind conditions for assisting future conventional train designs.

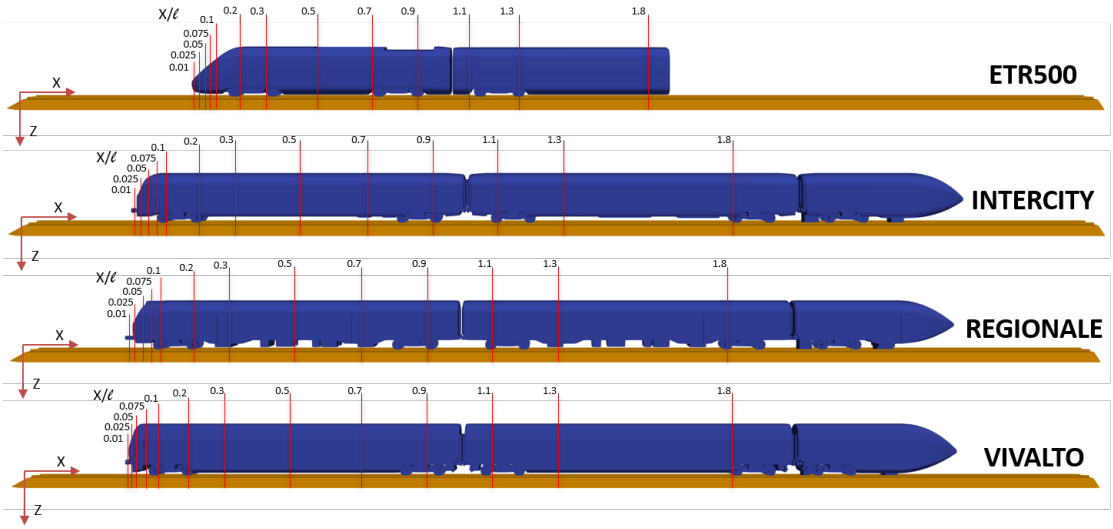

Figure 3.3. Train models for CFD study

3.1.2 Dimensions

It is important to state the geometrical dimensions of each train, in particular the leading vehicle, as later on they will be needed for the analysis. Nevertheless, all simulations are performed with geometries at scale 1:20.

Train	Tot. Height	Long.	Bot. Height	Lat. Area
ETR500	3.96 m	20.6 m	0.056 m	$\approx 71\ m^2$
Intercity (IC)	3.98 m	26.4 m	0.52 m	$\approx 91\ m^2$
Regionale (REG)	3.96 m	26.6 m	0.78 m	$\approx 93\ m^2$
Vivalto (VIV)	4.25 m	27.1 m	0.2 m	$\approx 110\ m^2$

Table 3.1. Vehicles measures

In table 3.1, measures are considered for the first car, being the total height the distance from the roof to the rail, the longitude the distance between the very front to the end of the car, and the bottom height the distance between the rail and the underfloor fairing.

3.2 Simulation domain

3.2.1 Description

In order to decide the computational fluid domain characteristics as size restrictions, position of the model or meshing parameters, among others, guidance from AeroTRAIN project [8] will be followed.

It is stated that there should not be any interference with the flow around the vehicle and, to ensure that, EN norms [12] establishes that the domain should start at least 8 characteristic heights (c) upstream from the leading edge of the ballast and 16 characteristic lengths downstream from the trailing edge. This characteristic height is defined as the distance between the top of the vehicle and the ground, including the ballast. As a schematic picture, in figure 3.4 a longitudinal section of the domain summarizes these restrictions.

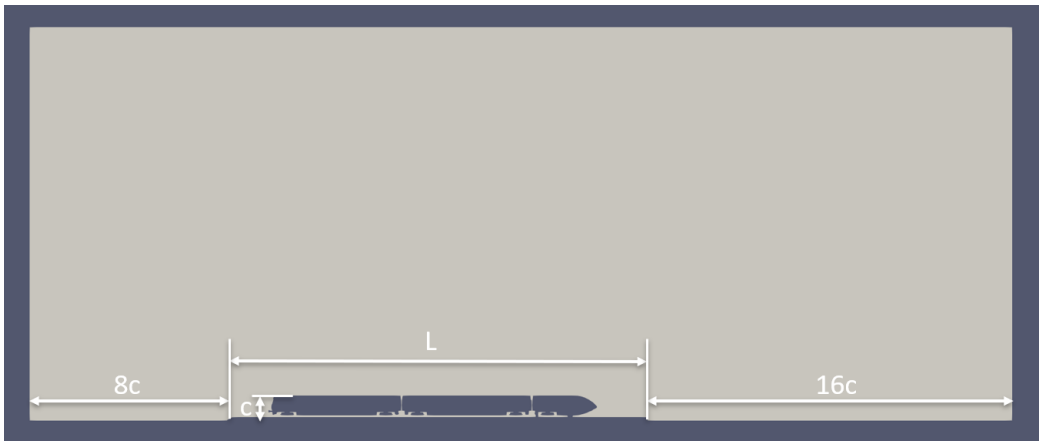

Figure 3.4. Minimum distances for the models according to [12]

3.2.2 Coordinate system

Furthermore, it is important to establish a common reference system to be able to compare the moment and force coefficients. Therefore, the coordinate system used coincides with [13] (see figure 3.5), where reference geometrical scaling parameters are assumed to be $d_0 = 3m$ and $A = 10m^2$ ([12]).

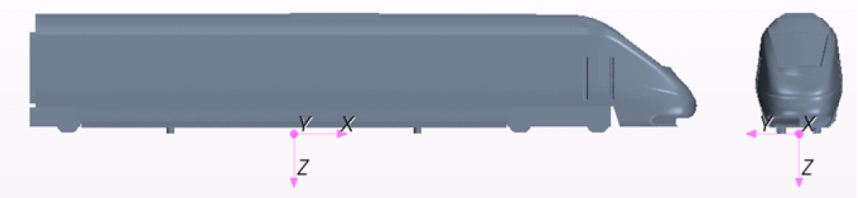

Figure 3.5. Coordinate system taken from [13]

3.2.3 Mesh set-up

With regard to the mesh, it should be able to resolve the pressure and velocity gradients, boundary layer, detachments, recirculations, etc. To assess this problem properly, a sensitivity analysis must be performed to check mesh independence at 30 degree of yaw angle [8], where mesh resolution is changed among them.

Five refinement zones can be distinguished within the mesh and differentiated by box like shapes with different refinement levels. This has been achieved with the use of *blockMesh* and *snappyHexMesh* utilities from ©OpenFOAM.

In figure 3.6, a transversal section shows the decomposition of these subdomains and the transition and difference in detail and mesh size between them. The top and bottom zones are the ones more critical as together with the surface refinement define the level of detail on how well is going to be captured the phenomenon related to the boundary layer.

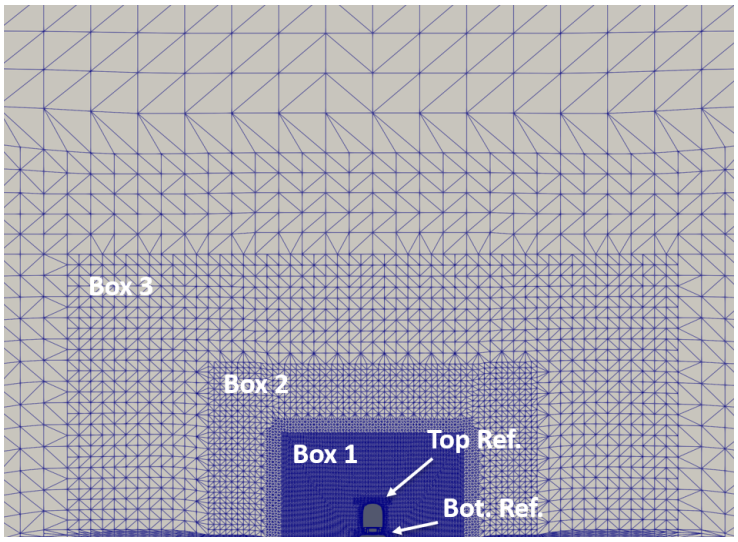

Figure 3.6. Mesh refinements subdivisions.

The numerical mesh has been developed with a combination of polyhedral and trimmed hexahedral control volumes, being the latter the type of cell more present within the domain. In [12], it was proved that hexahedral type mesh was more sensible at higher yaw angles, leading in fact, to higher discrepancies when compared to experimental data, thus it will be considered in chapter 4.

Lastly, but not least, it is well established among the CFD community that in order to capture properly the boundary layer, y^+ should be around 1 if it is solved directly or between values of 30 to 150 if wall functions are used. However, [8] showed that in this particular case, y^+ value did not have a significant influence in the accuracy of the results when recommended turbulence models are used. In fact, what they found was that it is advisable to aim for a dimensionless distance that lays somewhere in the buffer zone regarding the law of the wall, i.e. $y^+ \approx 5 \sim 30$.

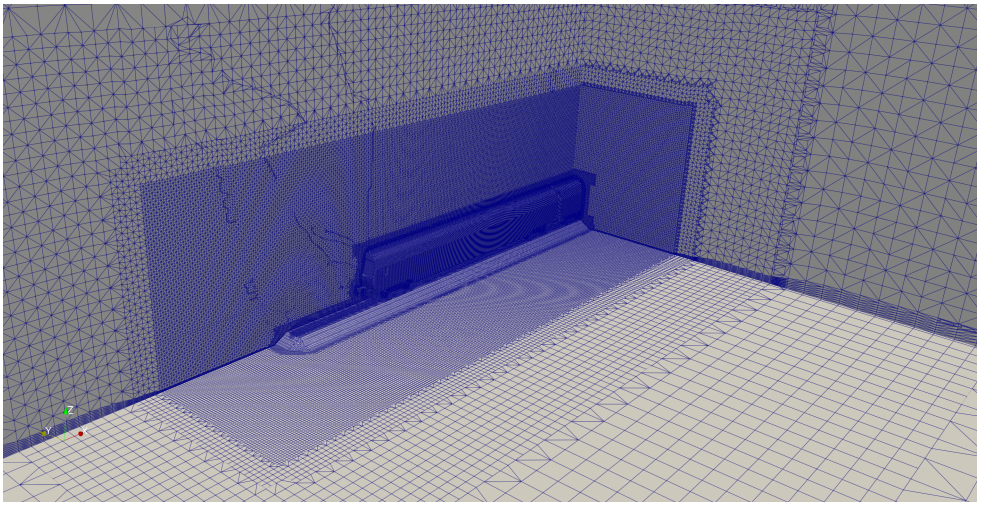

Figure 3.7. Mesh refinements subdivisions.

3.3 Computational method set-up

3.3.1 Turbulence modelling

The physics of a train under crosswind conditions is a problem where the airflow structures change with wind incidence angle as seen in chapter 2. Flow's inherently instability increases for big yaw angles, until the maximum angle of 90 degrees where is completely unstable and Von Kármán vortical structures form.

Nevertheless, it is extremely rare to find such high angles as it is formed by the composition of relative velocity between the moving vehicle and the incident airflow. Thus, as instability is not that high at angles of interest below 30 degrees, RANS model is used to save in computational cost and time.

Furthermore, as seen in appendix A, $k-\omega$ SST model is recommended by [12], and it presents also big advantages in comparison to other turbulence models when approaching problems like the one concerning, where high speeds are present but also detachment of the boundary layer.

Therefore, because of what has been previously discussed and the reasons here stated, the simulations will be performed with RANS equations, together with a $k-\omega$ SST turbulence model, FVM discretization, upwind interpolation for kinetic energy and omega parameters and linear-upwind for velocity, and solved with SIMPLE algorithm.

3.3.2 Boundary conditions

The following boundary conditions have been considered for the simulations, which agree as well with [8] criteria:

- Two velocity inlets where velocity components are defined in order to achieve

the desired yaw angle.

- Two pressure outlet downstream where static pressure is specified.
- Two walls with no slip boundary conditions, representing the ground and roof of the wind tunnel.
- No slip boundary conditions applied to the whole geometry under studied without any moving reference frame for the reasons discussed in chapter 2.

In figures 3.8 and 3.9 these conditions are presented in a more illustrative manner.

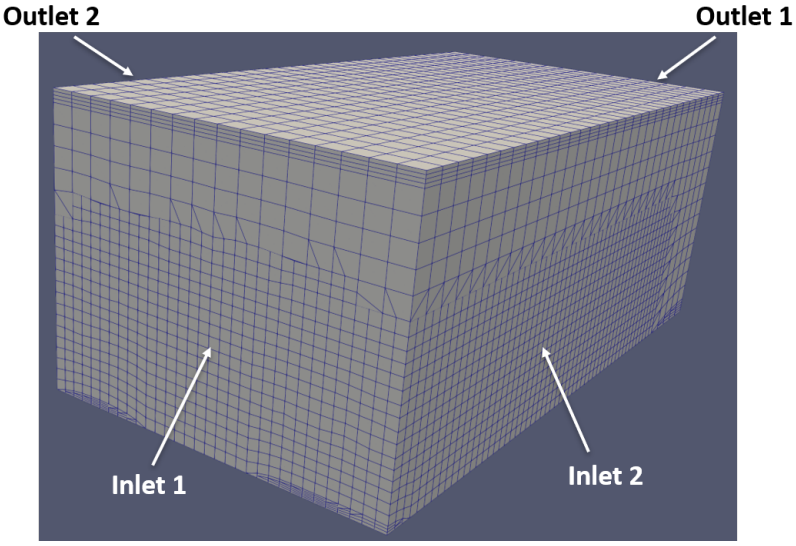

Figure 3.8. Outside view of the computational fluid domain already meshed.

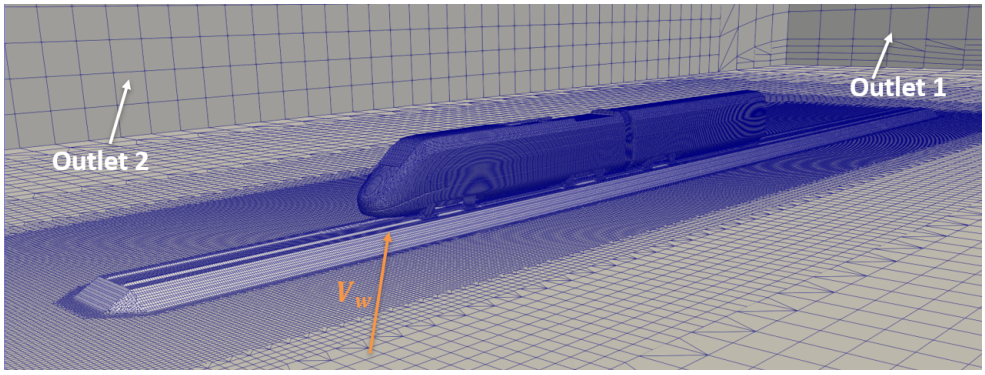

Figure 3.9. Inside view of the computational fluid domain already meshed

Also, the parameters values for velocity, air density and dynamic viscosity are:

- $U_\infty = 15 \quad m/s$
- $\rho = 1.225 \quad kg/m^3$

- $\mu = 1.8375x10^{-5} \quad kg/ms$

The value of velocity is computed by taking into account the scale 1:20 of the model and fulfilling the minimum Reynolds number requested by [12], which is $Re > 2.5e5$.

3.4 Validation

3.4.1 Sensitivity analysis

As requested by [12], a sensitivity analysis of the mesh is performed at 30 degrees of yaw angle to achieve a proper domain for the CFD analysis. 5 grids with different sizes haven been developed by changing basically the refinements of the subdomains and surface of the geometry.

In figure 3.10 the results are summarized. It can be seen how convergence of the results is achieved from grids with 5 million elements onwards. Thus, although a mesh of fine quality would be valid for the analysis, extrafine parameters will be used for conventional trains. The reason for assuming this increase in computational cost lays on the fact that geometries of conventional trains have much more irregularities compared to the ETR500, so better detail of the grid will be probably needed.

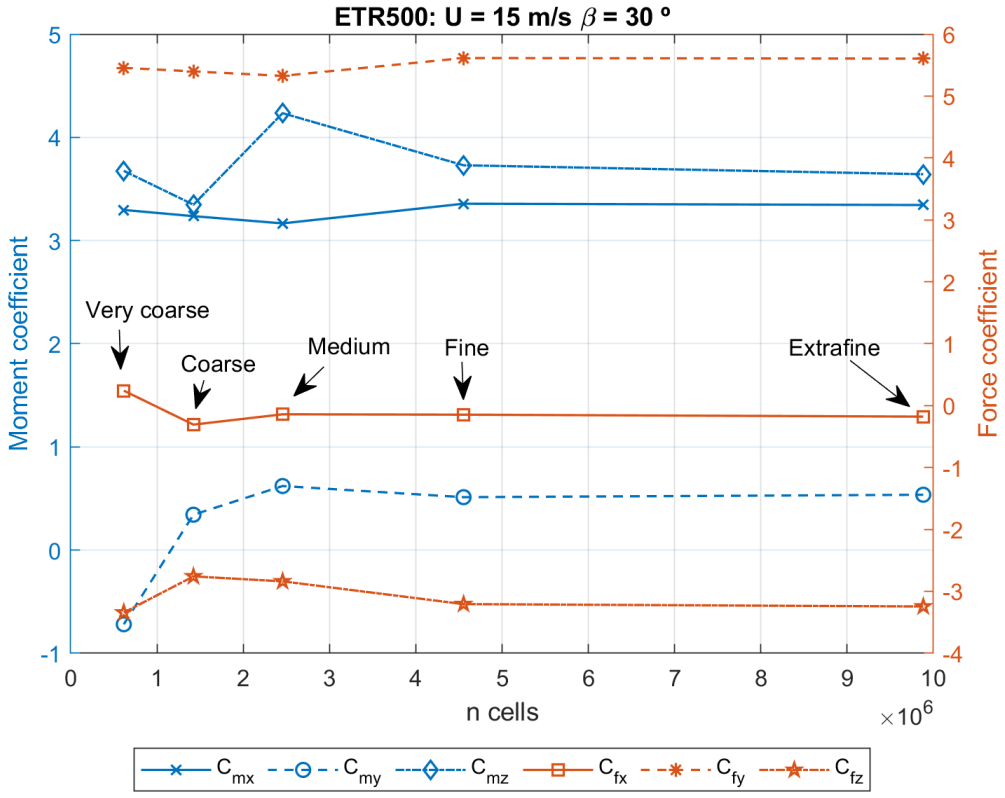

Figure 3.10. Sensitivity analysis results. Moment and forces coefficients values.

3.4.2 Experimental wind tunnel data comparison

Once the mesh has been decided, the simulation is carried out for yaw angles of 0, 10, 20, 30, 45, 60 and 90 degrees. Then the main coefficients are analysed and compared with EN14067-6 results [12]. These comparisons are conducted in pictures 3.11, 3.12, 3.13 and 3.14.

According to EN14067-6 norms, a limit in error is established for $C_{mx,lee}$ where $\varepsilon < 0.15$ [12] i.e. 15% relative error between CFD and experimental data is the maximum value permitted. Analysing the results from the graphics, the model is considered valid as the relative error for $C_{mx,lee}$ never exceeds the 15% threshold. Nevertheless, some differences can be seen and should be considered and analysed in further detail in chapter 4.

Notice that results are nearly the same but as the yaw angle is increased, so does the difference between them. In fact, CFD data underestimates the coefficient, probably due to the increase in instability and the fact that steady RANS equations do not handle well this type of flow.

Recall also the equation to compute the non dimensional moment coefficient around the leeward rail which is $C_{mx,lee} = C_{mx} - C_{fz} \cdot b_0/l$; where $2b_0 = 1.5 \quad m$ for a standard gauge track of 1435 mm and $l = 3 \quad m$. Then, looking at figure 3.14, it can be seen that the model struggles more to capture properly the lift coefficient in comparison with experimental data, which makes $C_{mx,lee}$ to have bigger errors than C_{mx}.

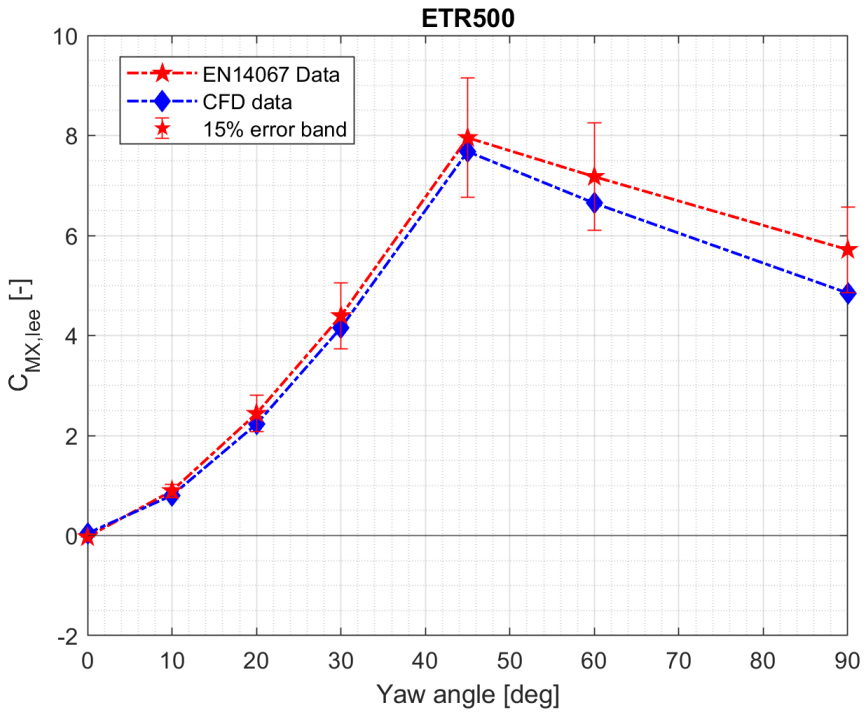

Figure 3.11. ETR500 $C_{mx,lee}$ comparison between CFD and experimental data.

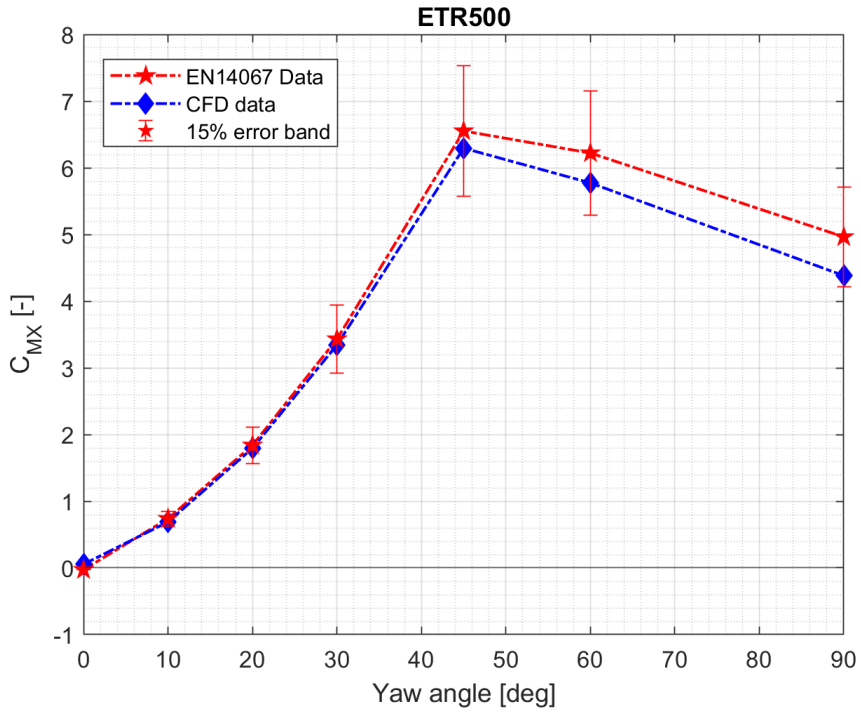

Figure 3.12. ETR500 C_{mx} comparison between CFD and experimental data.

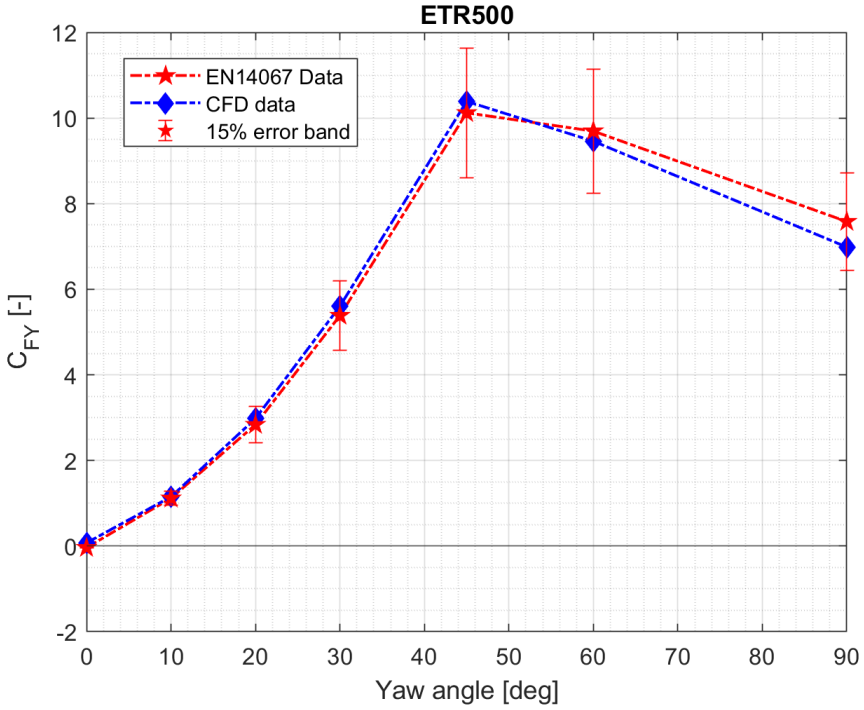

Figure 3.13. ETR500 C_{fy} comparison between CFD and experimental data.

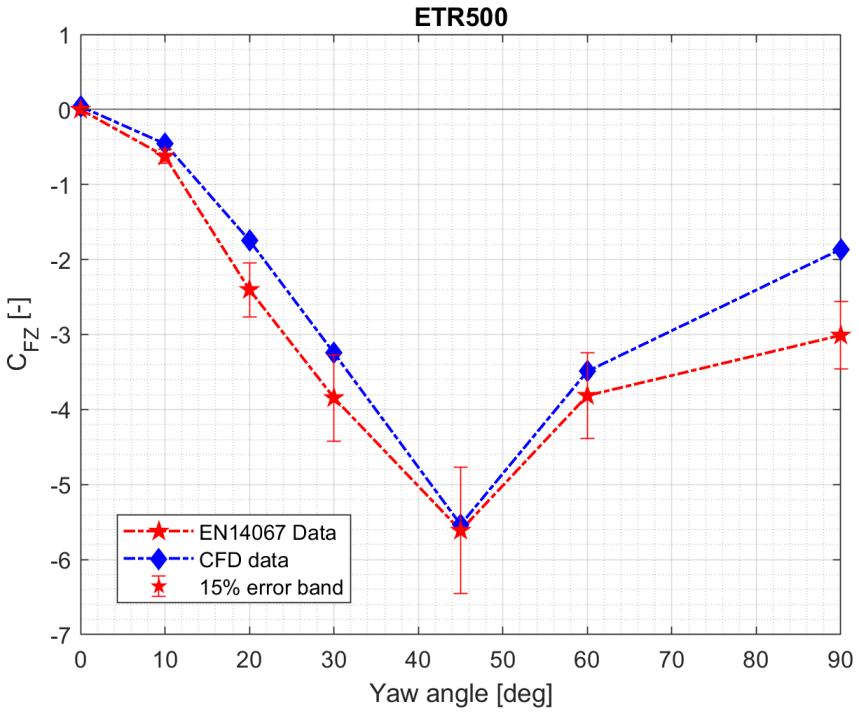

Figure 3.14. ETR500 C_{fz} comparison between CFD and experimental data.

ETR500 STD	0	10	20	30	45	60	90
C_{Fx}	0.02	0.014	0.015	0.082	0.06	0.14	0.24
C_{Fy}	0.03	0.014	0.028	0.052	0.14	0.26	0.48
C_{Fz}	0.02	0.03	0.035	0.093	0.09	0.25	0.49
C_{Mx}	0.002	0.001	0.003	0.005	0.016	0.028	0.04
C_{My}	0.01	0.007	0.01	0.02	0.027	0.09	0.08
C_{Mz}	0.01	0.004	0.004	0.02	0.05	0.11	0.15

Table 3.2. Relative standard deviation in % of the different coefficients after 2500 iterations.

In table 3.2, the relative standard deviation in % of the different coefficients for every simulation performed on the ETR500 are shown. The results are obtained for 2500 iterations. CEN standards require that a relative standard deviation has to be below 0.25% in order to ensure convergence of the results. Thus, it can be seen that for high yaw angles (60 and 90), the high values achieved in the STDs prove a struggle for obtaining a stationary solution and hence, pointing to the inherently physical unsteadiness condition of the problem.

3.4.3 Analysis of the influence of wind tunnel balance measurement equipment

As some differences are present, the doubt of whether experimental measurement equipment may affect or disturb the flow in some way arised. Thus, a CFD analysis

taking into account the equipment used in wind tunnel testing at POLIMI was conducted in order to discard possible causes of errors.

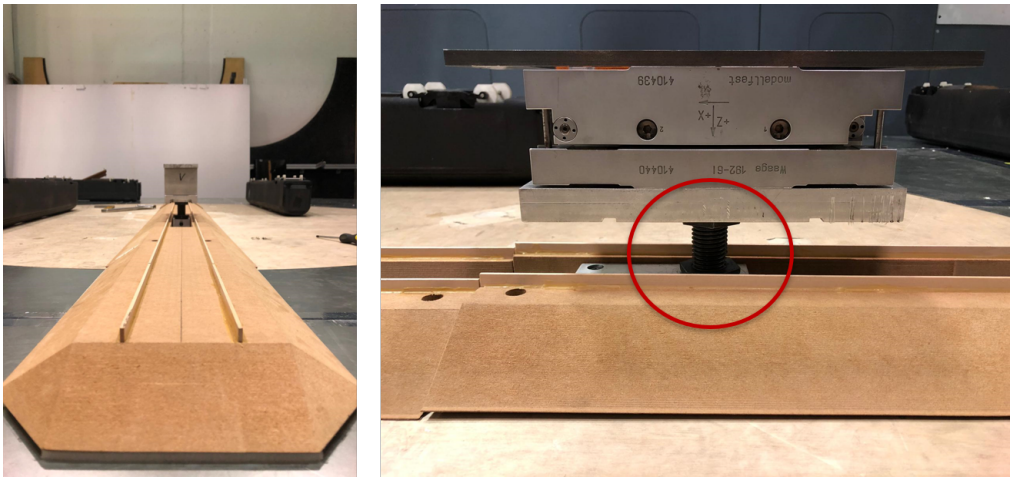

Figure 3.15. Wind tunnel setup of ballast and balance.

In figure 3.15, the experimental set-up in the wind tunnel shows the balance that is put inside the train to measure the forces and moments applied by the wind on the vehicle. The doubt rises from the presence of the balance bolt which in practice is a cylindrical disturbance between the underfloor and the ballast. This could be, for instance, the reason for the discrepancies regard lift coefficient.

Therefore, this geometry has been considered in the CFD model as shown in figure 3.16, and analyses, presenting then the results in graphs 3.17, 3.18, 3.19 and 3.20.

However, as it can bee seen in the graphs, the relative error is close to zero, so the presence of the balance does not affect significantly the flow and thus, will no be present during the analysis of conventional trains in chapter 4

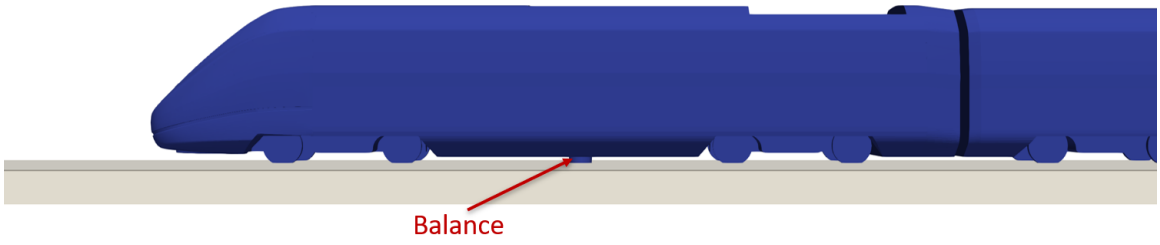

Figure 3.16. CFD setup of ballast and balance.

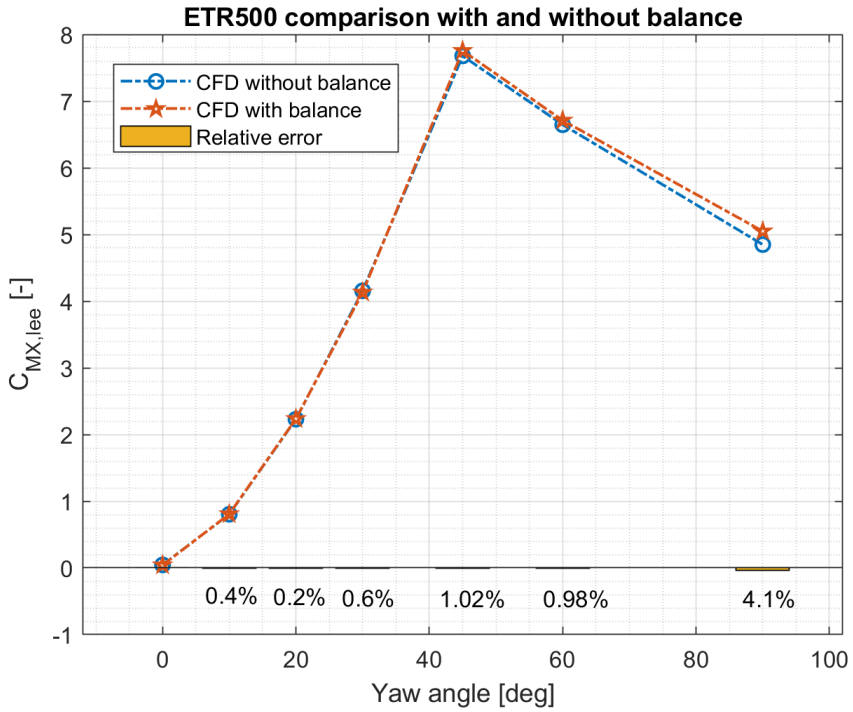

Figure 3.17. Balance influence results in ETR500 $C_{mx,lee}$ values.

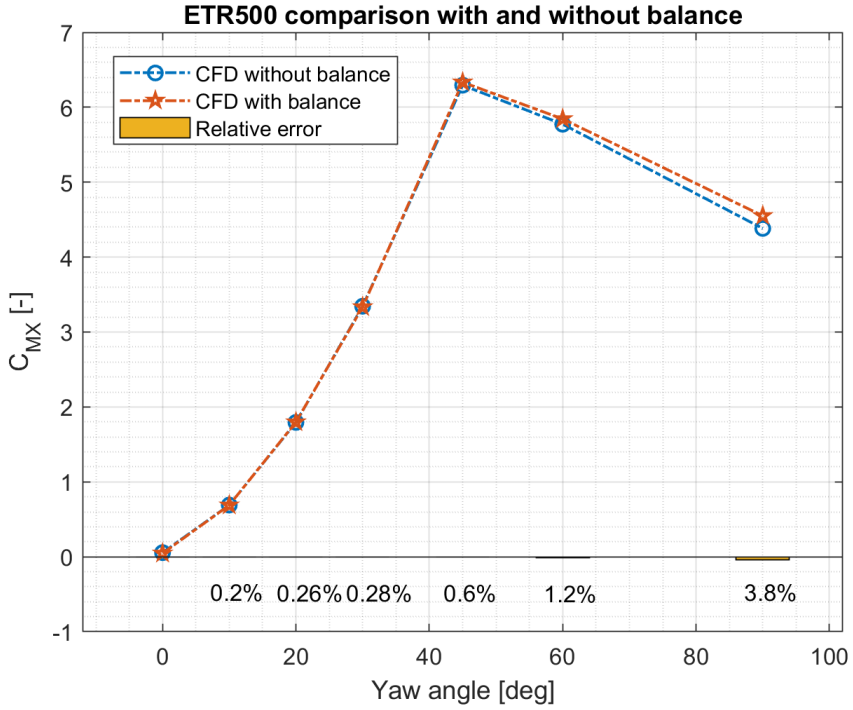

Figure 3.18. Balance influence results in ETR500 C_{mx} values.

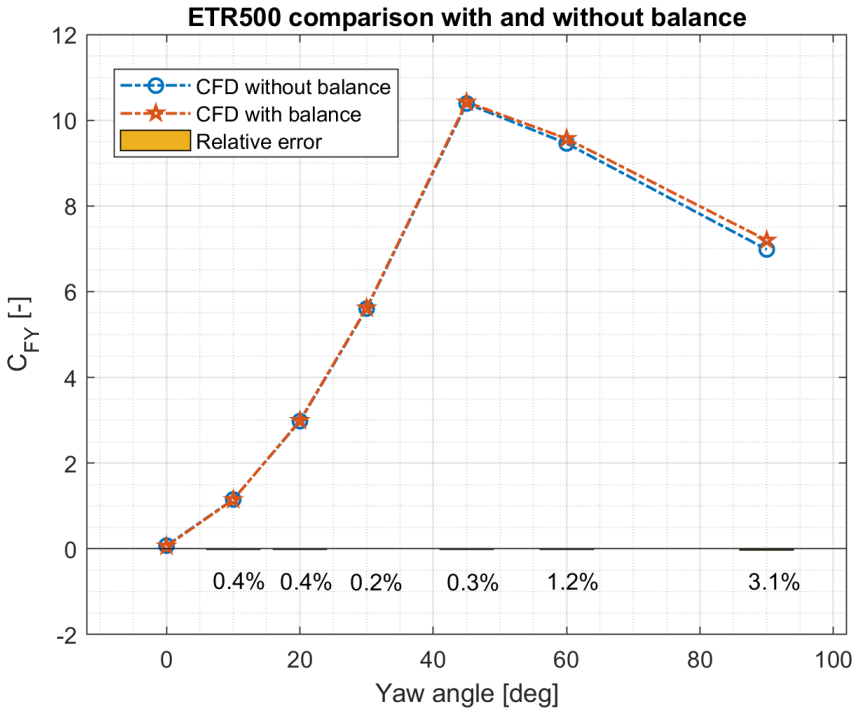

Figure 3.19. Balance influence results in ETR500 C_{fy} values.

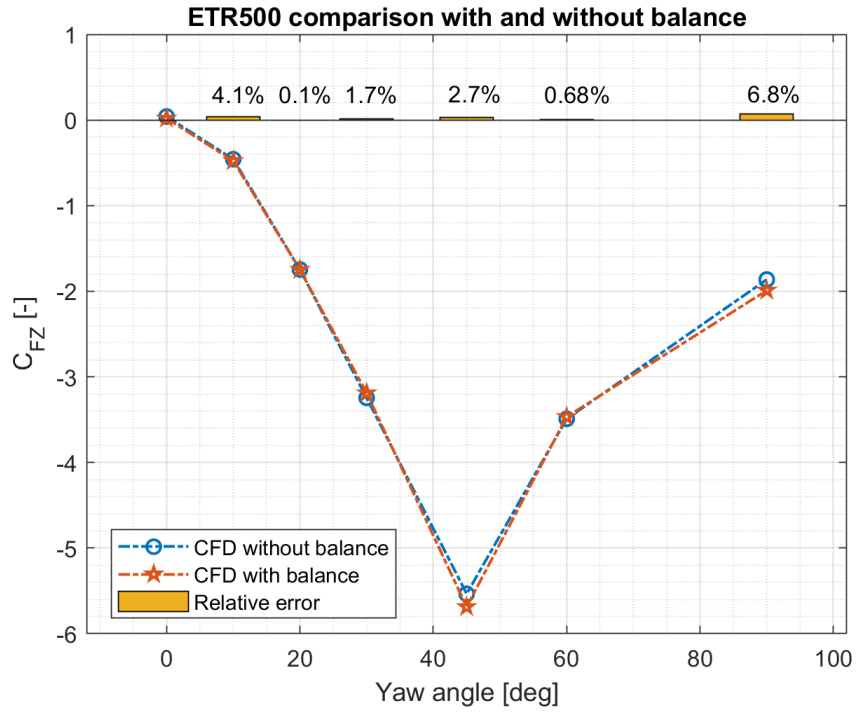

Figure 3.20. Balance influence results in ETR500 C_{fz} values.

Chapter 4

Results analysis

In this chapter, the results obtained from the CFD simulations performed for each train are presented and discussed. Specifically, force coefficients and moment coefficients are compared and some differences are established among the different vehicles. Then, a qualitative analysis is carried out to understand the physical differences between the various types of trains.

The mesh and model approach developed in chapter 3 has been used for every simulation. In fact, the finer meshing procedure has been considered (mesh sizes around 11 million elements) as the flow becomes more turbulent and unsteady for conventional trains and thus, more precision in the grid is needed for accuracy and convergence as expected.

4.1 Introduction

In this section, results obtained are presented in a quantitative way. In figures 4.1 and 4.2 the results for the different force and moment coefficients are presented for a range of yaw angles between 0 and 90 degrees. In addition, CFD results are compared simultaneously with experimental data already post processed and obtained at POLIMI's wind tunnel.

To start with, by looking at figure 4.1 two different behaviours can be distinguished among these 4 types of leading car vehicles. Vivalto and ETR500 have a very similar behaviour along the whole range of yaw angles (group 1), while Intercity and Regionale form a different set (group 2). In particular, the main difference is observed for high wind incidence angles where the first group sees a decline in the coefficients while the second group reaches a stable value at 60 degrees remaining constant until a fully perpendicular yaw angle.

In terms of CFD results, the behaviour matches almost experimental data, especially for group 1. Nevertheless, comparing quantitatively the values obtained, the second group presents an underestimation of the coefficients, being the regional train the one showing less accuracy. It is worth noticing also that this difference is worsen as yaw angle increases, reaching a maximum error at 45 degrees. However, the criteria to

validate the results established by [12] of achieving an error below 15% for $C_{MX,lee}$ is fulfilled for angles below 45 degrees (see Appendix B). However, for greater angles is not norm compliance, showing that RANS approach may not be sufficient for high Yaw angles in conventional trains. Thus, the challenge that arises becomes explaining why VIVALTO train, being also a conventional railway vehicle, does not present this inaccuracy and presents a different behaviour compared to group 2.

Lets highlight then three main areas along the curves, namely for $C_{MX,lee}$, C_{MX} and C_{FY}, which can be distinguished by the three oval regions presented in picture 4.1. Note as well that C_{FZ} is much more inaccurate quantitatively and qualitatively for the whole spectrum of yaw angles. It shall be expected as it was also an issue observed while doing the validation analysis in chapter 3 and, as showed before, it was also a problem encountered during the AeroTRAIN project [19]. Hence, the dare is trying to understand why it is the only coefficient not captured properly and also, why there is such a difference within the different vehicles as shown in the experimental data.

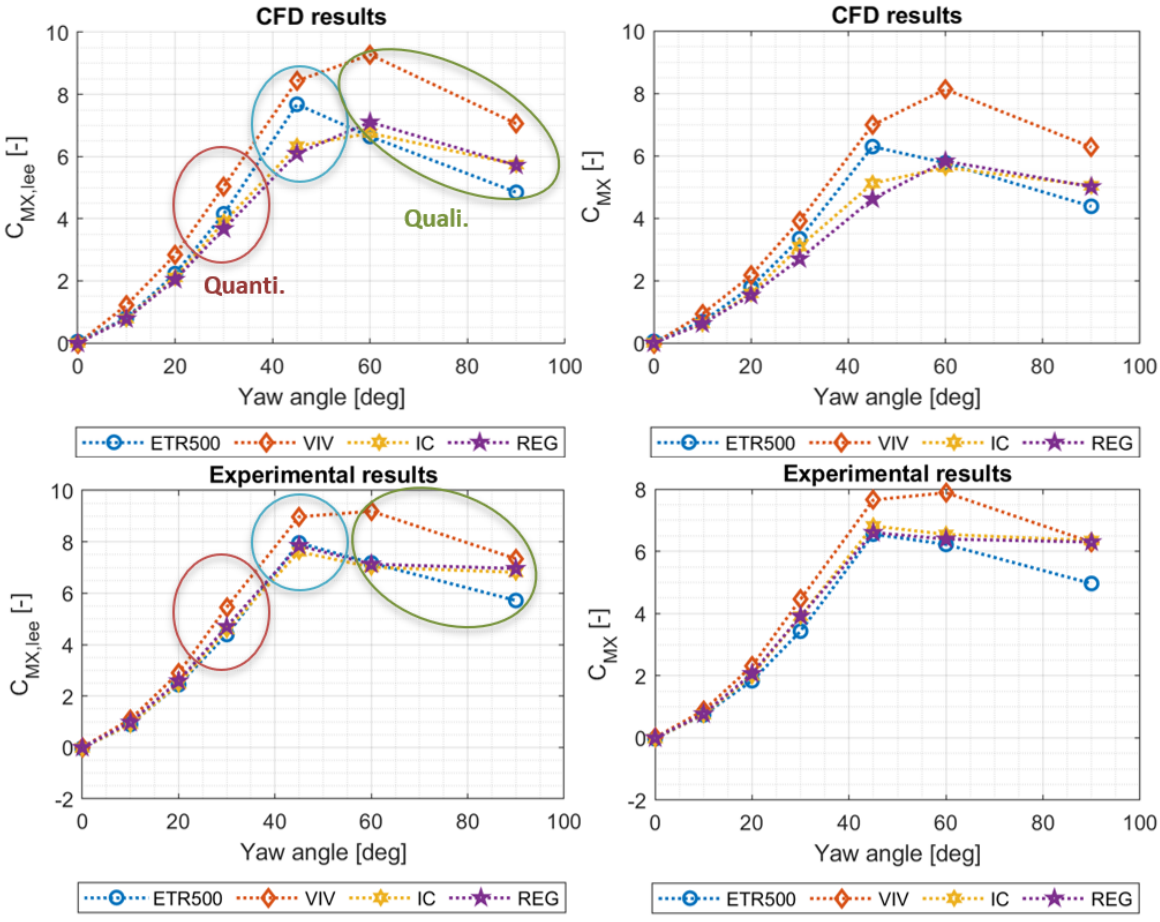

Figure 4.1. $C_{MX,lee}$ and C_{MX} coefficients comparison between CFD data and experimental results for every train under study.

And so, in order to have a first insight that allows a better understanding of the phenomenon, a first visualization of the flow around the vehicles becomes very useful. In figures 4.3 and 4.4 streamlines are shown for every train at 30 degrees of yaw angle

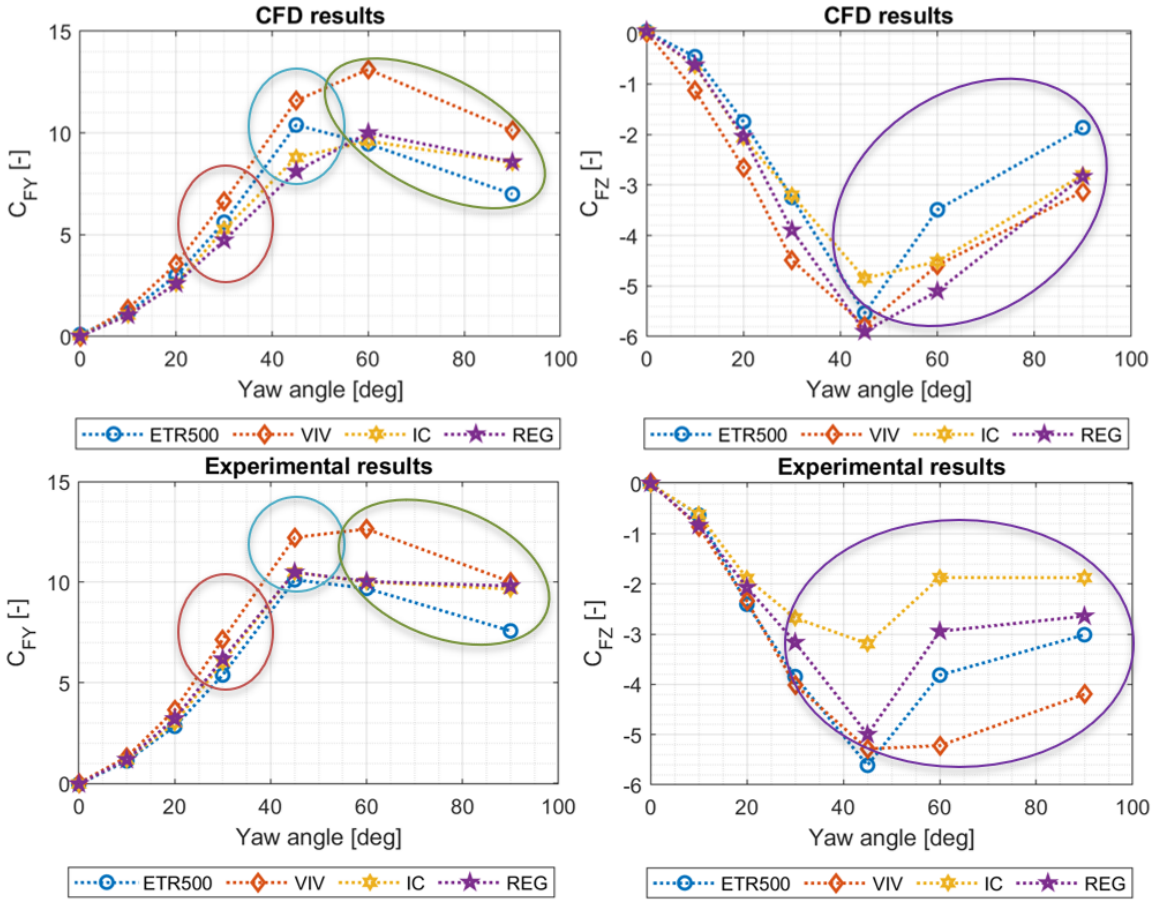

Figure 4.2. C_{FY} and C_{FZ} coefficients comparison between CFD data and experimental results for every train under study.

and for every yaw angle for Vivalto train respectively. The reason to particularize for this vehicle lays on the fact that is the train which has captured with less error the aerodynamic coefficients when compared to experimental data (see appendix B). Thus, it is the criteria that will be followed throughout the whole analysis when presenting qualitative results from Vivalto.

Taking a closer look into figure 4.3, two vortical structures are present. The flow reaching the nose of the train creates two vortices. The Main Vortex (MV) that is generated on the leeward side of the vehicle and continues increasing in size downstream, and a Secondary Vortex (SV), which is also created at the nose of the vehicle due to the presence of a recirculation bubble generated by the detachment of the flow. In fact, looking closer, it is appreciated that it becomes bigger and stronger for flat nose trains (ETR500 SV cannot be nearly appreciated), and for bigger trains in terms of hight, like Vivalto.

Note also that streamlines and trains' surfaces are coloured according to pressure coefficient highlighting the core of the vortices by the low pressure generated and giving a first hint on the reason for Vivalto's coefficients to be higher.

Moreover, by looking at figure 4.4 a first relation between the behaviour presented in the coefficient graphs is appreciated, which relates the increase in the coefficients'

value with the increase in vortex strength. This fact is demonstrated by the reduction of pressure with an increment in the yaw angle, achieving a maximum depression at 45 degrees (maximum $C_{MX,lee}$). Also, for cross-flow cases the vortical structure becomes more complex as it presents a mixed Von Kármán structure. The principal one is produced by the basic shape of a cylinder in a free stream which creates two vortical structures with circulation in the y-z plane, while the second one is created at the ends of the vehicle and it generates as well a Von Kármán street vortex sheding within the x-y plane. In figure 4.5 the lateral vortices (LV) can be seen formed in a clearer way by means of the stream lines.

Hence, the flow becomes not only highly unsteady in one plane but rather in two, leading to convergence and accuracy problems for a RANS approach. This conclusion could be the main reason for inaccuracy problems seen for high angles when comparing CFD vs experimental data. Thus, it will be analysed further during this chapter to get a better understanding on the phenomenon and why it is higher for the Intercity and Regionale trains with respecto to the first group.

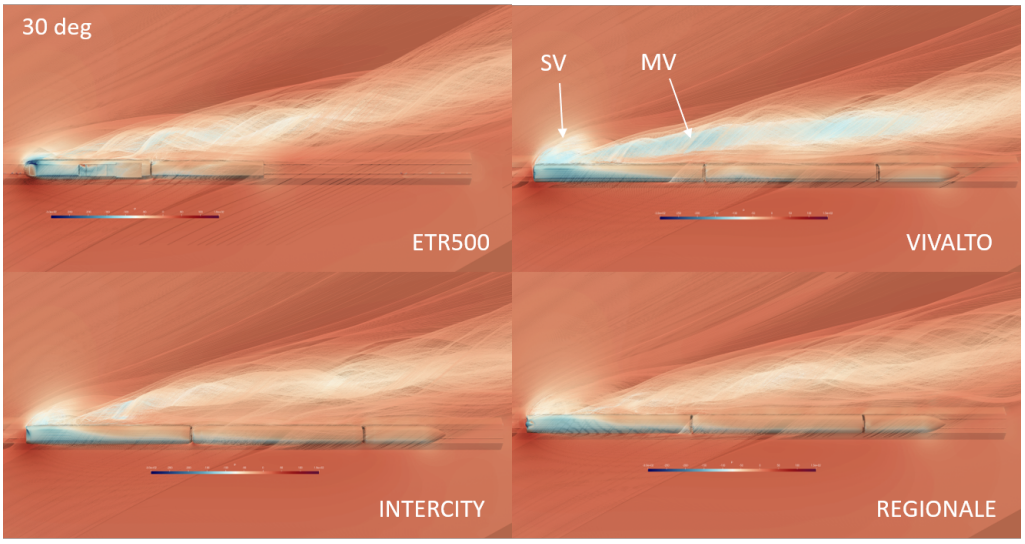

Figure 4.3. Vortical structure visualization based on streamlines for every train at an angle of 30 degrees.

Lastly, after having analysed the main results and having stated the main differences for the principal coefficients, it is straight forward that results should be approached in two different ways depending on the yaw angle. In particular, they can be divided in angles that range from 0 degrees to 45 and from 45 to 90, where 30 degrees is the best angle for comparison in a quantitative and qualitative way due to is grater precision and its more frequent occurrence in real conditions. Then, 90 degrees yaw angle is studied to have a better understanding in a qualitative way of the flow behaviour around the different leading cars so that some hypothesis can be stated to explain the main differences among these two groups at high wind incidence angles.

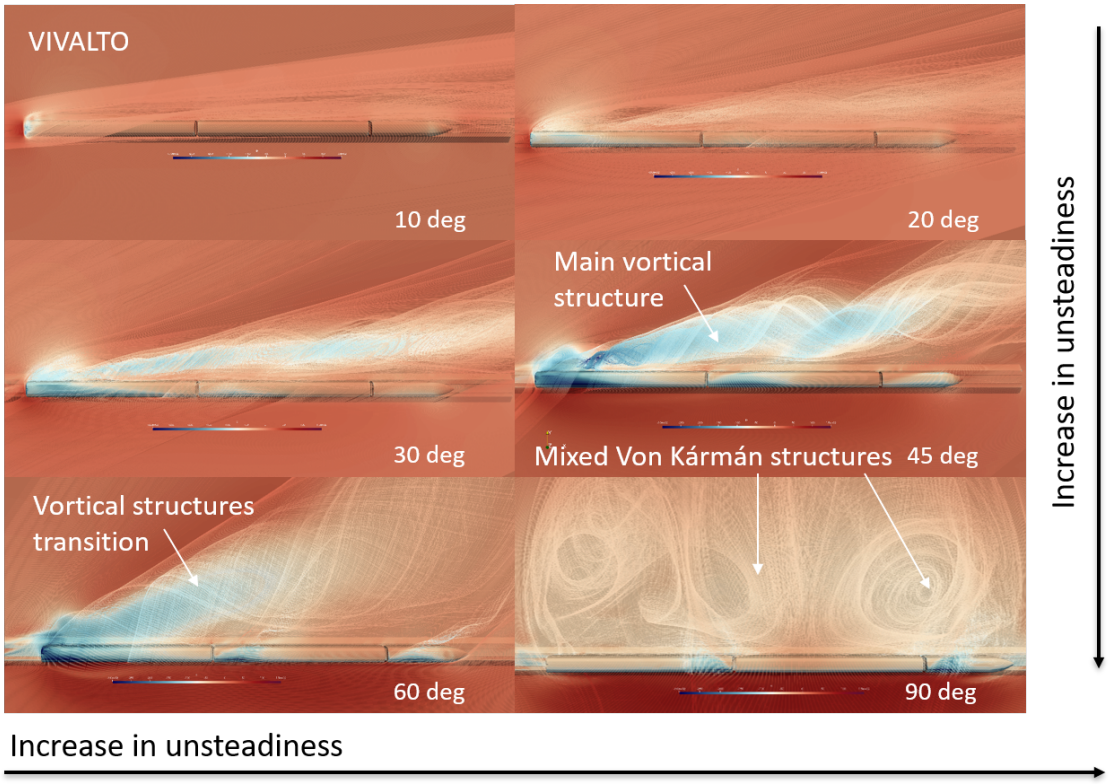

Figure 4.4. Vortical structures evolution visualization based on streamlines around Vivalto train at different yaw angles.

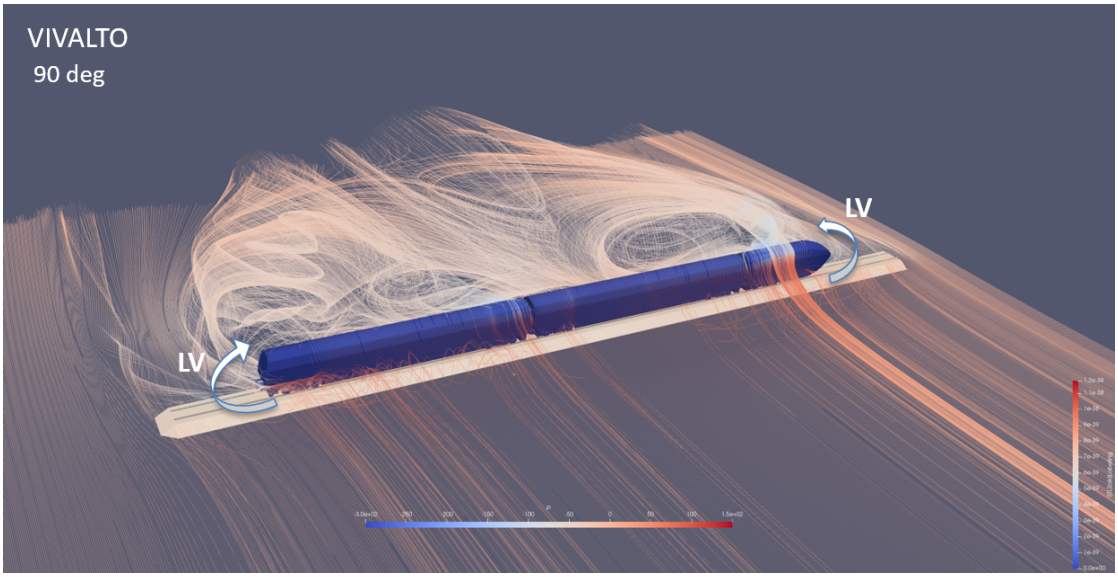

Figure 4.5. Vortical structure created at 90 degrees of yaw angle.

4.2 Results for small yaw angles

The objective of this section is to comprehend the cause of the aerodynamic coefficients behaviour involving crosswind phenomenon and state the main differences between the two main groups of vehicles already discussed at a quantitative and qualitative level.

In particular, the way to tackle the problem is going to be based in the concept of circulation and its relation to the creation of lift (in this case, lateral force mainly) proposed by Kutta-Joukowsky [50] (see equation 4.1). This different insight with respect to the literature, may allow a better understanding of the crosswind phenomenon. As a matter of fact, this perspective is an alternative way to explain phenomena surrounding any aerodynamic shapes like is done, for instance, with Delta Wings [51].

$$L' = \rho_\infty V_\infty \Gamma \tag{4.1}$$

Where ρ_∞ is the density of the free stream, V_∞ is the velocity of the free stream and Γ the circulation of the vortex responsible for the forces. This circulation at a given x/l location is obtained by integrating the velocity over the closed contour C as shown in equation 4.2.

$$\Gamma = \oint_C \mathbf{u} \cdot \mathbf{dl} \tag{4.2}$$

This in turn, can be related with the amount of vorticity by means of Stoke's theorem where the amount of circulation is equal to the flux of vorticity (ζ) through a certain surface S.

$$\Gamma = \int_S \zeta \cdot \mathbf{n} \quad dS \tag{4.3}$$

$$\zeta = \nabla \times \mathbf{u} \tag{4.4}$$

Therefore, as show in this mathematical procedure, vorticity can be related to the forces exerted on the body. The challenge lays on quantifying the circulation [50](potential theory, vortex pannel method, CFD, etc). From here onwards, the normalized circulation $\Gamma/U_\infty c$ will be used to be able to compare results between different trains.

Figure 4.6 shows iso-surfaces of vorticity magnitude equal to 1000 coloured proportional to the pressure coefficient value C_p for different yaw angles particularized for Vivalto train.

It can be deduced from the figure that the amount of vorticity rises with an increase in the yaw angle as the sizes of the iso-surfaces become bigger on the leeward side of the vehicle. This produces a stronger suction of the underneath flow which in turn translates into a higher depression of the flow showed by the colouring of the pressure coefficient C_p. At the leeward side the main vortex dominates the flow and the secondary vortices form two clear lobes of vorticity at the upper and lower leeward side of the leading car which dissipate very quickly.

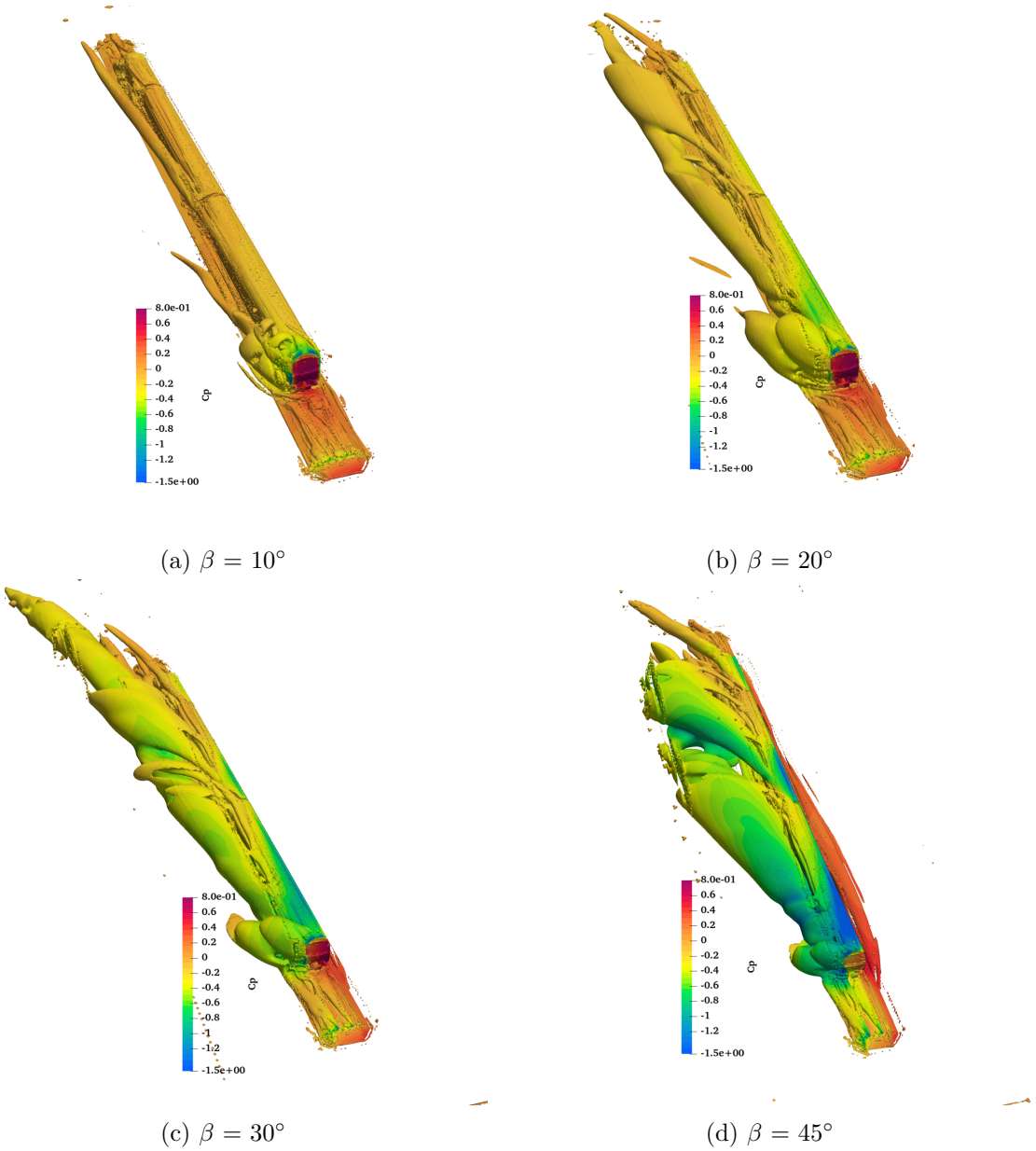

(a) $\beta = 10°$ (b) $\beta = 20°$

(c) $\beta = 30°$ (d) $\beta = 45°$

Figure 4.6. Iso-surfaces of vorticity magnitude equal to 1000 coloured in proportion to the pressure coefficient C_p at angles of yaw $\beta = 10°$,20°,30° and 45° for Vivalto train.

This behaviour confirms indeed the hypothesis that lateral force coefficient C_{FY}, and hence also C_{MX} and $C_{MX,lee}$, grow with the increment in the wind incident angle until reaching the maximum value at 45 degrees. Then, the vortex breakdown starts and a transition to the secondary vortex shedding structure occurs.

Then, understanding the effect of geometrical features on the vortical structures is pursued. A good approach is achieved by means of analysing the x-component of the vorticity in the y-z plane along the whole length of the leading car, as it is able to show the main component of vorticity, its breakdown location, core location and strength.

Figures 4.7, 4.8, 4.9 and 4.10 represent vectors of averaged tangential velocity in the y-z plane and contours of normalized x-component of vorticity at various lengthwise sections at $\beta = 30°$ for every train. Notice that at locations where exists a transition between refinement areas in the mesh, vorticity is computed and hence elements at this locations are also coloured. However, it seams not to create significant discontinuities in the iso-contours of vorticity so results are valid for a qualitative analysis.

To start with, the first train is the ETR500 which belongs to the first group discussed in section 4.1. Its main characteristic in comparison to conventional trains lays in its streamlined shape which reduces the drag resistance i.e C_{FX} (see Appendix C in normal operating conditions. The absence of abrupt changes in geometry avoids the detachment of the flow at the very front of the leading car and therefore, the secondary vortex founded at other vehicles is not present. Also, the primary vortex is very small in size if compared to other cars and it forms at the top leeward side of the train.

The breakdown is produced by a counter vortex that generates at the front bogie and wraps up along the leeward face of the train, creating the main core of the MV. As the size and strength of the vortex is not that high compared to other trains, and the breakdown occurs very early (at $x/l = 0.5$), the force and moment coefficients should not be very significant either. However, quantitative data in CFD and wind tunnel testing tells the opposite.

Taking a closer look at figures (c) and (d) an important geometrical detail is playing its roll. In fact, as the roof of the leading vehicle is not rounded and some sharp edges exist, a new vortex is created at the very end of the leading car which in turn breaks down by the counter vorticity of the second bogie, leading to a new core formation which ends up joining the one already created. This engenders a main vortex composed by two cores, enhancing its strength and thus, its forces and moment coefficients.

On the other hand, Vivalto is a conventional train with a very different front end shape with respect to the ETR500. A completely flat nose creates a very strong vortex that starts at the upper edge. At the same time and in the same way it happened with the ETR500, a counter vortex starts at the front bogie and rolls up around the leeward side accounting for the breakdown of the main vortex at $x/l = 0.9$.

In this case the core is formed only by one vortical structure because the top part of the train is continuously rounded. It shows in fact darker colours meaning a higher amount of vorticity, which indeed explains the higher moment and forces coefficients. This is probably related to the size of the leading car in terms of hight, as the frontal area is not much different from other vehicles.

Also lateral lobes can be seen forming at a distance $x/l = 0.1$ in the upper and lower part of the leading car. Consequently, the only geometrical similarity that exists among these two leading cars is the distance from the underfloor of the car to the top of the rail. They belong to the group of trains which are closer to the rails, limiting the amount of flow that can pass by, thus strengthening the main vortex as a significant counter vortex is not formed.

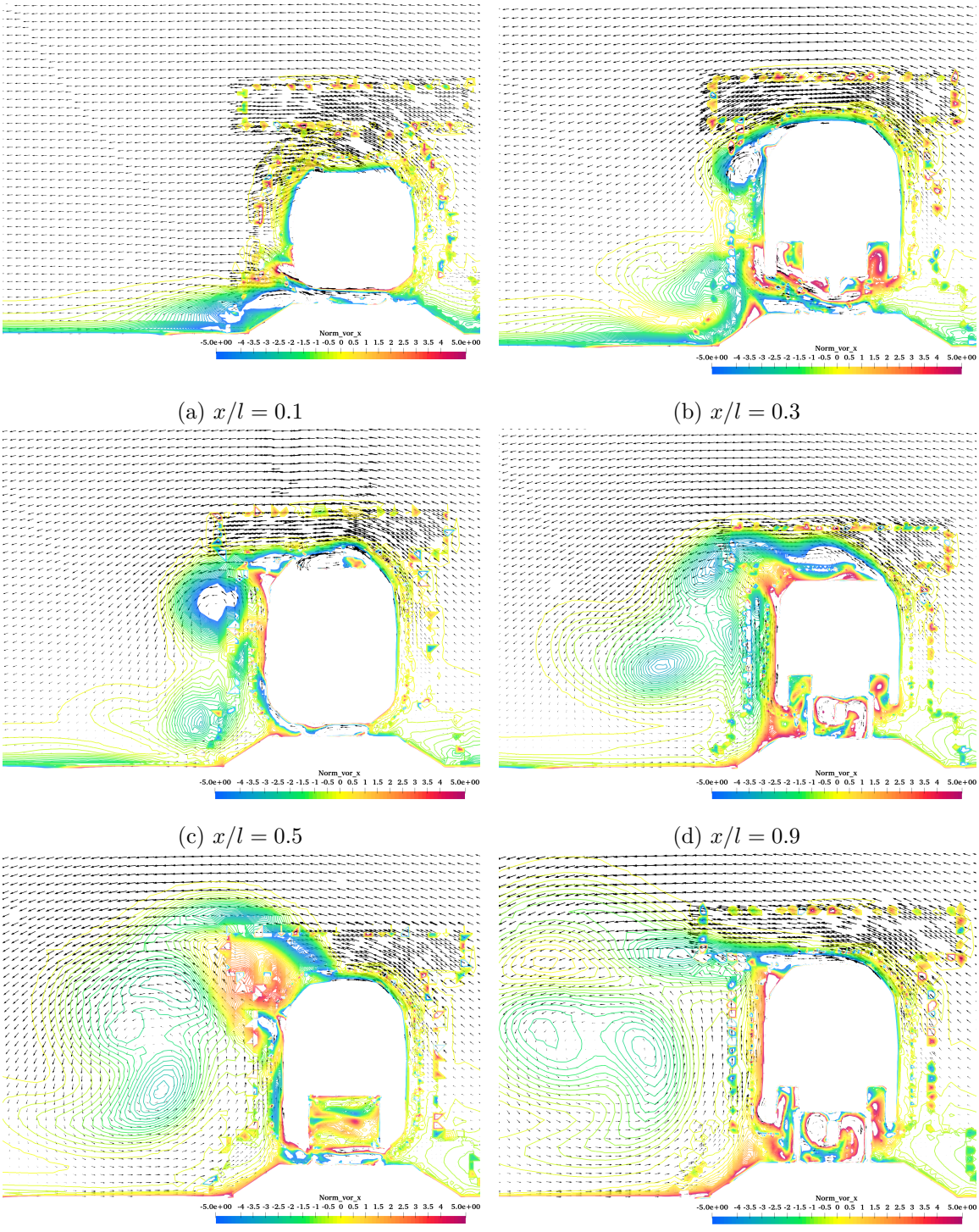

(a) $x/l = 0.1$

(b) $x/l = 0.3$

(c) $x/l = 0.5$

(d) $x/l = 0.9$

(e) $x/l = 1.1$

(f) $x/l = 1.3$

Figure 4.7. Vectors of averaged tangential velocity in the y-z plane and contours of normalized x-component of vorticity at various lengthwise sections for ETR500 train at $\beta = 30°$.

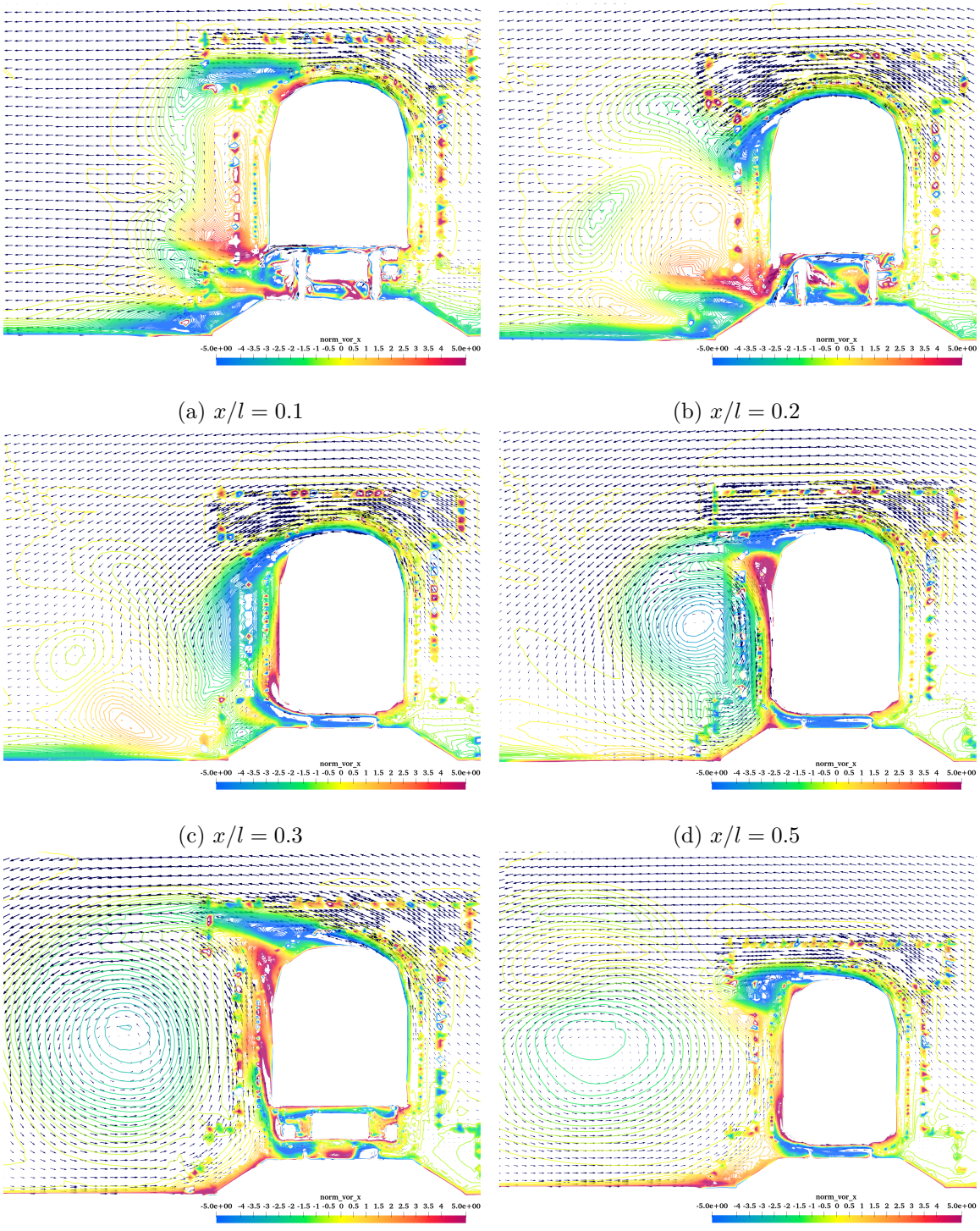

(a) $x/l = 0.1$ (b) $x/l = 0.2$

(c) $x/l = 0.3$ (d) $x/l = 0.5$

(e) $x/l = 0.9$ (f) $x/l = 1.3$

Figure 4.8. Vectors of averaged tangential velocity in the y-z plane and contours of normalized x-component of vorticity at various lengthwise sections for Vivalto train at $\beta = 30°$.

Moreover, the second group has a different behaviour at first sight. Intercity and Regionale trains have a geometrical characteristic in common and that is the larger distance from the bottom floor of the train to the top of the rail, leading to a higher flow rate underneath the cars.

Particularizing for the Intercity train in figure 4.9, at location $x/l = 0.1$ and $x/l = 0.2$ the same behaviour that was observed for Vivalto train happens again. Two recirculation zones created by the abrupt change in geometry appear, leading to the secondary vortices. Then, at $x/l = 0.3$ onwards the phenomenon follows the same pattern than Vivalto train. However, the underneath vortex has a higher strength and size in comparison due to the higher flow rate below the car. This makes that the resulting vortex becomes smaller and weaker and that the break down occurs first. This indeed, explains the lower coefficients obtained in the CFD results and also experimental ones.

Furthermore, Regionale train follows a similar behaviour as seen in picture 4.10. Although, in this case the underfloor is not completely clear from obstructions in the same way as Intercity. This particular condition, makes the flow field such that new vorticity cores are created every time an irregularity is encountered. Small cores are generated and then come together creating a main vortex composed by various cores as seen in picture (f).

This uneven phenomenon makes the flow to become more unsteady with respect to the other railway vehicles. So, as a RANS model is used, more imprecision in the results should be expected, and that is, in fact, what happens. Recalling figure 4.1, coefficients from Regionale are the smaller ones. Also from appendix B, higher errors are proved, and the difference is shown to increase with yaw angles.

Indeed, that group 2 has a bigger inaccuracy as wind incidence angle increases, it is well explained after having analysed the behaviour of the different vortical structures. In fact, for high angles the flow that passes underneath the train increases, making the flow more unsteady in comparison to group 1 and thus increasing the struggle for RANS modelling to obtain good results.

For the sake of completeness, in appendix D, pressure coefficient C_p distributions are shown for every train at various lengthwise sections for a yaw angle $\beta = 30°$. Here, all the analysis already discussed regarding vorticity and its qualitative behaviour can be seen by means of the difference in pressure. ETR500 shows a very small core but presents the higher difference in pressure among the whole set of trains. It is then, very interesting to see how a great difference in pressure does not imply a higher moment or force coefficient if the vortex is not big enough. Also, as some studies have shown, a higher vorticity (and thus force) does not imply a greater depression inside a vortical structure [52].

Nevertheless, the cores forming the different vortical structures are very well represented. For instance, Intercity's pressure field shows two counter vortex forming from the top and the bottom of the leading car as seen before. Also Regional's pressure field is much more complex in comparison to the other vehicles as expected. Lastly, detachment and recirculation zones are better appreciated than before and it can be seen that a higher bypass flow rate separates the vortex earlier.

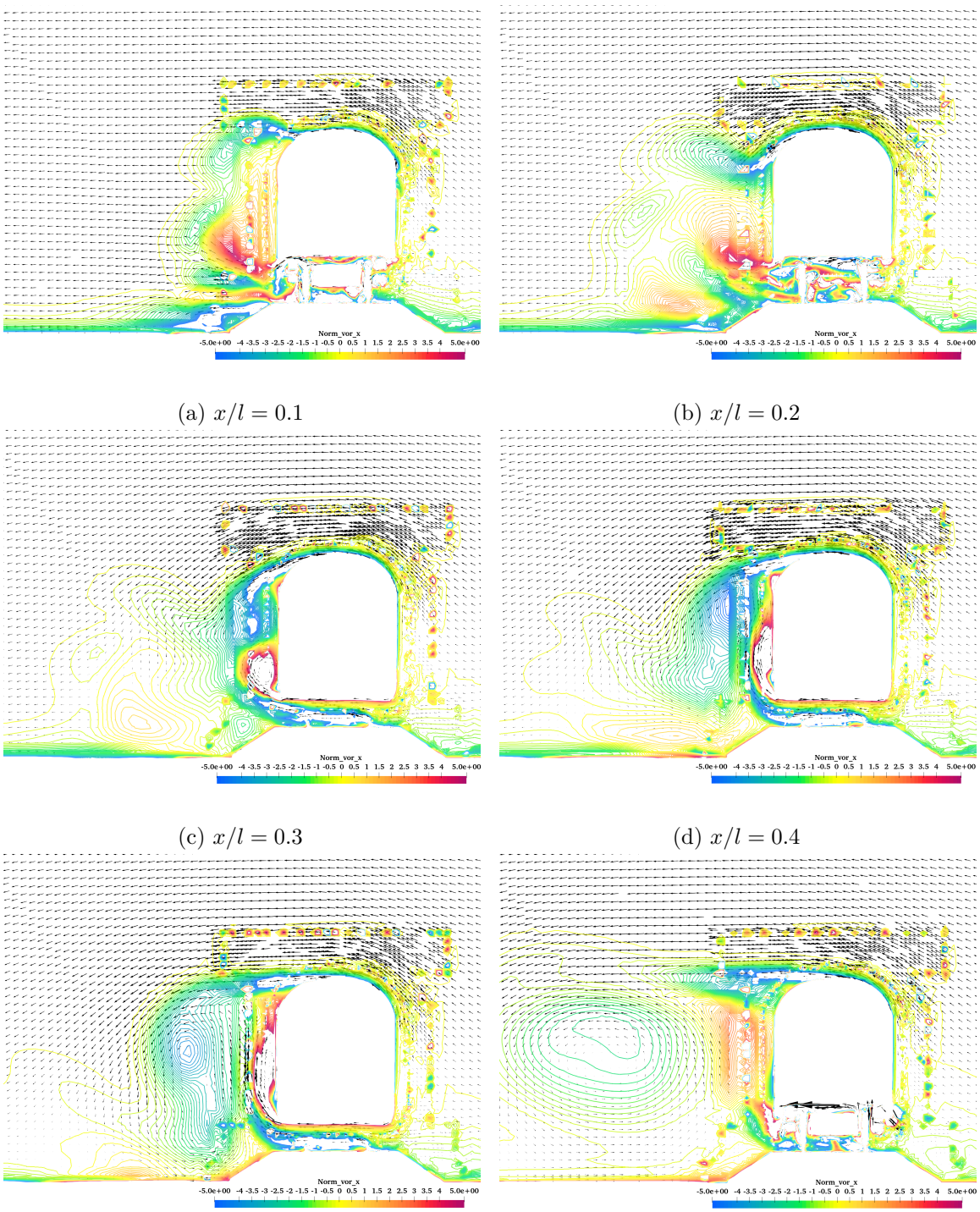

(a) $x/l = 0.1$

(b) $x/l = 0.2$

(c) $x/l = 0.3$

(d) $x/l = 0.4$

(e) $x/l = 0.5$

(f) $x/l = 0.9$

Figure 4.9. Vectors of averaged tangential velocity in the y-z plane and contours of normalized x-component of vorticity at various lengthwise sections for Intercity train at $\beta = 30°$.

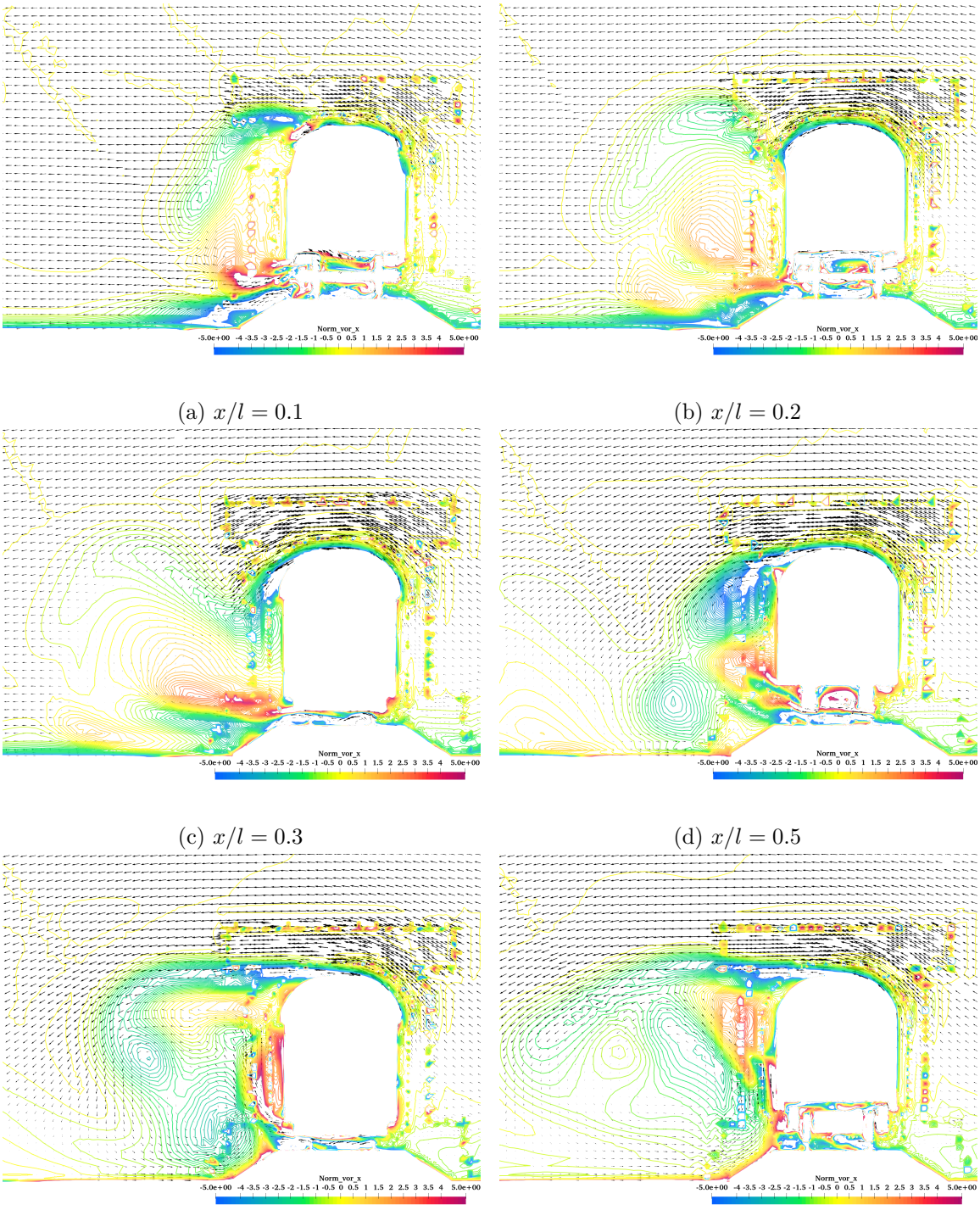

(a) $x/l = 0.1$ (b) $x/l = 0.2$

(c) $x/l = 0.3$ (d) $x/l = 0.5$

(e) $x/l = 0.7$ (f) $x/l = 0.9$

Figure 4.10. Vectors of averaged tangential velocity in the y-z plane and contours of normalized x-component of vorticity at various lengthwise sections for Regional train at $\beta = 30°$.

In figure 4.11, iso-surfaces of vorticity equal to 1000 show the vortical flow structure of the different vehicles for a yaw angle $\beta = 30°$. Here the main differences are greatly appreciated. ETR500 show different vortex shedding generating from the top of the train (MV1 & MV2) and producing the main core on leeward side. Vivalto, Intercity and Regionale show as well that a secondary vortex appears also at the beginning of the second car. In addition, Intercity train confirms that a higher distance from the top of the rail induces the vortex breakdown to occur much earlier than other vehicles and to be more detached from the vehicles leeward side wall.

Now that the main differences are understood, it becomes of utter importance to understand exactly from which points and what kind of geometries induce vortex sheets to be generated. In order to accomplish this understanding, in figure 4.12 the leeward side of the vehicles is coloured by means of Shear stress magnitude. Also, shear stress fluxes are computed on top of the surface to have a better visualization on how the flow behaves on this side of the vehicle. MVSL indicates the main vortex separation line and SVSL the secondary vortex separation line.

The ETR500 presents three main patterns from where the flow detaches and creates the vortices. The main vortex starts on the upper part of the nose of the vehicle and travels downstream, then secondary vortices are generated from the bogies and the sharp corners of the underneath fairing, joining the MV downstream. Also from the upper part which presents sharp corners as well, more vortex shedding is generated.

Regarding conventional trains the vortices start at the very top front corner on the leeward side of the leading car. From there, it divides in to two generating the characteristic lobes at the beginning as seen before, and the main vortex which travels downstream.

It is evident that the underfloor geometries are the main responsible for conditioning the flow behaviour on the leeward side of the train. Intercity train presents the smoother fluxes among all as the bypass flow is much higher and so, the vortical structures detach earlier and are much simpler.

In contrast to this it is regionale train, which presents a much more complex flow because of all the disturbances founded below. It produces many different recirculation zones that contribute to the build up of the vortex core.

Halfway between Regionale and Intercity it is Vivalto. It has a cleaner underfloor but is much closer to the top of the rail so the bogies fairing affect much more in a similar way as ETR500. Hence, it is clear that the underfloor geometry is the main part affecting the flow and vortex shedding structure, followed by the nose shape and the sharp corners that may be found anywhere on the fairing of the vehicle.

Also in appendix D the pressure coefficient distribution is shown at the leeward side of the vehicle. Adverse pressure gradient directions are very clear and match the MVSL and SVSL. It also reflects how pressure distribution may look like along the leeward face and how hard it may be to quantify and relate its effect with moments and forces coefficients' value due to its random and complex distribution. Thus, supporting a vorticity approach as performed in this thesis. Nevertheless, it shall be the common point to understanding wind tunnel results in a more qualitative way, as in the latter pressure gaps are the elements used for measurements.

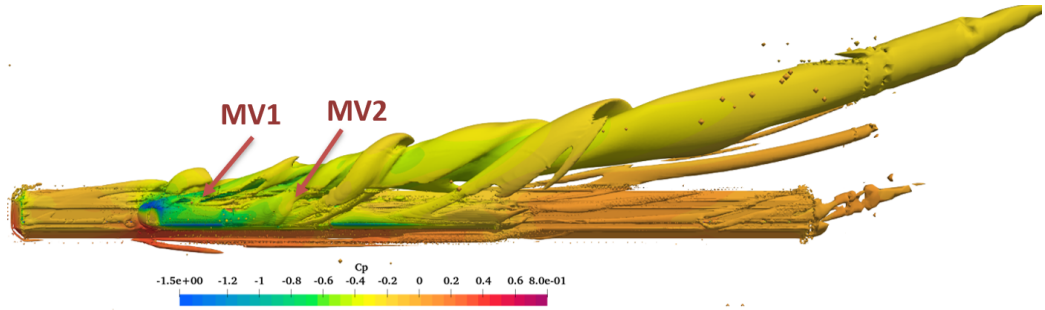

(a) Iso-surfaces of vorticity equal to 1000 coloured by means of the pressure coefficient C_p at $\beta = 30°$ for ETR500 train.

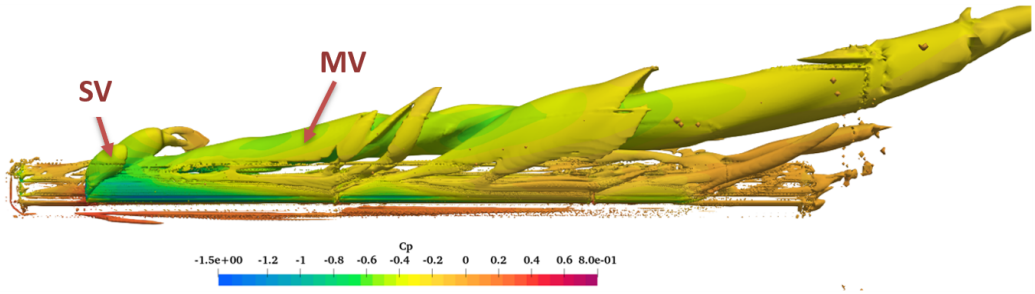

(b) Iso-surfaces of vorticity equal to 1000 coloured by means of the pressure coefficient C_p at $\beta = 30°$ for Vivalto train.

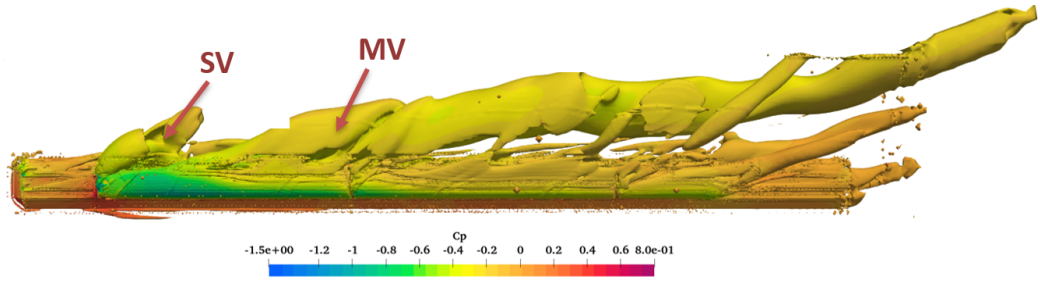

(c) Iso-surfaces of vorticity equal to 1000 coloured by means of the pressure coefficient C_p at $\beta = 30°$ for Regionale train.

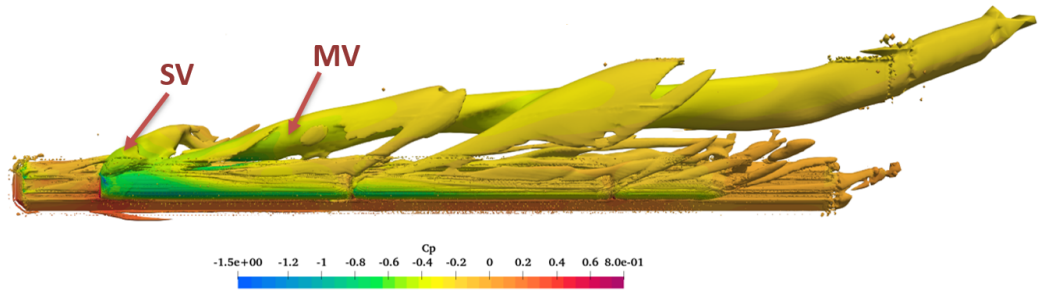

(d) Iso-surfaces of vorticity equal to 1000 coloured by means of the pressure coefficient C_p at $\beta = 30°$ for Intercity train.

Figure 4.11. Iso-surfaces of vorticity equal to 1000 coloured by means of the pressure coefficient C_p at $\beta = 30°$ for every train.

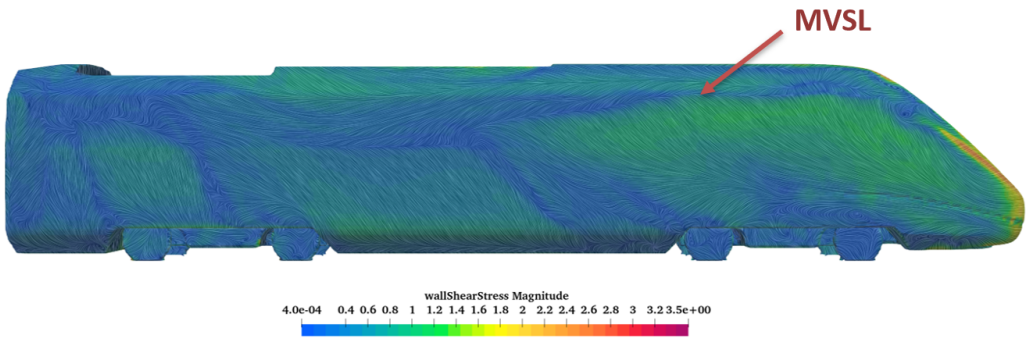

(a) Wall shear stress flux lines coloured by wall shear stress magnitude at the leeward side of ETR500 at $\beta = 30°$.

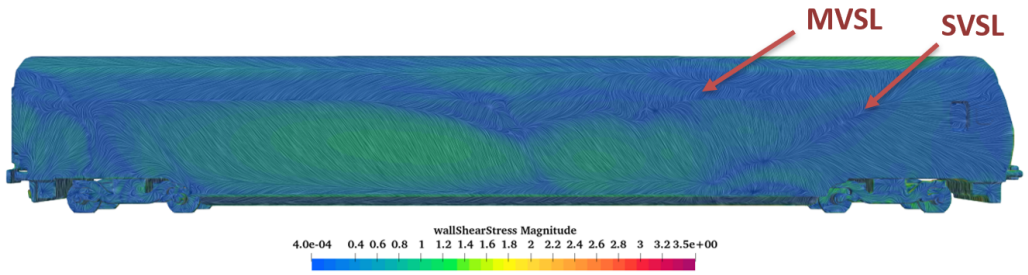

(b) Wall shear stress flux lines coloured by wall shear stress magnitude at the leeward side of Vivalto at $\beta = 30°$.

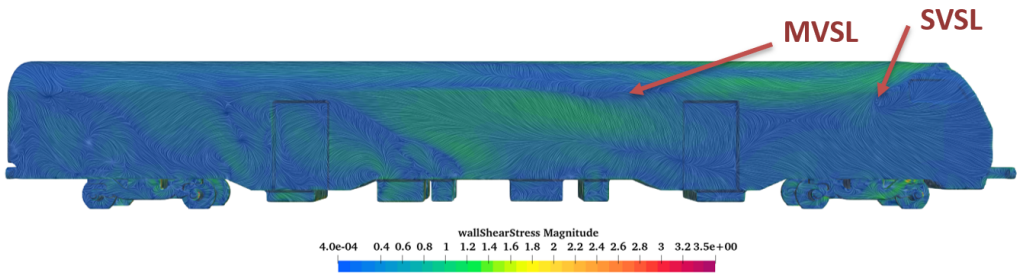

(c) Wall shear stress flux lines coloured by wall shear stress magnitude at the leeward side of Regionale at $\beta = 30°$.

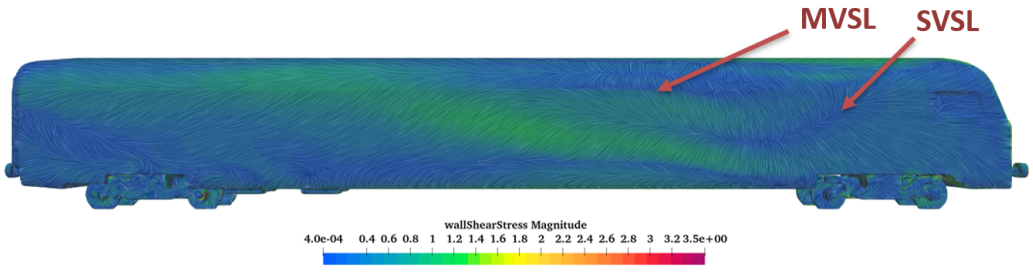

(d) Wall shear stress flux lines coloured by wall shear stress magnitude at the leeward side of Intercity at $\beta = 30°$.

Figure 4.12. Wall shear stress flux lines coloured by wall shear stress magnitude for all leading cars at $\beta = 30°$.

4.3 Results for high yaw angles

To this point, quantitative and qualitative analysis regarding yaw angles below 45 degrees haven performed. Geometrical differences have been studied to understand better the mechanism that take place under cross wind conditions.

CFD results match really well experimental data, although innacuracies depend on the type of vehicle and yaw angle. In fact, as seen in section 4.1, for high yaw angles results do not match that well wind tunnel data and convergence in the simulations is harder to achieve. Also, C_{FZ} does not match experimental results, not even at qualitative level.

Therefore, although a better knowledge on the flow behaviour has been already obtained, a quick overview on the behaviour at these yaw angles will help to understand better and justify with a well formed hypothesis the behaviour noted from wind tunnel tests for lift and lateral force coefficients.

Recalling these results from figure 4.2, the main difference between both groups is founded above 60 degrees. After seeing how much of influence the under car aerodynamics are, the first idea that could explain this dissimilarity in the behaviour of C_{FY} could be precisely the bypass flow relationship.

In fact, the main aerodynamic characteristic at 90 degrees is the mixed Von Kármán structure already discussed. This type of flow field is characterized by an unsteady oscillation of the vortex shedding from the top and bottom of the railway vehicle. Therefore, it is more probable that this phenomenon becomes more intense for train which have a great distance from the bottom to the top of the rail.

Looking at y-z plane contours of normalized x-component of vorticity in figure 4.13, they endorse exactly the hypothesis here presented. For the first group of trains, the vorticity below the vehicle is way smaller in comparison to the second group. Actually, the circulation is pretty significant for the latter. The transition to this secondary type of vortical flow field happens before for Regionale and Intercity, probably becoming the main reason of circulation, and hence, lateral force. Therefore, it is logical that from 60 to 90 degrees the lateral force coefficients remain constant as there must not be much difference on the flow behaviour. In addition, in figure 4.14 iso-surfaces of vorticity reflect as well the importance of the underfloor region. All vehicles behave very similar on the upper part, but differently on the lower. For the ETR500 it is a bit different and shows that the nose shape may have also a great impact on the coefficients at high angles.

Regarding C_{FZ} it is much more complex trying to have a good understanding for the particular behaviour showed in the wind tunnel test, as CFD data is not very reliable. Neither at quality level nor at quantitative. Thus, only hypotheses can be made based on the facts already explained, which should be confirmed and study in further detail in future works. It is of substantial peculiarity that Intercity train which, in turn, is the one with a higher flow rate underneath and a smoother flow, appears to be the vehicle with a smaller lift coefficient. Not only that, but it starts as well to drop and change behaviour at 30 degrees of yaw angle, much before with respect to the others.

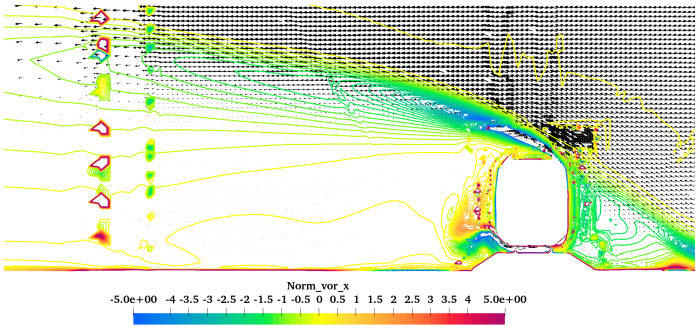

(a) ETR500

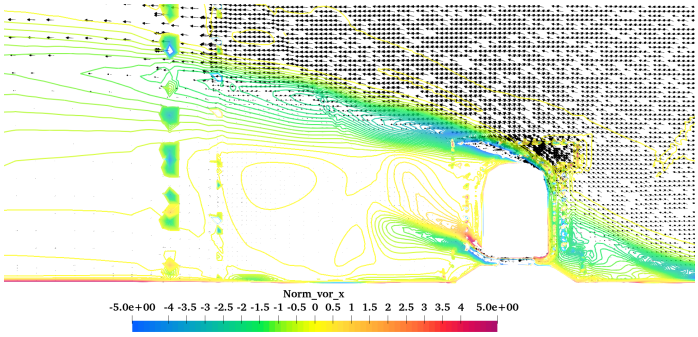

(b) Vivalto

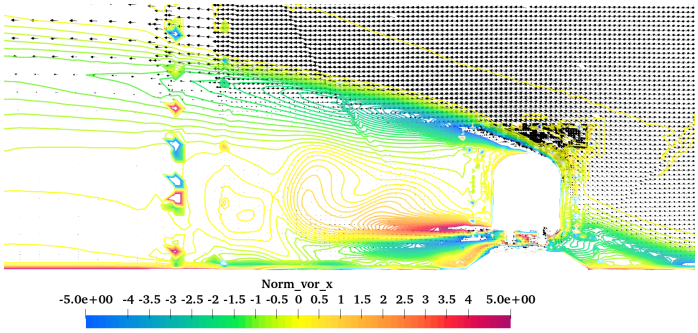

(c) Regionale

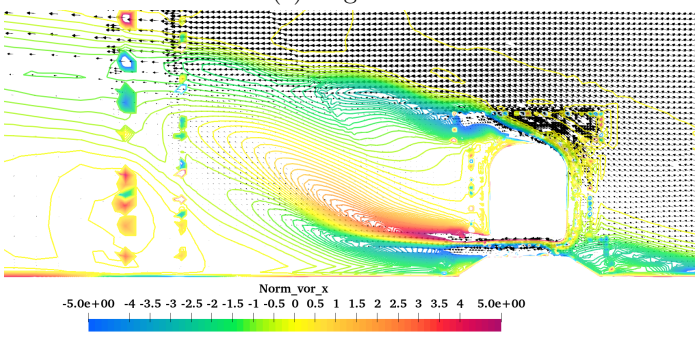

(d) Intercity

Figure 4.13. Vectors of averaged tangential velocity in the y-z plane and contours of normalized x-component of vorticity at $\beta = 90°$ and $x/l = 0.5$ for every train.

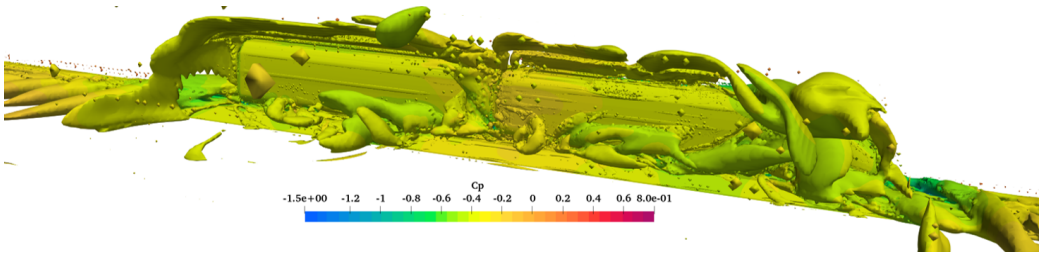

(a) Iso-surfaces of vorticity equal to 2000 on the leeward side coloured by means of the pressure coefficient C_p at $\beta = 90°$ for ETR500 train.

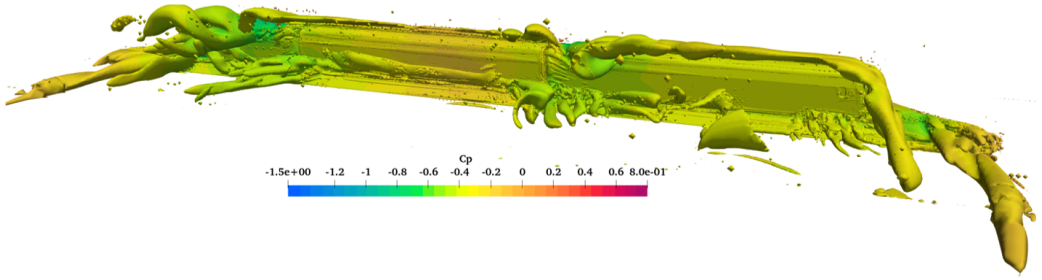

(b) Iso-surfaces of vorticity equal to 2000 on the leeward side coloured by means of the pressure coefficient C_p at $\beta = 90°$ for Vivalto train.

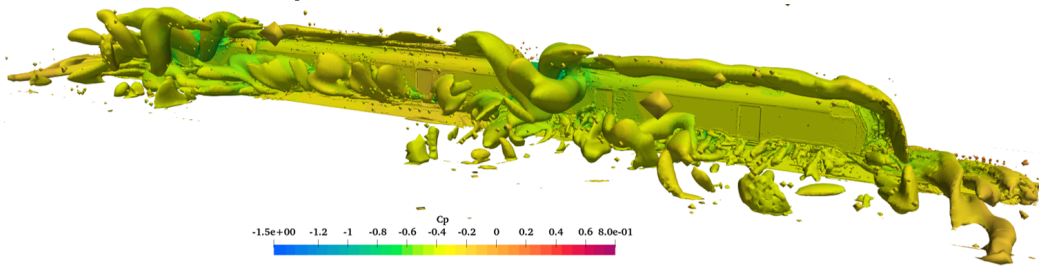

(c) Iso-surfaces of vorticity equal to 2000 on the leeward side coloured by means of the pressure coefficient C_p at $\beta = 90°$ for Regionale train.

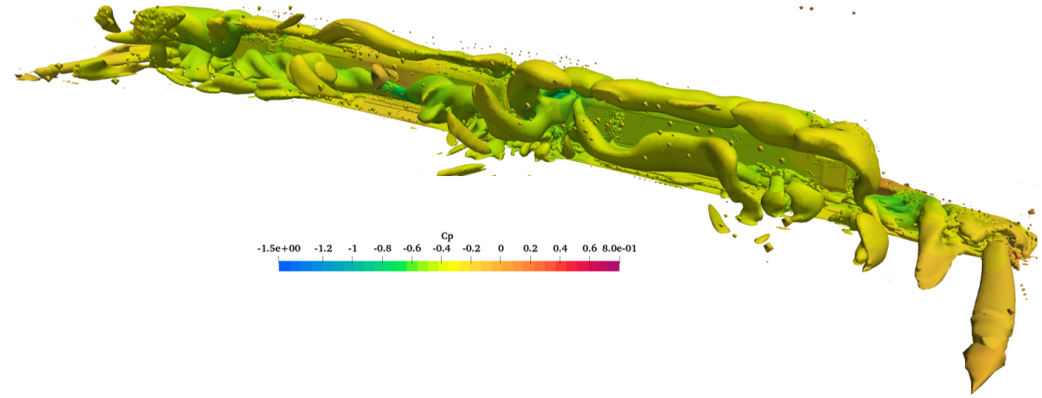

(d) Iso-surfaces of vorticity equal to 2000 on the leeward side coloured by means of the pressure coefficient C_p at $\beta = 90°$ for Intercity train.

Figure 4.14. Iso-surfaces of vorticity equal to 2000 on the leeward side coloured by means of the pressure coefficient C_p at $\beta = 90°$ for each train.

Regionale train follows a similar pattern compared to Intercity, but the blockage of the flow in the longitudinal axis is greater due to the geometries hanging from the bottom floor. This may be the reason for a higher lift coefficient even if the floor is also at a certain distance from the top of the rail. Then Vivalto shows a smaller drop, so, ETR500 should follow as they present in every other case the same behaviour. However, it is not the case. So, as the flow showed in figure 4.14, the shape of the nose may play also an important role in the lift coefficient at high angles of yaw, which is in fact, when results differ from Vivalto behaviour.

4.4 Conclusions

CFD results have shown an acceptable level of accuracy with respect to wind tunnel data. Two segments have been distinguished along the range of yaw angles, together with two different groups of vehicles depending on the coefficients evolution behaviour.

It has been proved that 3 main geometrical characteristic condition the results somehow. These are:

1. Nose shape (streamed or bluff).
2. Lateral underfloor area available for the flow to pass by.
3. Sharp geometries encountered at corners of the fairing (roof or bogies for instance).

Among these three features, the second one has shown to be crucial and the most differentiating one as, in usually, the fairing of conventional trains and their nose shapes are very similar between them. Therefore, lets define it a bit better.

Let then, the geometrical relation:

$$BPR = \frac{h}{c'} \tag{4.5}$$

be the bypass ratio which defines indirectly how much flow passes below the underfloor car, being c' the characteristic height from the top of the train to the top of the rail and h, the characteristic distance from the bottom floor to the top of the rail.

Table 4.1 summarizes the BPRs that correspond to the geometries that have been studied. It could be then established a threshold to determine at which point the transition in behaviour takes place. However, Regionale's BPR shows to be higher with respect to Intercity not matching the results observed. This is because the distance does not take into account that some objects may be hanging from the underfloor and thus, interfering with the flow.

Therefore, a blockage ratio should be added to the equation to account for this factor. A suggested approach is presented in equation 4.6.

$$BPR_{eff} = \varphi \cdot \frac{h}{c'} \cdot (1 - A_{eff}) \tag{4.6}$$

	ETR500	VIVALTO	REGIONALE	INTERCITY
BPR	0.014	0.047	0.197	0.131

Table 4.1. BPRs values for the different trains.

Where A_{eff} is the effective area that the flow has to pass by between bogies and φ a dimensionless constant to tune the values to a rounded number. In addition, the effective area is computed from the ratio of the total underfloor area exposed to the incoming flow (A_{exp}) and the total area of elements that represent some blockage to it (A_b).

$$A_{eff} = \frac{A_b}{A_{exp}} \tag{4.7}$$

Although there is not sufficient and consistent cases to determine a proper criteria, for a matter of completeness, in table 4.2 the effective BPRs for these 4 vehicles is summarized. However, a more in depth study should be performed in order to determine the appropriate threshold that conditions the lateral force and lift coefficients.

	ETR500	VIVALTO	REGIONALE	INTERCITY
$\mathbf{BPR_{eff}}$	0.15	0.52	1.18	1.44

Table 4.2. Effective By Pass Ratios BPR_{eff}.

For these cases, the value of φ has been set to be equal to 12. Looking at the numerical results obtained, the formula has proved to provide more coherent values. In fact, a threshold could be set for a $BPR_{eff} = 1$, belonging the trains which obtain a $BPR_{eff} < 1$ to group 1, and a $BPR_{eff} > 1$ to group 2. Also, the higher the BPR_{eff}, the lower it is C_{FZ} for high yaw angles.

Lastly, as there is some difference between values, it seems at first sight that C_{FY} may be less sensitive to changes in BPR_{eff} with respect to C_{FZ}.

Chapter 5

Conclusions and Future Work

In this chapter the conclusions obtained from the work performed in this thesis are presented. In addition, some suggestions for possible future works are made, as the complete understanding of the mechanism that rule the aerodynamics of railway vehicles under crosswind are yet far to be completely understood.

5.1 Conclusions

This thesis has assisted the crosswind modelling problem for conventional trains by means of CFD tools. In particular, CEN standards have been followed thoroughly to develop a model that may be used to help with *Virtual Homologation* (VH) of Conventional railway vehicles.

As suggested by CEN norms [12], RANS approach with a $k-\omega$ SST turbulence modelling has been chosen. Then, a sensitivity analysis for the mesh has been carried out to determine the best size/accuracy relationship for the grid, being the extra-fine the one used. Afterwards, CFD results obtained for the ETR500 where compared to EN14067-6 data, validating the model after fulfilling the $\epsilon < 15\%$ restriction for $C_{MX,lee}$.

CFD analysis where then performed for three different types of conventional trains. Three geometrical features were differentiating: flat shape noses, underfloor distance to the top of the rail and sharp edges and corners in the fairing. Results where compared to wind tunnel data and validated. For the whole spectrum of yaw angles (0 to 90 degrees), the model satisfied EN14067-6 restrictions only for wind incidence angles below 30 degrees. For higher values, unsteady aerodynamics gains relevance and so, RANS model does not comply in accuracy. Nevertheless, errors were not well above the threshold value and so, a qualitative analysis could be conducted for that interval.

Forces and moments coefficients curves could be divided in two phases. Small yaw angles (below 45 degrees) and high yaw angles (above 45 degrees). In addition to this division, depending on the behaviour at high angles two groups may be differentiated as well: group 1 (ETR500 & Vivalto) and group 2 (Regionale & Intercity).

For the first segment of β values, all the trains presented a similar behaviour in terms of lateral forces. It was verified that the strength and size of the vortical structure found on the leeward side is proportionally related to the aerodynamic coefficients, except for C_{FZ}. The latter starts changing its behaviour at 30 degrees, depending on the type of leading car. It is worth highlighting as well that vortex intensity, break down or core composition depend on these three geometrical attributes that were compared. For instance, streamed nose shapes reduce vortex size and delays its appearance, high by pass ratio underfloors bring forward the vortex detachment and sharp geometries induce more complex flow structures that may or may not help to increase or decrease forces coefficients. These results prove that, for small yaw angles, flow structure may differ a bit depending on geometry which in turn reflects the disagreement found in literature.

Moreover, for the second section (i.e. $\beta > 45°$), there is a clear segmentation among the different vehicles. The reason to this is underpinned by the underfloor aerodynamics, specifically the Bypass Ratio (BPR_{eff}). While group 1 sees its lateral force coefficient reduced, group 2 sees it remaining constant due to the flow passing underneath the leading car. Besides, the transition to a mixed Von Kármán vortical structure happens first for this second set of trains, gaining unsteadiness more presence and thus error in RANS simulations.

Finally, but not least, an initial proposal for quantifying and characterizing the effect of the bypass ratio has been presented. The Effective By Pass Ratio (BPR_{eff}) approaches this phenomenon by means of geometrical features. Namely, the ratio between characteristic height from the top of the train to the top of the rail, characteristic height from the top of the underfloor to the top of the rail, effective lateral area available for the flow to pass underneath the leading car and a dimensionless constant. When a bypass ratio is higher than one ($BPR_{eff}>1$) a behaviour similar to group 2 should be expected. Whereas, if the ratio is below one ($BPR_{eff}<1$), then group 1 behaviour takes place.

In conclusion, the way CEN standards approaches *Virtual Homologation* for conventional trains in crosswind conditions may not be sufficient, as the errors increase significantly and are not norm compliant for high yaw angles. A more complex modelling is needed to account for the unsteadiness of the flow which is, indeed, more relevant in conventional trains.

5.2 Future work

Results hereby presented have brought some interesting possibilities for future works. Two lines of further investigation can be established: CFD modelling improvement to achieve better accuracy in the results to enhance *Virtual Homologation*, and development of a set of various trains accounting for geometrical differences. The latter, pursuing to obtain a better comprehension on the geometrical factors that determine vorticity under crosswind conditions and thus, forces and moment coefficients.

Firstly, though already suggested in [19], this thesis has confirmed that RANS modelling is not sufficient for conventional trains at high angles of yaw if *Virtual*

Homologation is pursued. Also, although within limits by little, big errors at low yaw angles are present. Moreover, underfloor aerodynamics have shown to be crucial for computing properly lift coefficient. Therefore, a model that contemplates unsteady aerodynamics and higher precision on the boundary layer should be considered. Thus, the author proposes a Detached Eddy Simulation (DES) approach with URANS equations close to the wall and a $k-\omega$ SST turbulence model. Also, as the model becomes time dependent, as some studies suggest [53], $y^+ = 1$ should be highly respected. To enhance computational cost, model could be initialized from RANS results. This proposal is also based on results performed in the AeroTRAIN project which proved DES had better accuracy. In addition, transition between mesh refinements should be improved and made smoother as vorticity figures showed some irregularities at transition layers.

Secondly, although many studies have been performed for crosswind, it is not clear yet what are the main mechanisms that rule aerodynamics of railway vehicles under crosswind conditions. In particular, flow field structure. Nevertheless, 3 general geometrical features have shown to play an important role. Therefore, the following steps to tackle this challenge are proposed:

1. Different sets of conventional trains should be developed maintaining constant nose geometry, characteristic height and smooth fairing and changes only in the bypass ratioBPR_{eff} should be done so that proper criteria on the influence of this parameter may be established.

2. Then, another set that maintains constant $BPR_{eff} = 1$ and fairing geometry should be developed, so that only changes in the nose shape are done and hence, a deeper understanding on its influence is obtained.

3. Lastly, for a reference nose shape and BPR_{eff}, changes in the fairing at critical areas like bogies or car roof should be attempted to comprehend better its direct relation with the flow.

Appendix A

Mathematical model

A.1 Navier-Stokes equations for incompressible flow

To describe the motion of fluids, Navier-Stokes equation may be used. In particular, mass-conservation or continuity equation as shown in equation A.1, and momentum equations summarized in equation A.2.

$$\frac{\partial \rho}{\partial t} + \nabla \cdot (\rho \mathbf{U}) = 0 \tag{A.1}$$

$$\underbrace{\rho \frac{\partial \mathbf{U}}{\partial t}}_{I} + \underbrace{\rho(\mathbf{U} \cdot \nabla)\mathbf{U}}_{II} = \underbrace{-\nabla p}_{III} + \underbrace{\lambda \nabla(\nabla \cdot \mathbf{U}) + \mu[\nabla^2 \mathbf{U} + \nabla(\nabla \cdot \mathbf{U})]}_{IV} + \underbrace{\rho f_B}_{V} \tag{A.2}$$

Where $\mathbf{U}$ is the velocity vector with three components $[u \quad v \quad w]^T$, p is the pressure, ρ is the density of the fluid, μ is the fluid dynamic viscosity and for monoatomic fluids [34] $\lambda = -\frac{2}{3}\mu$, also known as *Stoke's relation*. The physical interpretations for each term of the equation are:

- **I**: Velocity variation with time.
- **II**: Convection term.
- **III**: Pressure forces.
- **IV**: Diffusion term.
- **V**: Mass forces.

For steady and incompressible flows, i.e. flows with a Mach number $M_\infty = \frac{U_\infty}{c_\infty} < 0.3$, Navier-Stokes equations can be simplified as density and viscosity are considered to

be constant. In this case, equation A.1 degenerates to a kinematic condition that sets the velocity field to be solenoidal or divergence-free [35]:

$$\nabla \cdot \mathbf{U} = 0 \tag{A.3}$$

Whereas, momentum equation can be simplified and condensed in the following form:

$$\rho \frac{\partial \mathbf{U}}{\partial t} + \rho(\mathbf{U} \cdot \nabla)\mathbf{U} = -\nabla p + \mu \nabla^2 \mathbf{U} + \rho \mathbf{g} \tag{A.4}$$

However, for sake of convenience regarding literature of CFD, the momentum equation that will be considered throughout this document will be equation A.5, where it has just been rearranged considering Stoke's relation.

$$\frac{\partial(\rho \mathbf{U})}{\partial t} + \nabla \cdot (\rho \mathbf{U}\mathbf{U}) = -\nabla p + \nabla \cdot (\mu((\nabla \mathbf{U}) + (\nabla \mathbf{U}^T))) - \frac{2}{3}\mu(\nabla \cdot \mathbf{U})\mathbf{I} + \rho \mathbf{g} \tag{A.5}$$

Lastly, a third equation should be introduced, although is rarely solved in its full form as, depending on the problem, simplifications are usually done. However, for completeness is presented in equation A.6 and that is the energy equation.

$$\frac{\partial}{\partial t}(\rho c_p T) + \nabla \cdot (\rho c_p \mathbf{U} T) = \nabla \cdot (k \nabla T) + Q^T \tag{A.6}$$

A.2 Reynolds-Averaged Navier Stokes (RANS) equations

A.2.1 Introduction

When deriving the Navier-Stokes equation in subsection A.1, there was no mention at all in differentiating whether the velocity profile was laminar or turbulent. This is a very important fact that needs to be taken into account as turbulent flows are chaotic and unstable, diffusive causing rapid mixing, time-dependent, and involve three-dimensional vorticity fluctuations with a broad range of time and length scales [36].

Turbulence, according to the "energy cascade" theory proposed by Kolmogorov [37, 38], is composed of eddies of different sizes and energies. Is a chain process between smaller and bigger ones. Based on this cascade concept, very small time steps and mesh size would be needed to solve the whole temporal and spacial spectrum.

It does exist a technique called Direct Numerical Simulations (DNS), which as it names states, solves directly the Navier-Stokes equations. However, it involves a huge amount of cost in computational resources [36] which makes it infeasible for the current computational capacity that is present nowadays.

As an alternative, statistical analysis can be used to simplify the computation of turbulent flows. In fact, a Large Eddy Simulation (LES) lays in between DNS and RANS methodologies. It consists [39] on directly computing large scale eddies while smaller ones are approached by using sub-grid scale models.

Another methodology which is also gaining interest and was first suggested by Spalart [40] is the Detached Eddy Simulation, or DES. It is a hybrid model in between RANS and LES, which applies LES equations for a certain region apart from the surface, and RANS model close to the wall. This mixed model is less costly in terms of computational requirements in comparison to LES and has more precision than RANS, which makes it very interesting as an alternative way of solving cases when, for instance, the flow is highly unstable due to the physics of the problem.

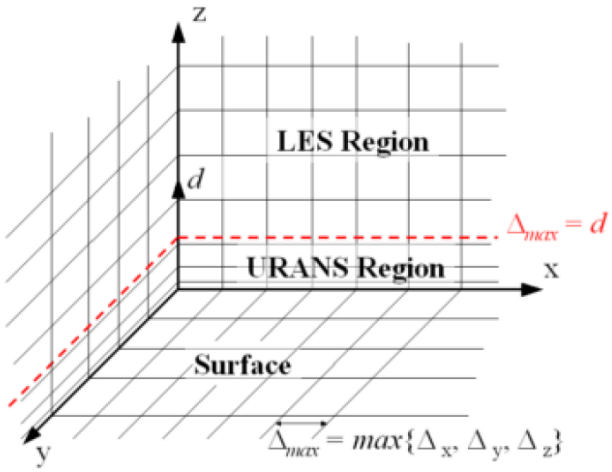

Figure A.1. Formulation of DES on a structured grid [10]

Nevertheless, the most popular way of approaching this challenge at industrial level is by using the Reynolds Averaged Navier-Stokes (RANS) equations. In this case, the averaged is not done at spacial level but rather in time [41]. Specifically, it decomposes the flow variables into a time-mean value component and a fluctuating one, substitutes in the original equations and time-averaging the obtained equations, making the mesh size limitation not as restrictive as DNS or LES.

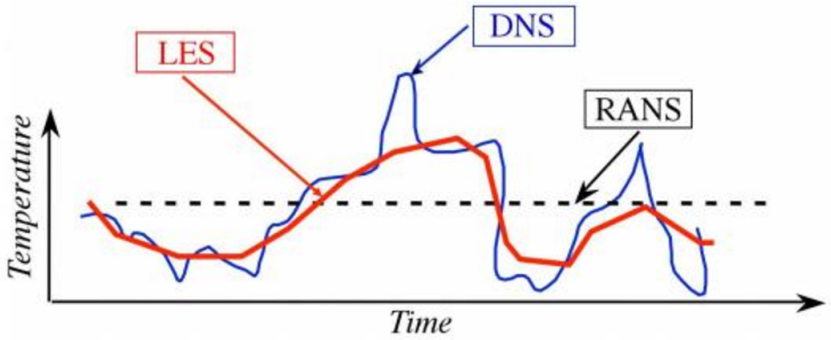

Figure A.2. Representation of the expected temporal evolution of a variable modelled by RANS, LES and DNS approaches.

As for the reasons here exposed, RANS will be the approach chosen to handle the challenge pursued in this thesis.

A.2.2 Reynolds Averaging

RANS equations consist in taking the absolute value of any of the variables implied and decompose it in a mean and fluctuating value. Let ϕ be any flow variable ($\mathbf{U}, p, e, h, T, \rho, etc.$), then the decomposition is such that:

$$\phi(\mathbf{x},t) = \underbrace{\overline{\phi}(\mathbf{x},t)}_{\text{mean value}} + \underbrace{\phi'(\mathbf{x},t)}_{\text{fluctuating value}} \tag{A.7}$$

For RANS equations, the averaging performed is regarding time, i.e. the average of a quantity which does not vary with time so that it is suitable for steady turbulent flows. Equation A.8 shows how it should be computed, although if the variable ϕ changes slowly in time in comparison with the time scale of turbulent fluctuations, equation A.9 may be used [42].

$$\overline{\phi}(\mathbf{x}) = \lim_{T\to\infty} \frac{1}{T} \int_t^{t+T} \phi(\mathbf{x},t)dt \tag{A.8}$$

$$\overline{\phi}(\mathbf{x},t) = \frac{1}{T} \int_T^{t+T} \phi(\mathbf{x},t)dt \tag{A.9}$$

Moreover, for the process of averaging Navier-Stokes equations, some properties or rules must be considered. In fact, if ϕ and φ are two variables, and ϕ' and φ' their fluctuating components, the following rules apply [42]:

$$\begin{aligned}
\overline{\phi'} &= 0 \\
\overline{\phi} &= \overline{\overline{\phi}} \\
\overline{\nabla\phi} &= \nabla\overline{\phi} \\
\overline{\phi+\varphi} &= \overline{\phi} + \overline{\varphi} \\
\overline{\overline{\phi}\varphi} &= \overline{\phi}\,\overline{\varphi} \\
\overline{\overline{\phi}\varphi'} &= 0 \\
\overline{\phi\varphi} &= \overline{\phi}\,\overline{\varphi} + \overline{\phi'}\,\overline{\varphi'}
\end{aligned} \tag{A.10}$$

Hence, assuming a newtonian fluid and taking the time average for incompressible Navier-Stokes equations, equations A.3, A.5 and A.6 are transformed into:

$$\overline{\nabla \cdot [\rho(\overline{U} + U')] = 0} \tag{A.11}$$

$$\begin{aligned}\overline{\frac{\partial(\rho(\overline{U}+U'))}{\partial t}+\nabla\cdot\rho(\overline{U}+U')(\overline{U}+U')=-\nabla(\overline{p}+p')}\\ \overline{+\nabla\cdot\left\{\mu\left(\nabla(\overline{U}+U')+(\nabla(\overline{U}+U'))^T\right)\right\}+\mathbf{f}_b}\end{aligned} \tag{A.12}$$

$$\overline{\frac{\partial(\rho c_p(\overline{T}+T'))}{\partial t}+\nabla\cdot(\rho c_p(\overline{\mathbf{U}}+\mathbf{U'})(\overline{T}+T'))=\nabla\cdot(k\nabla(\overline{T}+T'))+S^T} \tag{A.13}$$

Computing the equations above, the Reynolds averaged forms are obtained as:

$$\nabla\cdot(\rho\overline{\mathbf{U}})=0 \tag{A.14}$$

$$\begin{aligned}\frac{\partial(\rho\overline{\mathbf{U}})}{\partial t}+\nabla\cdot(\rho\overline{\mathbf{U}}\overline{\mathbf{U}})=-\nabla p+\nabla\cdot\left[\mu\left(\nabla\overline{\mathbf{U}}+(\nabla\overline{\mathbf{U}})^T\right)\right]\\ +\rho\mathbf{g}-\nabla\left(\frac{2}{3}\mu(\nabla\cdot\overline{\mathbf{U}})\right)-\underbrace{\nabla\cdot\left(\overline{\rho\mathbf{U'}\mathbf{U'}}\right)}_{\text{Reynolds-stress}}\end{aligned} \tag{A.15}$$

$$\frac{\partial(\rho c_p\overline{T})}{\partial t}+\nabla\cdot(\rho c_p\overline{\mathbf{U}T})=\nabla\cdot(k\nabla\overline{T}-\rho c_p\overline{\mathbf{U'}T'})+\overline{S^T} \tag{A.16}$$

From the process of averaging a new term appears and is called Reynolds-stress, which is a consequence of the fluctuating velocity. This new term is unknown, therefore, in order to close the equations, it has to be modelled by means of variables and constants that are known. This is achieved by employing Boussinesq hypothesis [42] which relates the Reynolds-stress with the mean velocity gradients as shown in equation A.17.

$$\underbrace{\overline{\rho\mathbf{U'}\mathbf{U'}}}_{\text{Reynolds-stress}}=\mu_t\underbrace{\left(\nabla\overline{\mathbf{U}}+(\nabla\overline{\mathbf{U}})^T\right)}_{\text{Mean Velocity Gradients}}-\frac{2}{3}\rho k\mathbf{I}-\frac{2}{3}(\nabla\cdot\overline{\mathbf{U}})\mathbf{I} \tag{A.17}$$

As it can be seen, the Reynolds-stress is related to the mean velocity gradients through the turbulent viscosity μ_t or dynamic eddie viscosity. Hence, once μ_t is known, the boussinesq hypothesis can be computed and equation A.15 can be approached.

In order to do so, many different models have been developed throughout the years and they can be classified in four different categories:

- Algebraic (Zero-Equation) Models
- One-Equation Models
- Two-Equation Models

- Second-Order Closure Models

Nevertheless, non of them is universally applicable and the choice will depend on the flow conditions. Therefore, for the issue at hand, only $k-\epsilon$, $k-\omega$ and $k-\omega$ SST models will be explained, not only because they might be the most popular ones, but because they are recommended by EN14067-6 norms [12].

A.2.3 k-epsilon ($k-\epsilon$) model

The $k-\epsilon$ model stands inside the group of two-equations models as it defines the turbulent viscosity in terms of turbulent kinetic energy k and turbulence dissipation rate ϵ as shown in equation A.18. Where both variables are solved using two transport equations.

$$\mu_t = C_\mu \frac{\rho k^2}{\epsilon} \tag{A.18}$$

The transport equation for k is shown in equation A.19, and it is worth noticing that it is the same equation for all the different variants of the k-epsilon model, i.e. for the RNG, realizable and standard, although the focus will be put in the standard model as it is the most common.

$$\underbrace{\frac{\partial(\rho k)}{\partial t}}_{\text{Time}} + \underbrace{\nabla\cdot(\rho \mathbf{U} k)}_{\text{Convection}} = \underbrace{\nabla\cdot\left[\left(\mu + \frac{\mu_t}{\sigma_k}\right)\nabla k\right]}_{Diffusion} + \underbrace{P_k + P_b - \rho\epsilon + S_k}_{\text{Sources+Sinks}} \tag{A.19}$$

Where the sources and sinks are P_k which reflects the production due to mean velocity shear, P_b which accounts for the production due to buoyancy and S_k which is left as a possible user-defined sink. Notice the minus sign for the dissipation rate, which proves that it is actually trying to dissipate the turbulent kinetic energy.

The difference between the various models relays on the transport equation for the dissipation rate, but as said, the focus will be given for the standard model and hence, the transport equation is stated in equation A.20.

$$\underbrace{\frac{\partial(\rho\epsilon)}{\partial t}}_{\text{Time}} + \underbrace{\nabla\cdot(\rho \mathbf{U} \epsilon)}_{\text{Convection}} = \underbrace{\nabla\cdot\left[\left(\mu + \frac{\mu_t}{\sigma_\epsilon}\right)\nabla \epsilon\right]}_{Diffusion} + \underbrace{C_1\frac{\epsilon}{k}(P_k + C_\mu P_b) - C_2\rho\frac{\epsilon^2}{k} + S_\epsilon}_{\text{Sources+Sinks}} \tag{A.20}$$

The main characteristic that distinguishes one model from another, are the values of the empirical coefficients C_1, C_2 and C_μ, which do not only change between models but have also evolved with time. These values are summarized in table A.1

Furthermore, it has been seen experimentally that eddies are affected when close to the wall in a way that reduces their size and strength. In order to account for this phenomenon, damping functions must be introduced to the model to control the

Model	σ_k	σ_ϵ	C_1	C_2	C_μ
Jones & Launder (1972)	1.0	1.3	1.55	2.0	0.09
Launder & Spalding (1974)	1.0	1.3	1.44	1.92	0.09
Launder & Sharma (1974)	1.0	1.3	1.44	1.92	0.09

Table A.1. $k-\epsilon$ model coefficients taken from [14–16]

dissipation rate when approaching a surface. Specifically, they are introduced to damp the coefficients C_1, C_2 and C_μ, therefore, the names given to these damping functions are f_1, f_2 and f_μ.

This allows, in theory, that the $k-\epsilon$ model could be applied all the way down to the wall, i.e. the equations could be solved even when the first cell lays within the viscous sub-layer ($y^+ < 5$). To this formulation, the name *low-Re formulation* is given.

In the standard $k-\epsilon$ model, the damping functions are the ones presented in equations A.21, A.22 and A.23. Where Re_T is the turbulent Reynolds number as shown in equation A.24.

$$f_1 = 1 \tag{A.21}$$

$$f_2 = 1 - 0.3exp(-Re_T^2) \tag{A.22}$$

$$f_\mu = exp\left(\frac{-3.4}{(1+(Re_T/50))^2}\right) \tag{A.23}$$

$$Re_T = \frac{\rho k^2}{\mu\epsilon} \tag{A.24}$$

The fact that Re_T is present in two damping functions is the key point for the low Reynolds formulation of the model, as it implies the proper behaviour of the model when close to the wall by making the factors smaller than 1 and hence, damping the corresponding terms in the transport equation for ϵ. So, for cells where Reynolds number is low (viscous forces are dominant), it is said to be using a low-Re number formulation, whereas far from a surface, Reynolds number tend to be large and therefore a high-Re formulation is used.

However, this is an old model firstly developed back in 1972, and so nowadays other turbulence models like the $k-\omega$ SST are preferred if the physics of the problem require more precise wall shear stress computation. Although, for high Reynolds simulation and where high separation and reattachments are no present, the $k-\epsilon$ is still well accepted among the community.

A.2.4 k-omega ($k-\omega$) model

As mentioned before, the lack of accuracy in the $k-\epsilon$ when trying to predict boundary layers where adverse pressure gradients are present and hence, detachments of the flow, motivated the need of developing a new model that could tackle this problem.

A wide variety of solutions to asses this challenge where proposed like the Spalart-Allmaras, Johnson-King or $k-\omega$ models. Not only that, but also even many different versions of the $k-\omega$ where suggested. However, the most commonly used is the latter and the focus will be put in it.

To further deepen the understanding of the model, the difference between the $k-\epsilon$ and $k-\omega$ models lays precisely in the definition of ω. Where as ϵ is the turbulence dissipation rate (units m^2/s^3), ω is the specific turbulence dissipation rate (units $1/s$). Nonetheless, they are directly linked to each other by the mathematical definition of ω and both variables mean dissipation of turbulence:

$$\omega = \frac{\epsilon}{C_\mu k} \qquad C_\mu = 0.09 \tag{A.25}$$

In fact, where both ω and ϵ are high, is where there is a high dissipation of turbulent kinetic energy, as recalling its transport equation A.19, the term is presented as a sink.

Another key point of the model is that, either a transport equation for ω or ϵ can be solved, as both are directly related through equation A.25, allowing easy conversion between each other.

But, it is in this transport equation for ω (eq: A.26) where the difference lays, as the empirical coefficients can change.

$$\frac{\partial(\rho\omega)}{\partial t} + \nabla\cdot(\rho\mathbf{U}\omega) = \nabla\cdot\left(\left(\mu + \frac{\mu_t}{\sigma_k}\right)\nabla\omega\right) + \frac{\gamma}{\nu_t}P_k - \beta\rho\omega^2 \tag{A.26}$$

At this point, a natural question should have arised and that is why does the $k-\omega$ capture much better the flow detachments if the equations are so similar and directly connected. This difference is largely due to its dependence on the empirical damping functions which are critical for the accuracy of the model, and is precisely there where the $k-\epsilon$ misses the point in the presence of adverse pressure gradients, whereas $k-\omega$ does not need these damping functions.

Nevertheless, $k-\omega$ also has its own weakness and that is its dependence and sensitiveness on the freestream turbulence conditions [11, 43]. In fact, [11] proved that small changes in freestream kinetic energy k_∞ lead to large changes in turbulent viscosity μ_t and skin friction coefficient c_f which may also alter forces on the body and flow separation inception.

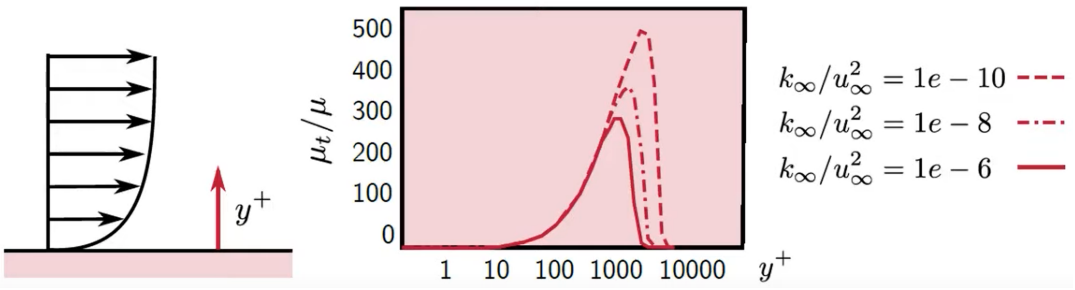

Figure A.3. Turbulence viscosity change with wall distance for different freestream turbulent kinetic energy [11]

To try to solve this problem, a blending solution was proposed. The idea is to combine the advantages of both, $k-\epsilon$ and $k-\omega$ models by using the first one in the freestream region (as it is not sensitive to changes in kinetic energy) and the latter close to the wall region where its performance outperforms the $k-\epsilon$ model.

This is the basis for the $k-\omega$ SST model.

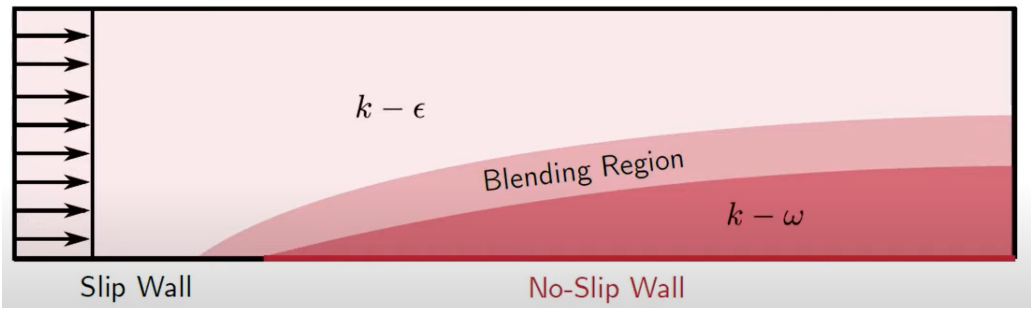

Figure A.4. Blending scheme between $k-\epsilon$ and $k-\omega$ models [11]

Since 1988, it has been suggested that $k-\omega$ is missing the cross-diffusion term in equation A.27, while others [11] suggest that the model coefficients $(\alpha, \beta, \beta*, \sigma_k, \sigma_\omega, \sigma_{\omega 2})$ are not tuned correctly. As it is not entirely clear yet, the $k-\omega$ SST model is preferred.

$$2\frac{\rho\sigma_{\omega 2}}{\omega}\frac{\partial k}{\partial x_j}\frac{\partial \omega}{\partial x_j} \tag{A.27}$$

A.2.5 k-omega SST ($k-\omega$ SST) model

Recalling the previous chapters, it has been argued how the $k-\omega$ SST model appears as an improvement for both, $k-\epsilon$ and $k-\omega$ models.

Recalling equation A.20, if $\epsilon = C_\mu k\omega$ is substituted in the transport equation, equation A.28 is obtained. The fact is, that if compared to equation A.26, the only

difference lays on this additional term at the end.

$$\frac{\partial(\rho\omega)}{\partial t} + \nabla \cdot (\rho \mathbf{U}\omega) = \nabla \cdot \left(\left(\mu + \frac{\mu_t}{\sigma_k} \right) \nabla\omega \right) + \frac{\gamma}{\nu_t} P_k - \beta\rho\omega^2 + \underbrace{2\frac{\rho\sigma_{\omega 2}}{\omega} \nabla k \colon \nabla\omega}_{\text{Additional Term}} \tag{A.28}$$

Where $\nabla k \colon \nabla\omega$ is the tensor inner product of the two gradient terms defined as:

$$\nabla k \colon \nabla\omega = \frac{\partial k}{\partial x_j}\frac{\partial \omega}{\partial x_j} = \frac{\partial k}{\partial x}\frac{\partial \omega}{\partial x} + \frac{\partial k}{\partial y}\frac{\partial \omega}{\partial y} + \frac{\partial k}{\partial z}\frac{\partial \omega}{\partial z} \tag{A.29}$$

Therefore, by pre-multiplying that term by a function $(1 - F_1)$ as shown in equation A.30, one can switch between $k - \epsilon$ or $k - \omega$ models and achieve the blending idea previously stated. In fact, when close to the wall, F_1 can be set to be equal to 1 and then the advantages of $k - \omega$ model are exploited, and far from the wall i.e. in freestream conditions, F_1 is set to 0 and then benefit is taken from $k - \epsilon$ turbulence model.

$$2(1 - F_1)\frac{\rho\sigma_{\omega 2}}{\omega} \nabla k \colon \nabla\omega \tag{A.30}$$

The set of transport equations A.20 and A.28 actually lead to the model called $k - \omega$ BST, where BST stands for Baseline Stress Transport.

Now, the decision on how to evolve the value of F_1 remains. It could be done by step functions, linear functions, exponential, etc. However, it is greatly accepted that an hyperbolic tangent function gives a smooth transition between both models, as shown in equation A.31.

$$F_1 = \tanh(arg_1^4) \tag{A.31}$$

Where it is intuitive according to the idea sought through this blending function, that the argument should be somehow a function which depends on the distance to the nearest wall. And so, it is established [44] that the argument follows equation A.32 where d is the distance from the centroid of a cell to the closest wall.

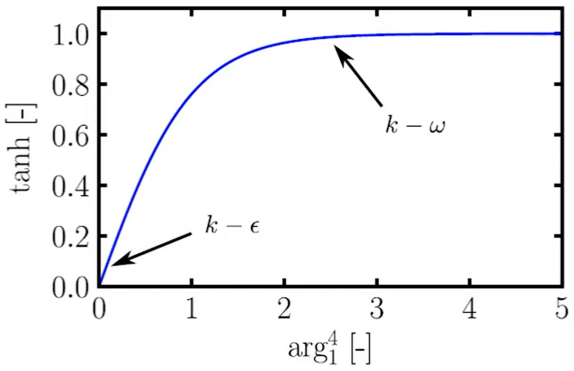

Figure A.5. Graphical representation of F_1

$$arg_1 = min\left[max\left(\frac{\sqrt{k}}{\beta * \omega d}, \frac{500\nu}{d^2\omega}\right), \frac{4\rho\sigma_{\omega 2}k}{CD_{k\omega}d^2}\right] \tag{A.32}$$

Additionally, F_1 can be used also to blend also the empirical constants between both models so the transition is even smoother.

Until here, the deduction of the $k-\omega$ BST has been shown, nevertheless, in the original paper, Menter [45] noticed that on over-prediction of the wall shear stress was still occurring, and therefore he proposed the SST or Shear Stress Transport variant of the model.

In order to extend the BST model to the SST, he introduced a viscosity limiter (eq: A.33) so that, close to the wall where shear stress is higher, it would be damped faster and so, it would not be over predicted if its carefully calibrated.

$$\underbrace{\mu_t = \frac{a_1\rho k}{max(a_1\omega, SF_2}}_{\text{SST Model)}} \tag{A.33}$$

It then appears F_2 which is another empirical blending function equivalent to F_1 in a way that, if the product SF_2 is large, then the viscosity is limited. In order to do it smoothly, it follows also an hyperbolic tangent whose argument depends again in the distance to the wall d (eq: A.34 & eq: A.35):

$$F_2 = \tanh(arg_2^2) \tag{A.34}$$

$$arg_2 = max\left(\frac{2\sqrt{k}}{\beta * \omega d}, \frac{500\nu}{\omega d^2}\right) \tag{A.35}$$

Finally, $k-\omega$ SST model has been proved to give better agreement with the experiments of mildly separated flows [46] and hence, it is best for external aerodynamics or simulations where separation is important as in the crosswind problem that is being assessed throughout this thesis.

A.3 Finite Volume Method (FVM)

A.3.1 Introduction

The Finite Volume Method (FVM) is a very popular way of approaching Computational Fluid Dynamics (CFD) [42] problems thanks to its high flexibility during the discretization process. This characteristic is achieved by the fact that discretization is carried out directly in the physical space without the need of transforming between physical and computational coordinate system. Furthermore, its adoption of a collocated arrangement [41] made it suitable for solving flows in complex geometries.

Navier-Stokes equation as seen in subsection A.1, are a set of partial differential equations in continuous time and space. However, as the computational fluid domain is being divided in N cells, Navier-Stokes equations must be also discretized in some manner. This is approached by the collocation method where a shape matrix premultiplies a system expressed in the form of equation A.36, where $\mathbf{M}$ is a matrix of coefficients.

$$\mathbf{MU} = \mathbf{B} \tag{A.36}$$

This process of discretisation can be performed for any kind of cell, although for the sake of generality, a 3D polyhedral cell will be taken as an example to explain the process.

In the case considered, the method is second order accurate since the quantities are calculated at cell and face centroids and the variation between the value of a variable and its average is of $O(\Delta x^2)$ [42]. Also, flow variables $(\rho, T, \mathbf{U})$ are assumed to vary linearly across the cell.

In addition, another important detail is that it allows a straightforward implementation of a full multigrid strategy thanks to the use of general polygonal elements without any pre-defined shape function.

A.3.2 Integration

The way to proceed on with the method begins with the integration of the Navier-Stokes equation across a certain cell P.

$$\int_V \left[\nabla \cdot (\mathbf{UU}) + \frac{1}{\rho}\nabla p - \nabla \cdot (\nu \nabla \mathbf{U}) - \mathbf{g} \right] dV = 0 \tag{A.37}$$

This integral can be divided into each term and integrated separately.

$$\int_V [\nabla \cdot (\mathbf{UU})] dV = \int_V \left[-\frac{1}{\rho}\nabla p \right] dV + \int_V [\nabla \cdot (\nu \nabla \mathbf{U})] dV + \int_V [\mathbf{g}] dV \tag{A.38}$$

Taking the constant source terms first like gravity, the integration and discretization is straight forward:

$$\int_V \mathbf{g} dV = \mathbf{g} V_p \tag{A.39}$$

$$\mathbf{M}_g \mathbf{U} = \mathbf{B} \tag{A.40}$$

Where gravity is added to the right hand side of the equation, i.e. vector $\mathbf{B}$. However, if the source term does vary linearly with the velocity ($[S\mathbf{U}]$) which may happen with turbulence model as seen for instance in A.2.3, the treatment is different, and the integration goes as follows:

$$\begin{aligned} \int_V [S\mathbf{U}] dV &= S_p \int_V \mathbf{U} dV \\ &= S_p \int_V (\mathbf{U}_p + (\mathbf{x} - \mathbf{x}_p) \cdot (\nabla \mathbf{U}_p)) dV \\ &= S_p \mathbf{U}_p \int_V dV + \underbrace{\left[\int_V (\mathbf{x} - \mathbf{x}_p dV \right]}_{=0} \cdot (\nabla \mathbf{U}_p) \\ &= S_p \mathbf{U}_p V_p \end{aligned} \tag{A.41}$$

As velocity variation across the cell is considered to vary linearly it can be decomposed as shown in step 2, and by splitting the integral, the second term is zero. This is because that second integral is in fact the actual definition of a cell centroid, which is the point under consideration in the finite volume method.

Now, the way of discretizing this term can be done in either an implicit or explicit way. Depends on whether the term $S_P V_P$ is added to the left hand side of equation A.36 (implicit) or the right hand side (explicit).

In the first case, matrix $\mathbf{M}$ would be a diagonal matrix of size $M * M$ with $-S_i V_i$ terms added to the diagonal. The decision to chose an implicit or explicit treatment lays on the weight wanted for the diagonal matrix which is directly related to its stability.

Regarding the convective and diffusive terms of the equation, the procedure is slightly different. For these cases, the divergence theorem, which equation A.42 recalls, is used.

$$\int_V \nabla \cdot \mathbf{F} dV = \int_S \mathbf{F} \cdot \hat{\mathbf{n}} dS \tag{A.42}$$

In fact, taking for instance the convection term and applying the divergence theorem, it can be expressed as in equation A.43, where the outside $\mathbf{U}$ is the unknown variable that is being solved.

$$\int_V [\nabla \cdot \mathbf{U}\mathbf{U} dV = \int_S [\mathbf{U} \underbrace{(\mathbf{U} \cdot \hat{\mathbf{n}})}_{\mathrm{I}}] dS \tag{A.43}$$

Where I is the volume flow rate out of the surface.

The next step would be to compute the surface integral but, as this calculation is not done for a continuous but rather a finite number of elements, the integral can be rewritten as in equation A.44, i.e. the integral is computed for M faces that define the elements as in figure A.6.

$$\int_S [\mathbf{U}(\mathbf{U}\cdot\hat{\mathbf{n}})]dS = \sum_{i=1}^{M}\int_S [\mathbf{U}_i(\mathbf{U}_i\cdot\hat{\mathbf{n}}_i)]dS_i \tag{A.44}$$

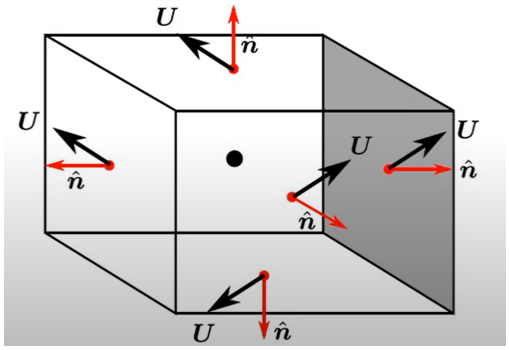

Figure A.6. Volume cell scheme

Then, as proposed by Prof. Jasak [47], instead of computing the integral for the whole face, it is assumed that the variation across the faces is linear and hence, it can be approximated as the value at the face centre leading to equation A.45.

$$\sum_{i=1}^{M}\int_S [\mathbf{U}_i(\mathbf{U}_i\cdot\hat{\mathbf{n}}_i)]dS_i \approx \sum_{i=1}^{M}\mathbf{U}_{fi}(\mathbf{U}_{fi}\cdot\hat{\mathbf{n}}_{fi})S_i \tag{A.45}$$

However, recalling that the finite volume method stores the values of the variable at the cell centroid, it implies that for the owner cell P and the neighbour cell N these values are known for their centroids but not at the face between them which is, indeed, the place at where the equation is being solved (figure A.7).

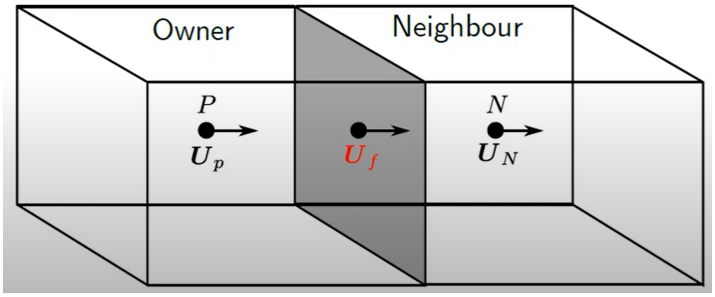

Figure A.7. Owner and neighbour cells scheme

Therefore, some kind of interpolation is needed so that, when interpolating between centroids P and N the corresponding variables, the values needed at the intermediate

faces can be obtained. And so, here is where CFD codes [48,49] provide many different face interpolation schemes like:

1. Upwind
2. Second-order/Linear Upwind
3. Central Differencing
4. QUICK

Once arrived to this point, the equation is reduced to equation A.46 and there transformed into matrix forms as in equation A.36, leading to a matrix $\mathbf{M}$ where cell centroids appear in the main diagonal and face contributions at off diagonal terms.

$$\int_V [\nabla \cdot \mathbf{UU}] dV \approx \sum_{i=1}^{M} \mathbf{U}_{fi} F_{fi} \tag{A.46}$$

To sum up with, this procedure of discretization developed through out the section is then extrapolated not only to classical Navier-Stokes equations but to every variation that may used as RANS model, LES or DNS.

A.4 Solution procedure

A.4.1 Introduction

At this point, it has been introduced how to deal with Navier-Stokes equations, how to approach them and model turbulence. Then, FVM method has been described to give a better insight on how these equations may be translated into a feasible computational domain to tackle the problem. Lastly, it has arrived the point where these equations have to be solved.

In order to do so, there are many ways to approach it. But, although iterative implementations are the ones preferred for nearly every case, also direct methods exist. With regard to iterative algorithms, there are also a few of them like SIMPLE, SIMPLEC, Time marching, PISO, etc [49]. However, for the case at issue, the basic and more generic SIMPLE algorithm has been chosen.

A.4.2 SIMPLE algorithm

Continuity and transport equations from Navier-Stokes for an incompressible flow give 4 equations and 4 unknowns (U_x, U_y, U_z, p) where p is the kinematic pressure (p/ρ). However, for the incompressible case, continuity is not furthermore an equation but rather a restriction that must be satisfied.

Moreover, the convection term in the momentum equations is non-linear and an state equation to compute pressure (e.g $p = \rho RT$) may not be possible to use as density and temperature could be constant.

And so, the scope of the SIMPLE (Semi Implicit Method for Pressure Linked Equations) algorithm relays on the objective of deriving an equation for pressure from the momentum and continuity equations, and derive a corrector for the velocity field so that it satisfies the continuity restriction.

To start with, the momentum equation is rewritten in the general discretized matrix form as seen in section A.3, leading to equation A.47.

$$\mathbf{MU} = -\nabla p \tag{A.47}$$

Recalling how $\mathbf{M}$ was obtained, after adding all the terms from the momentum equation it becomes a matrix with coefficients in the diagonal and off-diagonal terms. Therefore, by following the procedure shown in equation A.48, matrix $\mathbf{M}$ is divided in a diagonal matrix $\mathbf{A}$ and an off-diagonal matrix $\mathbf{H}$.

$$\mathbf{AU} - \mathbf{H} = -\nabla p \tag{A.48}$$

Where $\mathbf{H}$ is:

$$\mathbf{H} = \mathbf{AU} - \mathbf{MU} \tag{A.49}$$

The reason to make this step is that a diagonal matrix is much easier to invert in comparison with a normal matrix. In fact, the inverse of a diagonal matrix is obtained by inverting the each term of the diagonal.

Now, from rearranging the momentum equation A.48, and substituting in the continuity equation one can arrive to the so called Poisson equation for pressure (eq A.50.

$$\begin{aligned} & & \mathbf{U} &= \mathbf{A}^{-1}\mathbf{H} - \mathbf{A}^{-1}\nabla p \\ \nabla \cdot \mathbf{U} = 0 \qquad & & \nabla \cdot [\mathbf{A}^{-1}\mathbf{H} - \mathbf{A}^{-1}\nabla p] &= 0 \\ & & \nabla \cdot \left(\mathbf{A}^{-1}\nabla p\right) &= \nabla \cdot \left(\mathbf{A}^{-1}\mathbf{H}\right) \end{aligned} \tag{A.50}$$

Hence, a system of 4 equations and 4 unknowns is now obtained, although this time with an equation for pressure:

$$\mathbf{MU} = -\nabla p \tag{A.51}$$

$$\nabla \cdot \left(\mathbf{A}^{-1}\nabla p\right) = \nabla \cdot \left(\mathbf{A}^{-1}\mathbf{H}\right) \tag{A.52}$$

The solution process of the algorithm then goes as follows [47, 49]:

1. Initial guess for coefficients in matrix **M** and pressure. Then solve equation A.51 for the velocity field.

2. Solve equation A.52 also known as pressure correction equation as it is the difference between the actual value for pressure and the initial guess.

3. Once the pressure correction field is obtained, the velocity field is corrected so it satisfies the continuity equation deduced at eq. A.50.

4. The velocity field does not satisfy now the momentum equations, therefore, the new values are introduced back at step 1 and the cycle is repeated until convergence criteria is achieved.

Appendix B

CFD results vs Experimental data

B.1 Vivalto

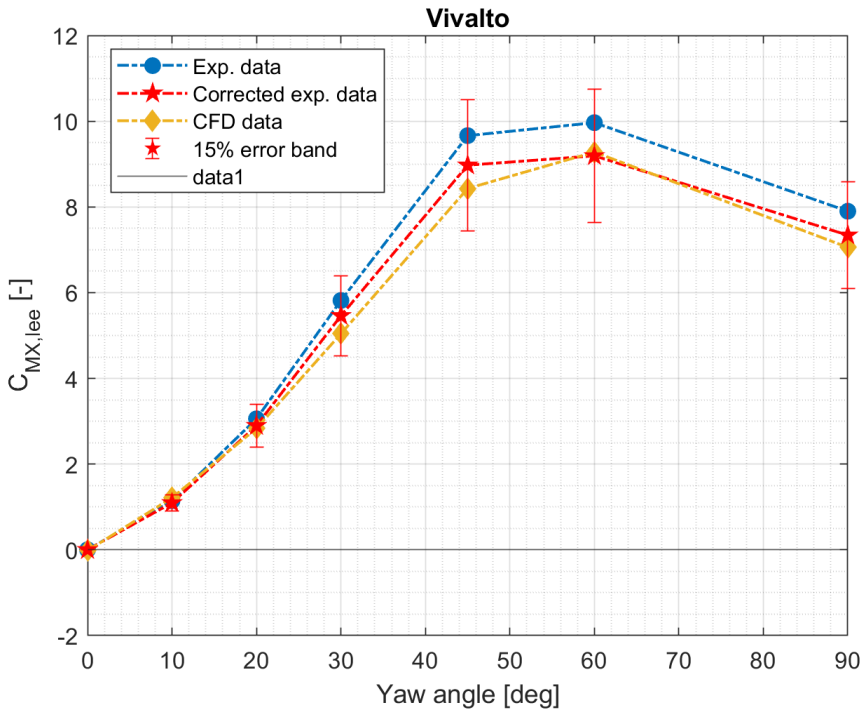

Figure B.1. Vivalto $C_{mx,lee}$ comparison between CFD and experimental data.

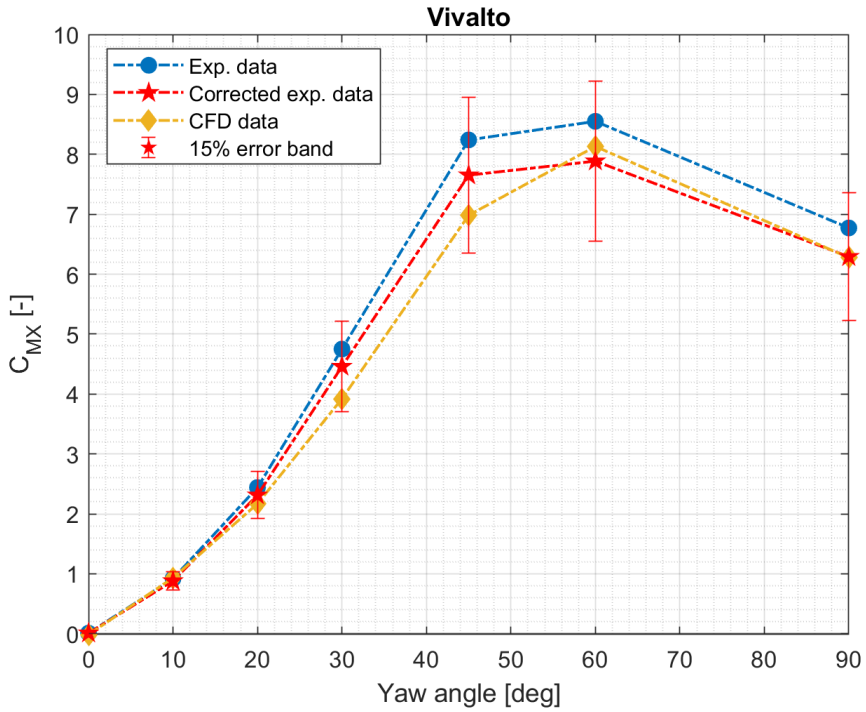

Figure B.2. Vivalto C_{mx} comparison between CFD and experimental data.

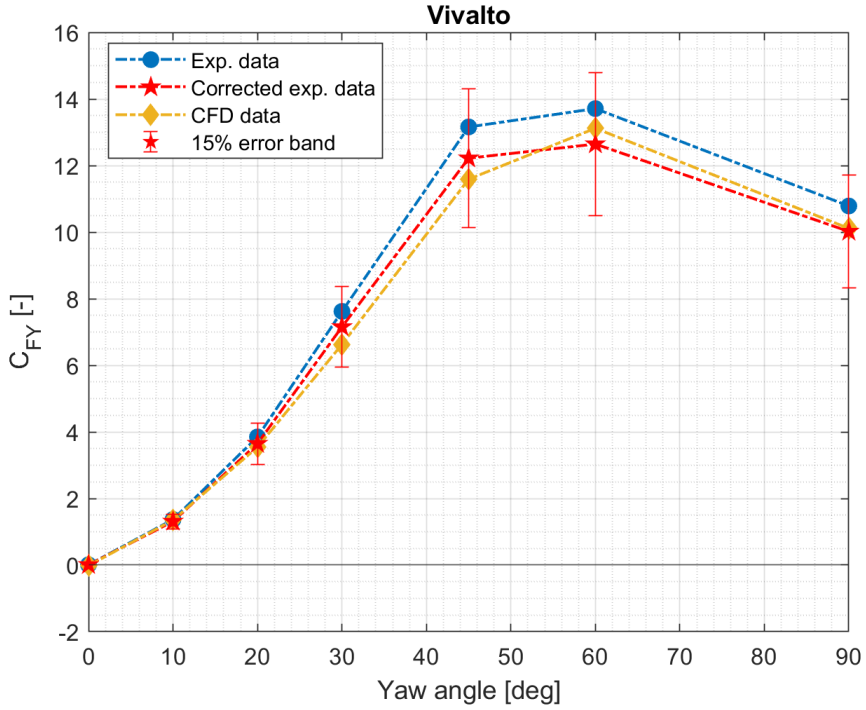

Figure B.3. Vivalto C_{fy} comparison between CFD and experimental data.

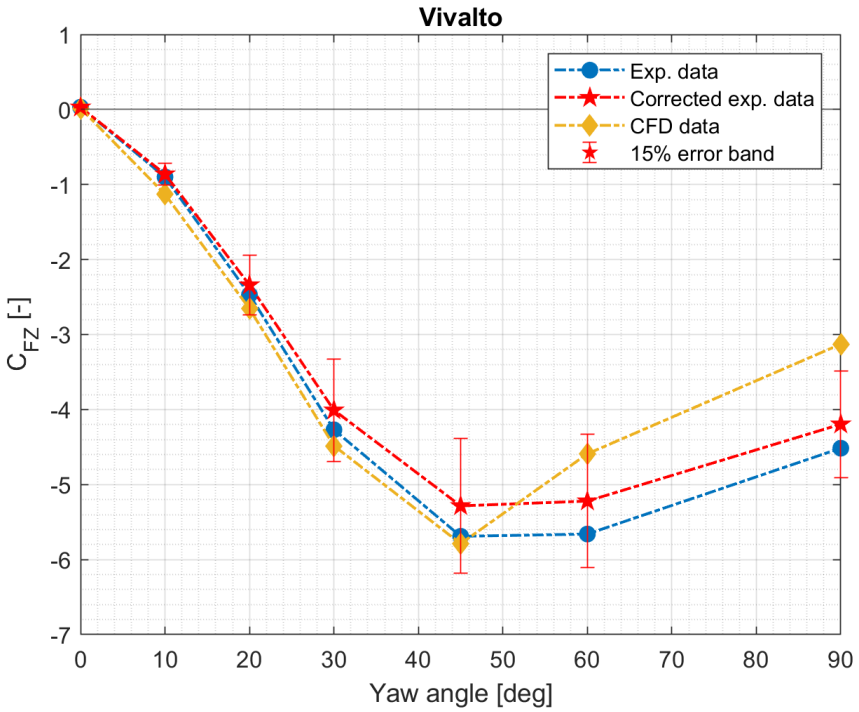

Figure B.4. Vivalto C_{fz} comparison between CFD and experimental data.

B.2 Intercity

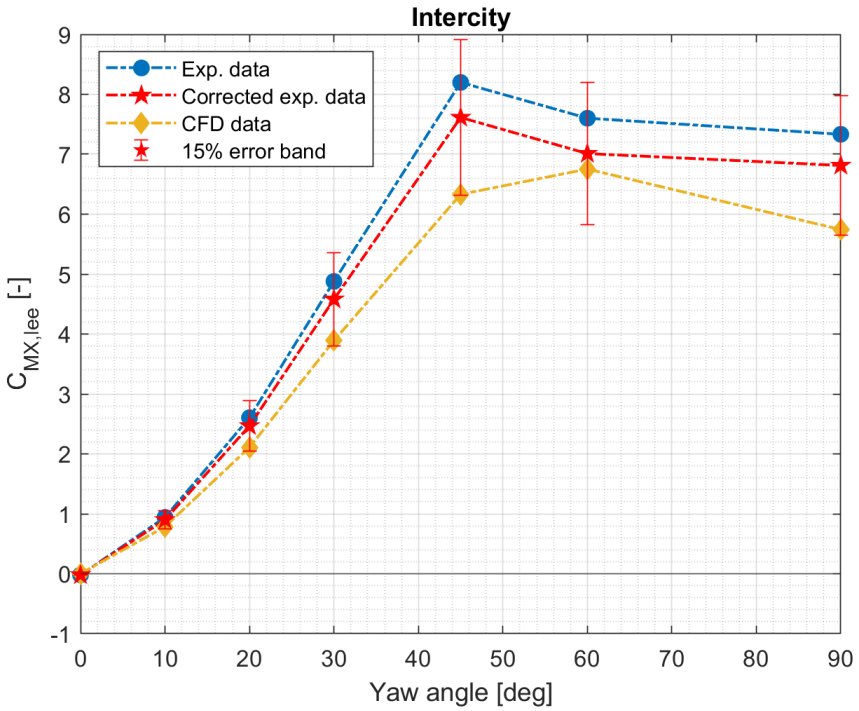

Figure B.5. Intercity $C_{mx,lee}$ comparison between CFD and experimental data.

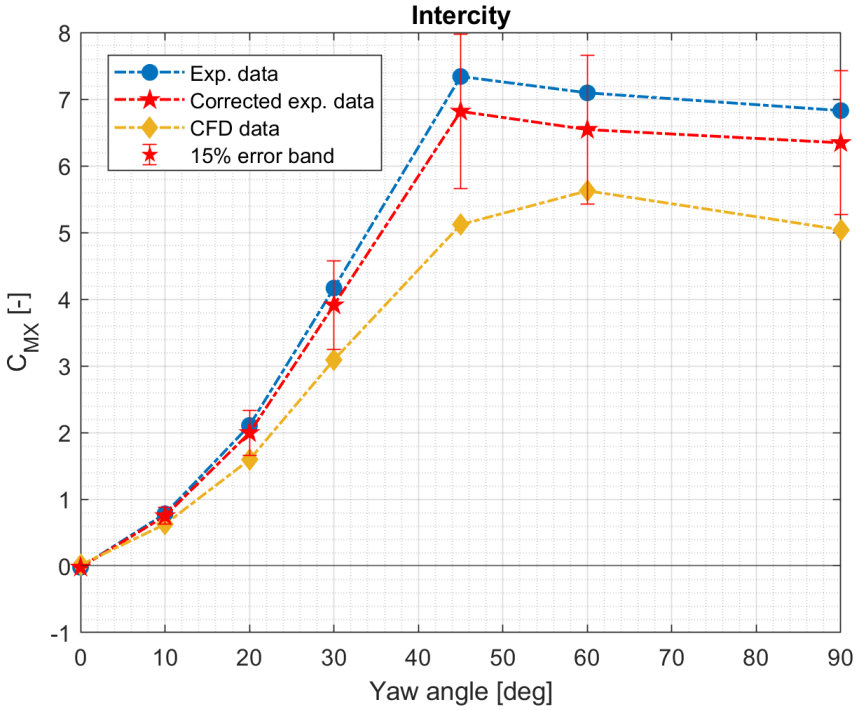

Figure B.6. Intercity C_{mx} comparison between CFD and experimental data.

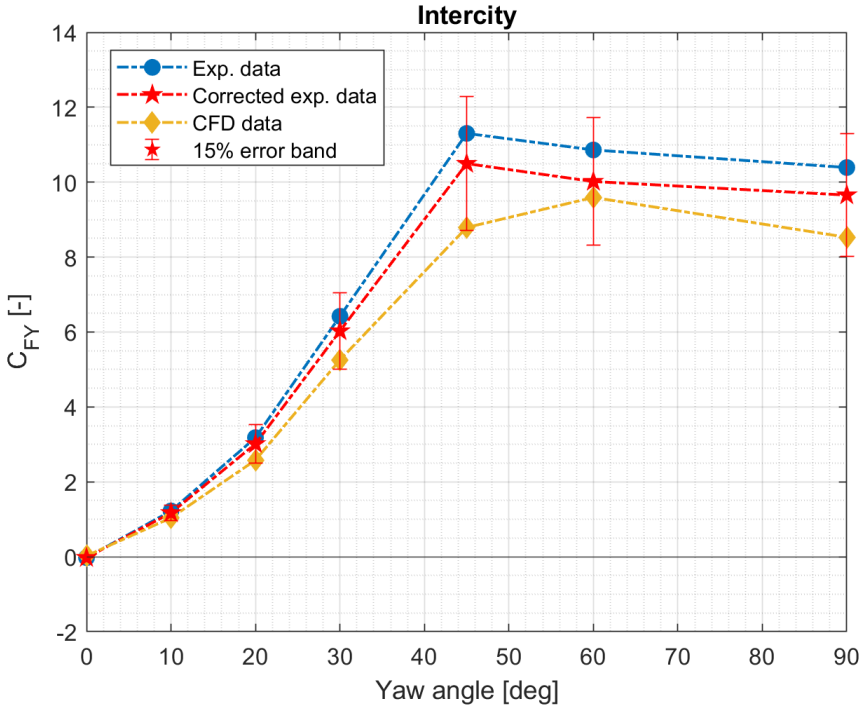

Figure B.7. Intercity C_{fy} comparison between CFD and experimental data.

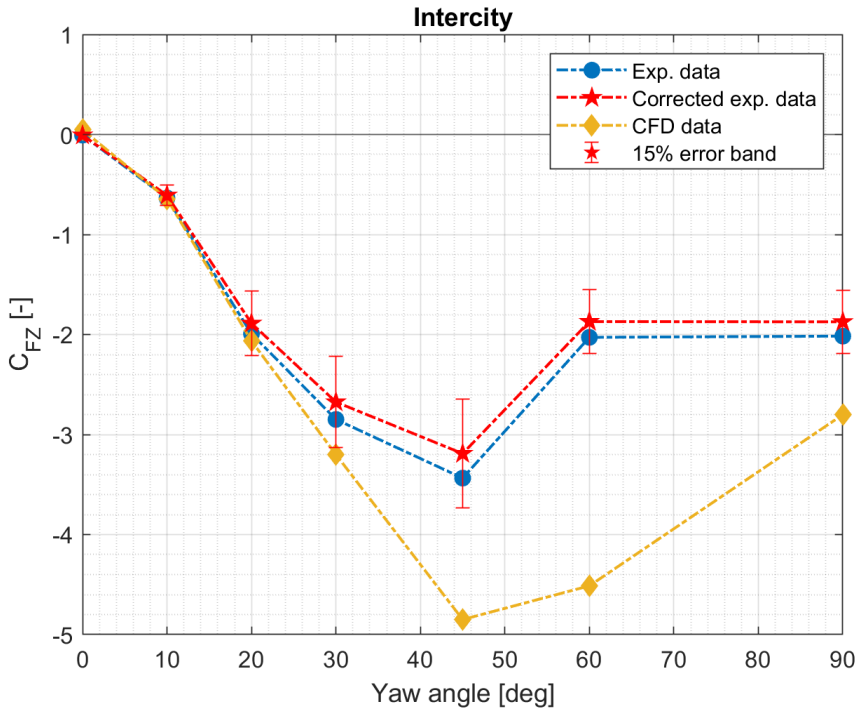

Figure B.8. Intercity C_{fz} comparison between CFD and experimental data.

B.3 Regionale

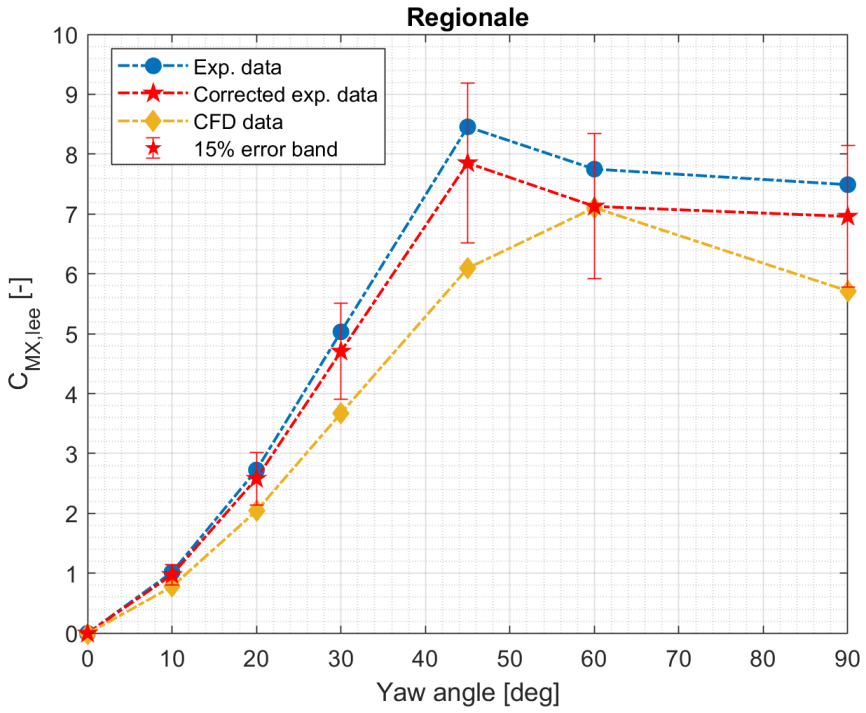

Figure B.9. Regionale $C_{mx,lee}$ comparison between CFD and experimental data.

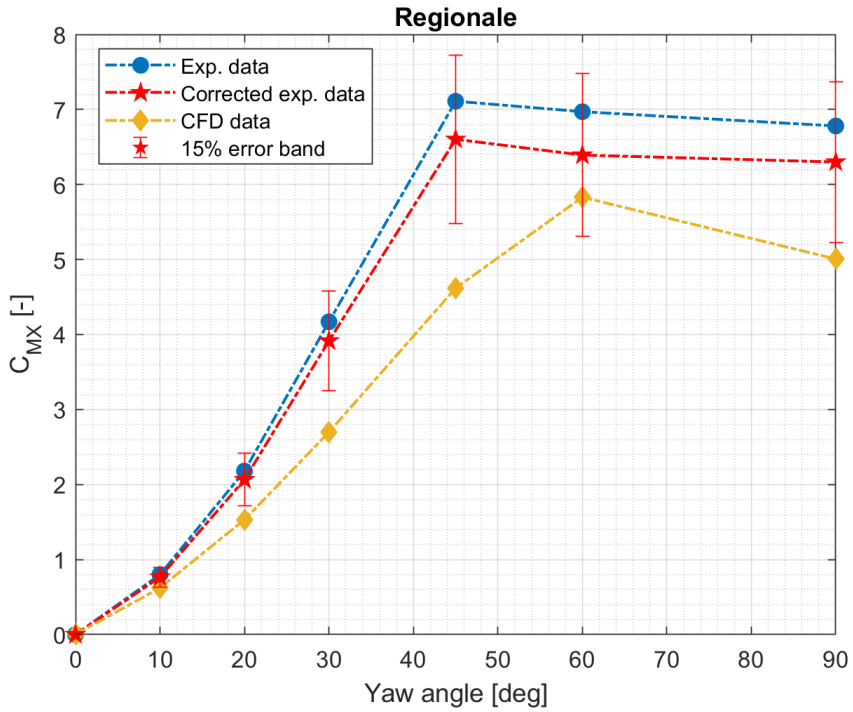

Figure B.10. Regionale C_{mx} comparison between CFD and experimental data.

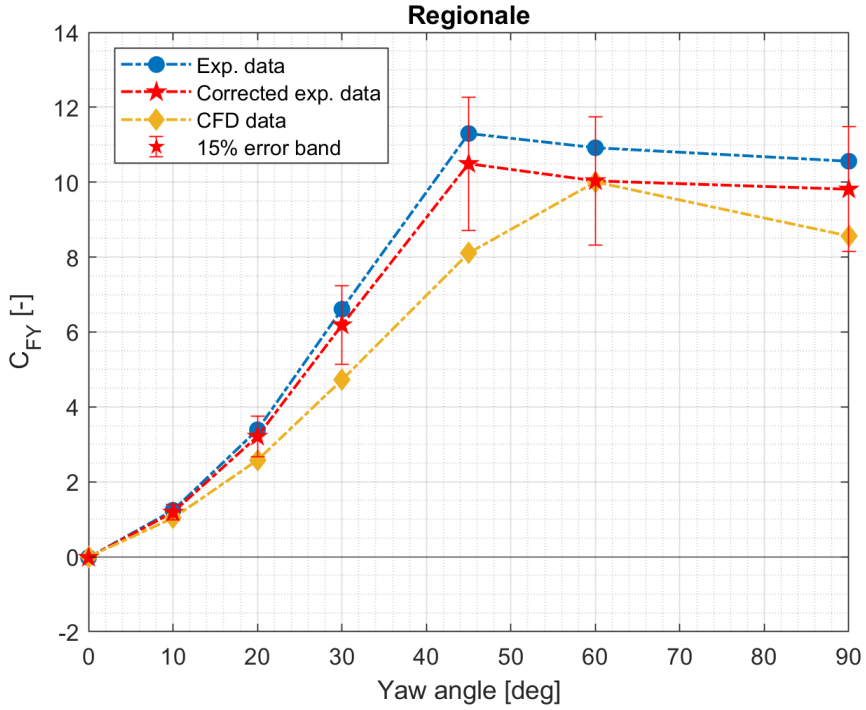

Figure B.11. Regionale C_{fy} comparison between CFD and experimental data.

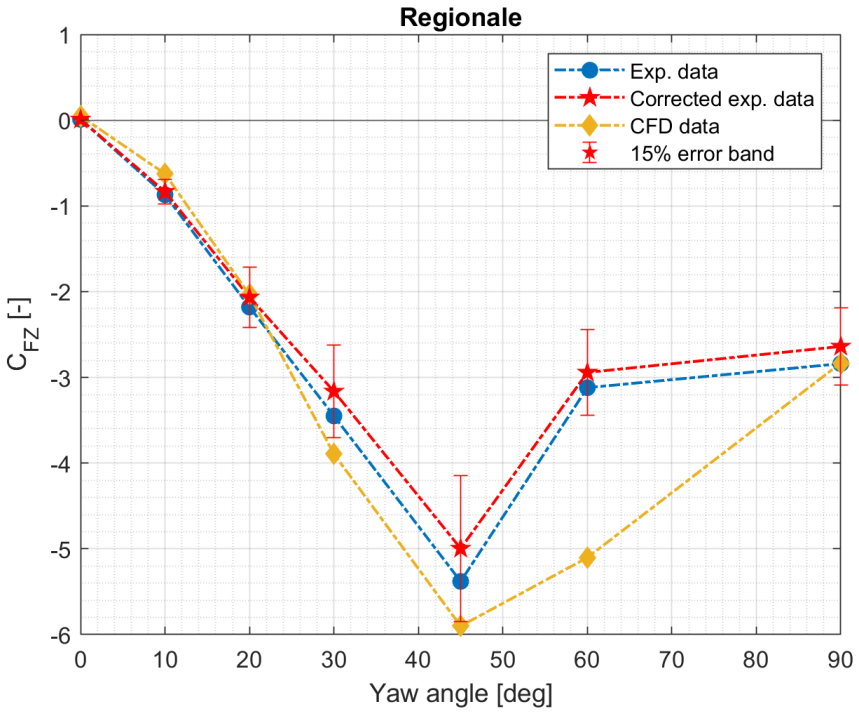

Figure B.12. Regionale C_{fz} comparison between CFD and experimental data.

Appendix C

Extra quantitative results

C.1 Complementary coefficients comparison

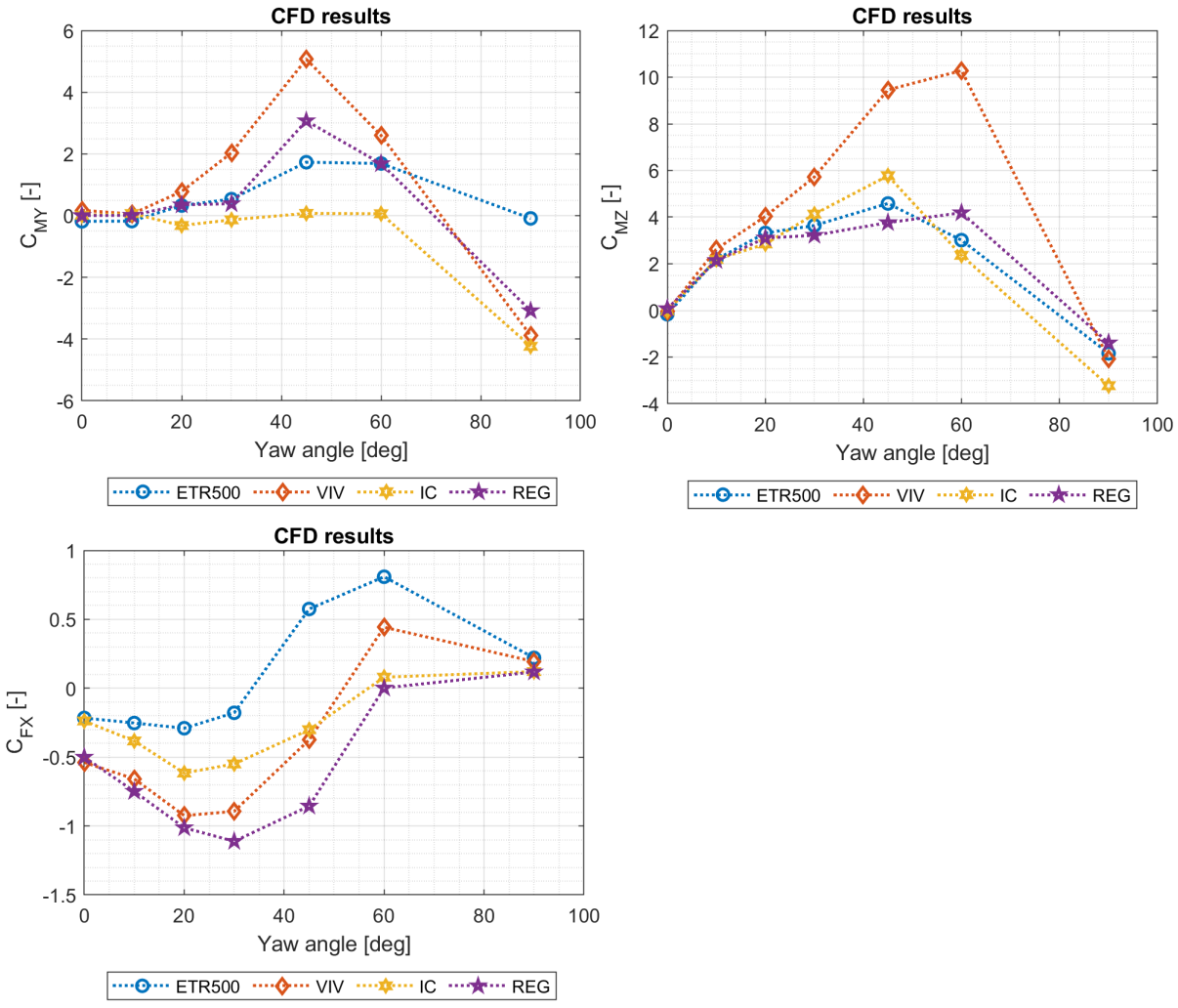

Figure C.1. Additional coefficients C_{MY},C_{MZ} and C_{FX} comparison for every train obtained from CFD data.

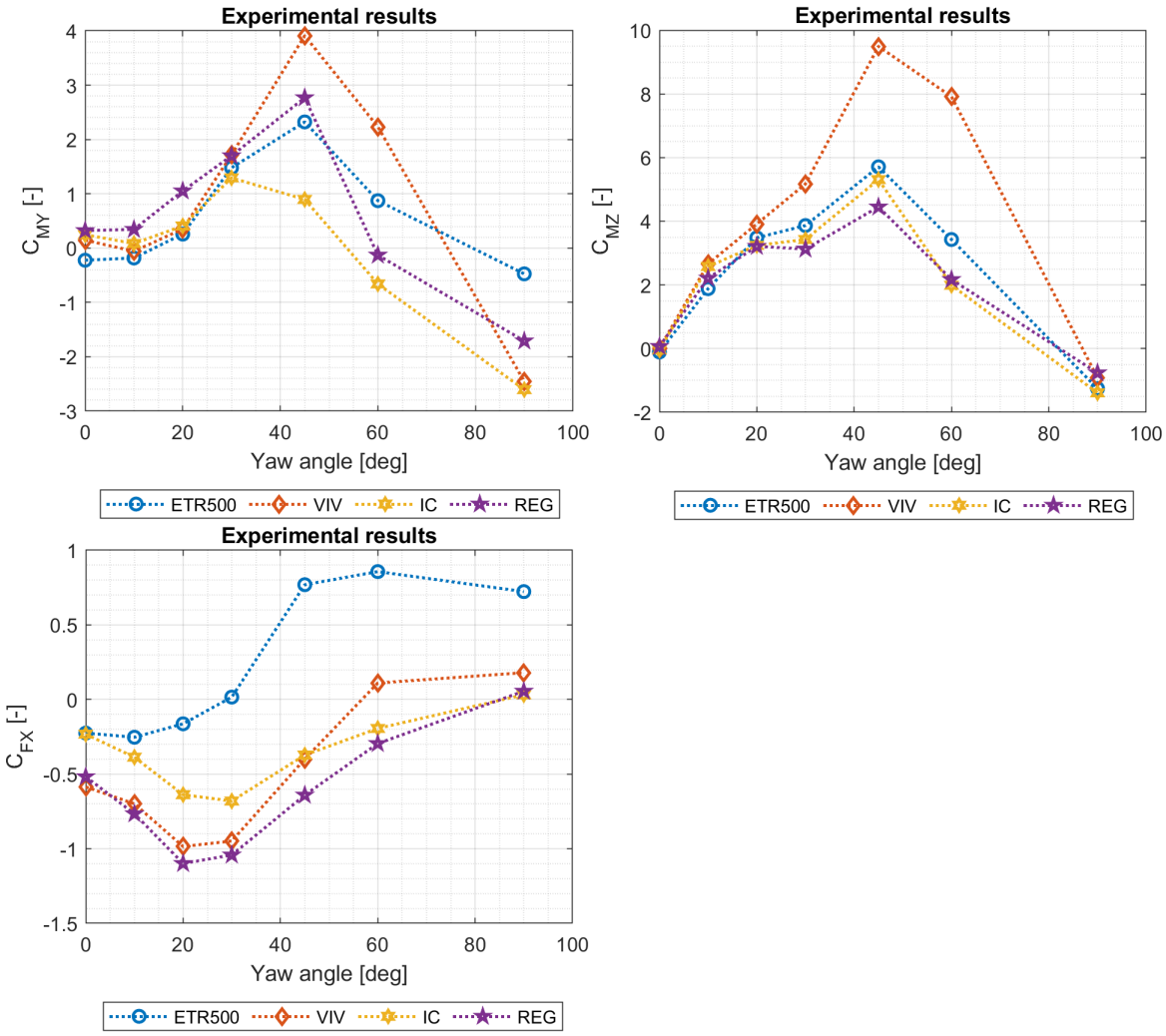

Figure C.2. Additional coefficients C_{MY},C_{MZ} and C_{FX} comparison for every train obtained from experimental data.

Appendix D

Qualitative results

D.1 ETR500 pressure distribution

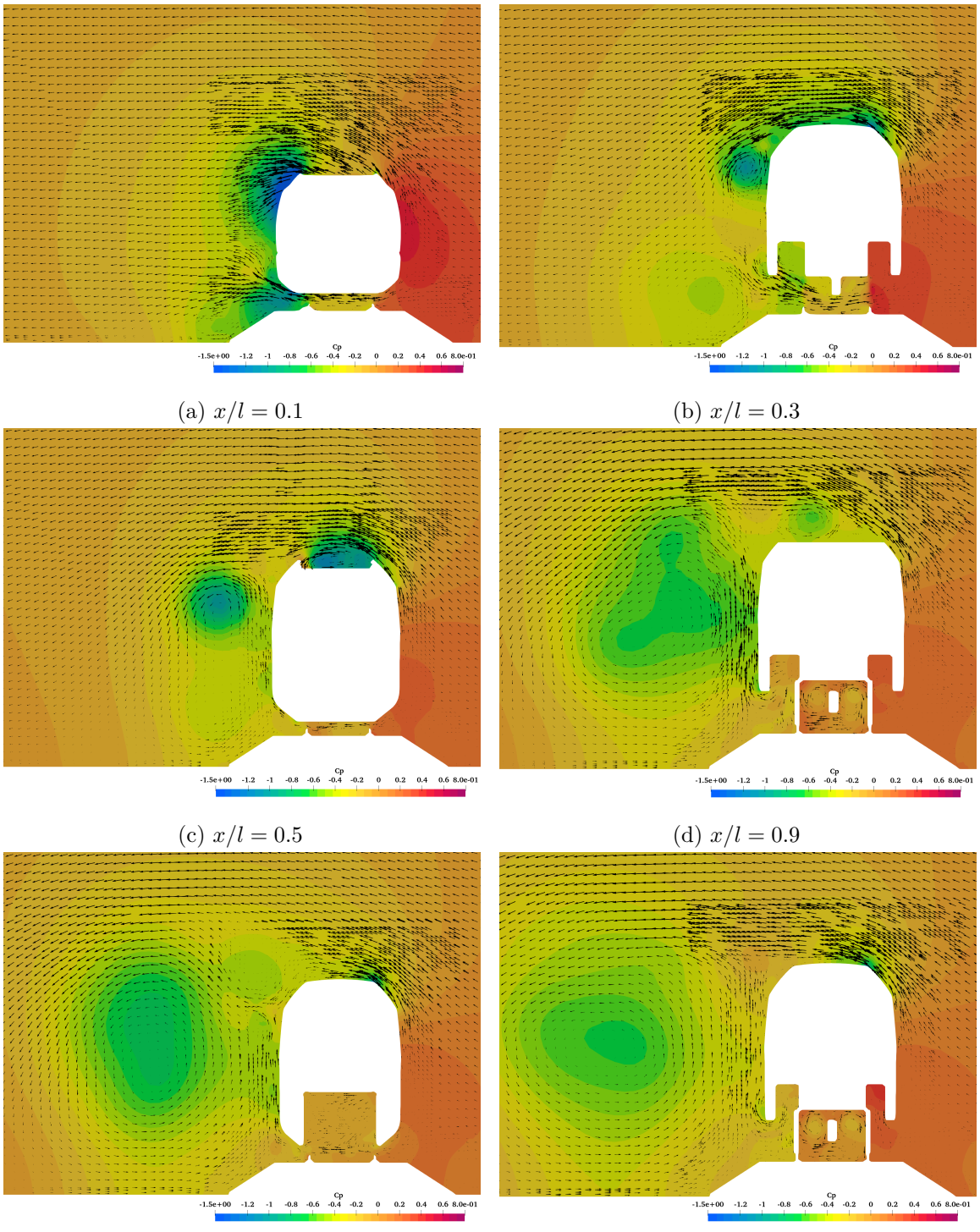

(a) $x/l = 0.1$ (b) $x/l = 0.3$

(c) $x/l = 0.5$ (d) $x/l = 0.9$

(e) $x/l = 1.1$ (f) $x/l = 1.3$

Figure D.1. Vectors of averaged tangential velocity in the y-z plane and contours of pressure coefficient C_p at various lengthwise sections for ETR500 train at $\beta = 30°$.

D.2 Vivalto pressure distribution

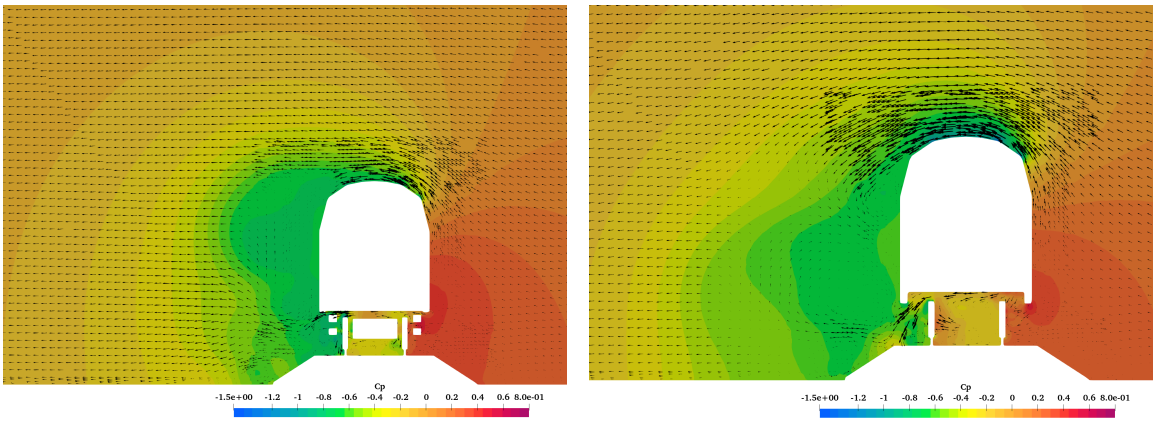

(a) $x/l = 0.1$

(b) $x/l = 0.2$

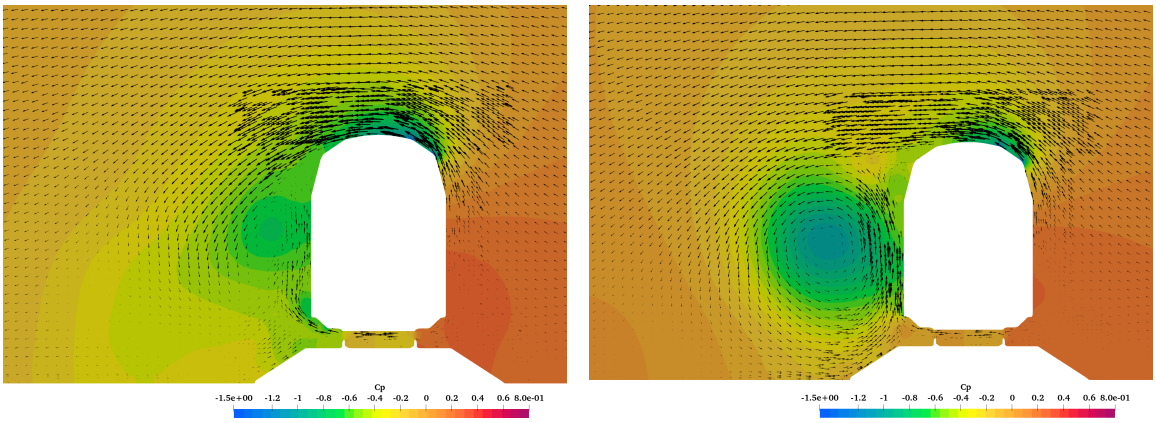

(c) $x/l = 0.3$

(d) $x/l = 0.5$

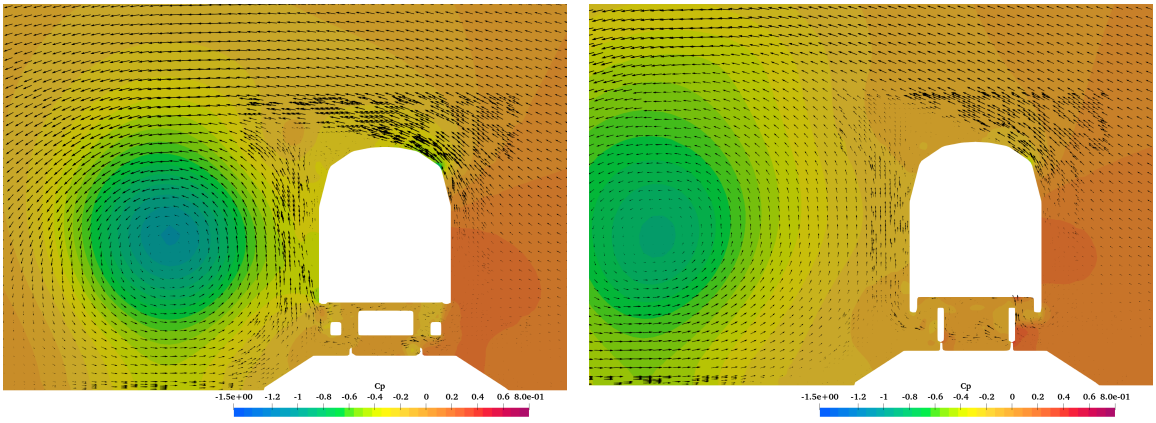

(e) $x/l = 0.9$

(f) $x/l = 1.8$

Figure D.2. Vectors of averaged tangential velocity in the y-z plane and contours of pressure coefficient C_p at various lengthwise sections for Vivalto train at $\beta = 30°$.

D.3 Intercity pressure distribution

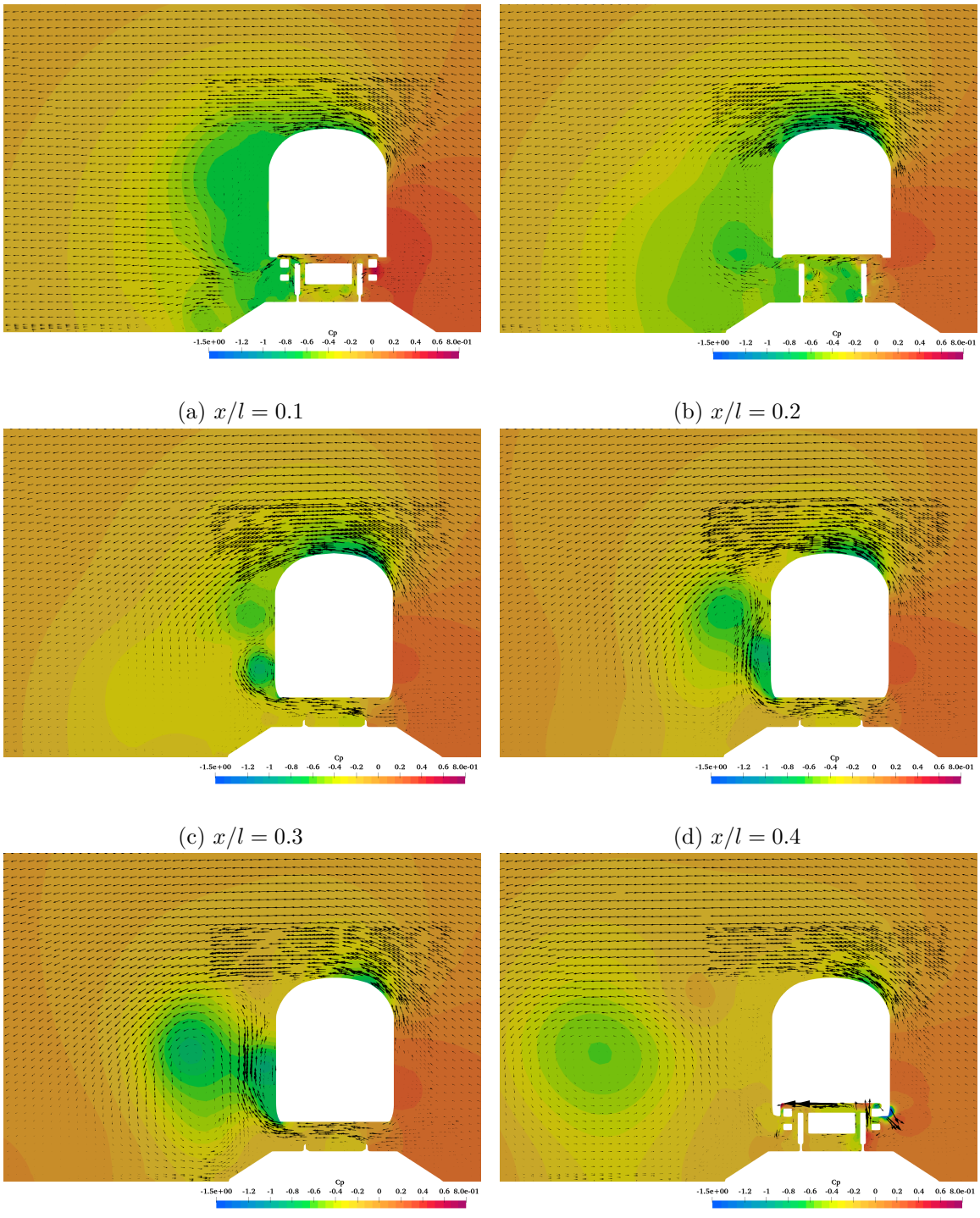

(a) $x/l = 0.1$ (b) $x/l = 0.2$

(c) $x/l = 0.3$ (d) $x/l = 0.4$

(e) $x/l = 0.5$ (f) $x/l = 0.9$

Figure D.3. Vectors of averaged tangential velocity in the y-z plane and contours of pressure coefficient C_p at various lengthwise sections for Intercity train at $\beta = 30°$.

D.4 Regionale pressure distribution

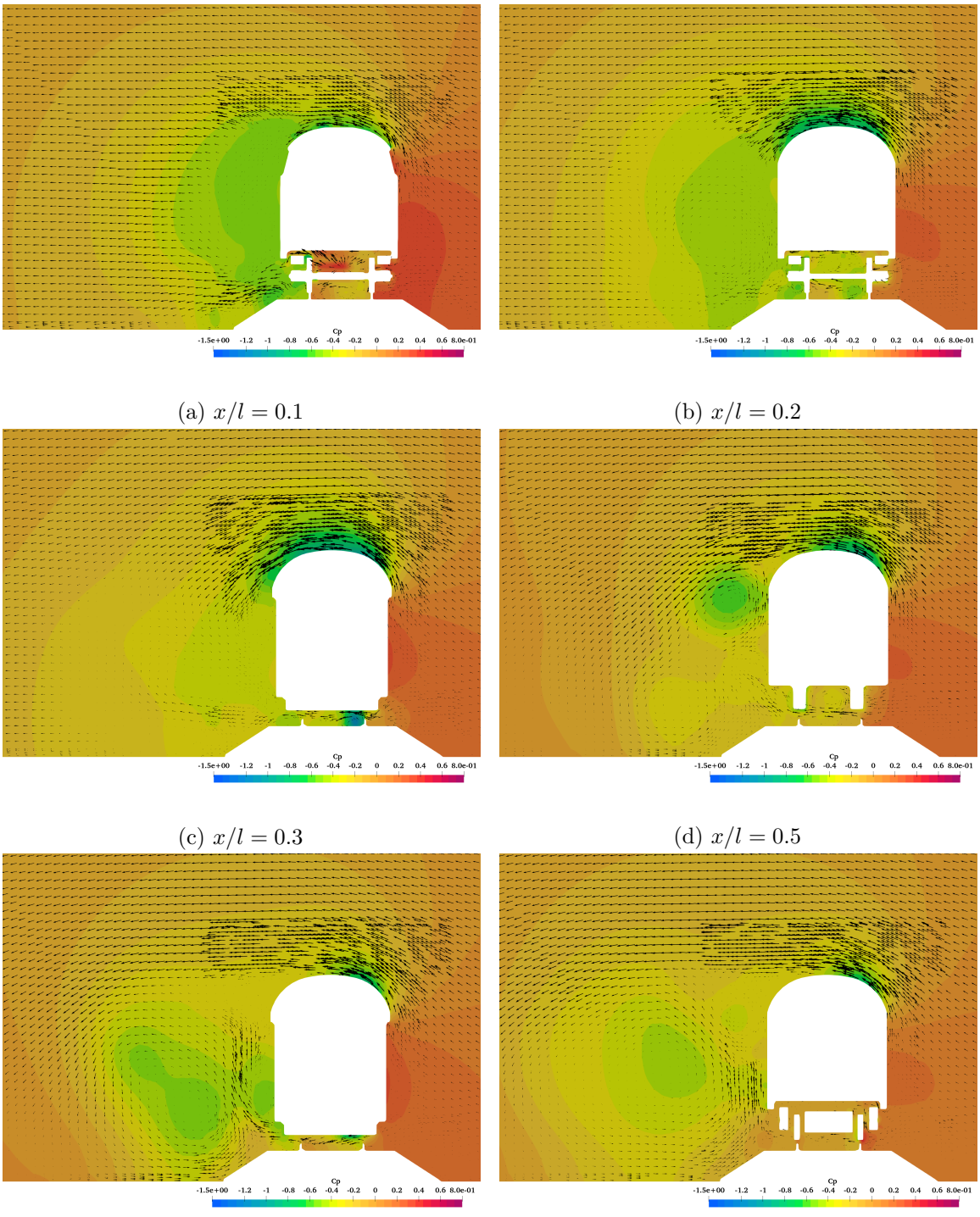

(a) $x/l = 0.1$ (b) $x/l = 0.2$

(c) $x/l = 0.3$ (d) $x/l = 0.5$

(e) $x/l = 0.7$ (f) $x/l = 0.9$

Figure D.4. Vectors of averaged tangential velocity in the y-z plane and contours of pressure coefficient C_p at various lengthwise sections for Regionale train at $\beta = 30°$.

D.5 Leeward surface pressure distributions

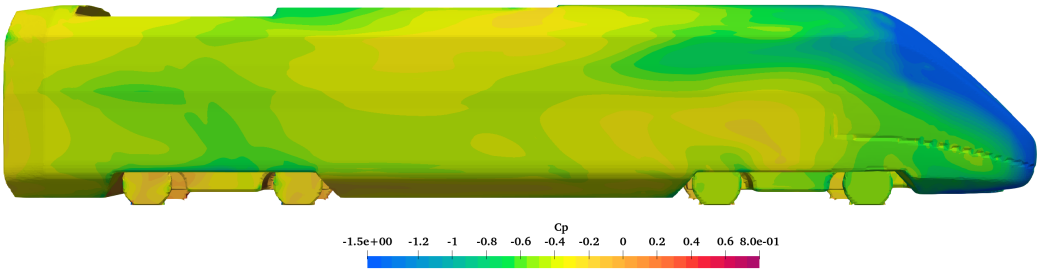

(a) Pressure coefficient C_p distribution at the leeward side of ETR500 at $\beta = 30°$.

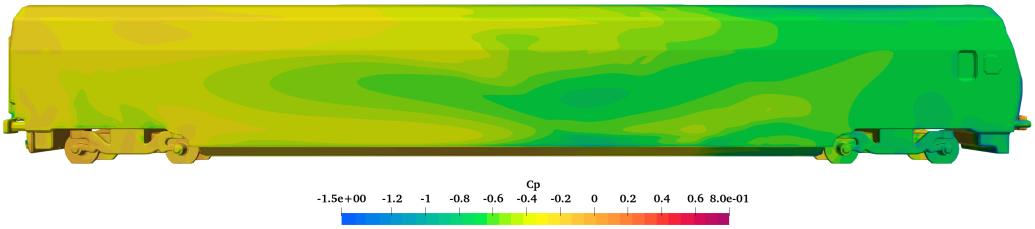

(b) Pressure coefficient C_p distribution at the leeward side of Vivalto at $\beta = 30°$.

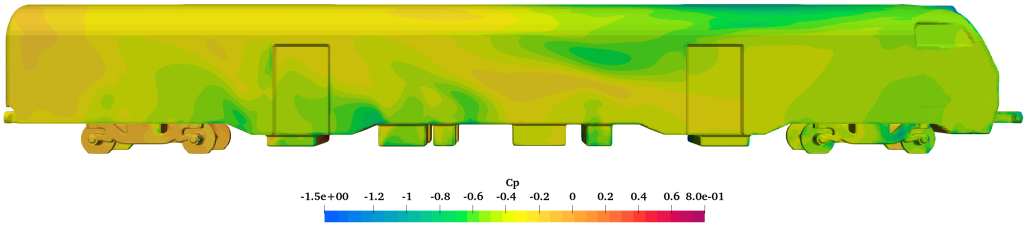

(c) Pressure coefficient C_p distribution at the leeward side of Regionale at $\beta = 30°$.

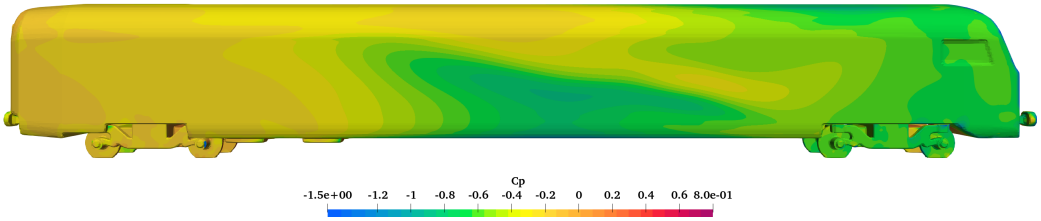

(d) Pressure coefficient C_p distribution at the leeward side of Intercity at $\beta = 30°$.

Figure D.5. Leeward side pressure coefficient C_p distribution for all leading cars at $\beta = 30°$.

Bibliography

[1] Dr. Rolf Naumann Clemens H´oppe Martin grab. Calculation of characteristic wind curves for cross wind curves for cross wind investigations.

[2] Antonio Premoli. *Virtual homologation of high-speed train aerodynamics: experimental and numerical studies.* PhD thesis, Politecnido di Milano, 2015.

[3] W. Khier M. Breuer and F. Durst. Flow structure around trains under side wind conditions: a numerical study. In *Computers & Fluids*, volume 29, pages 179–195. 2000.

[4] Alessandro Zampieri Daniele Rocchi Paolo Schito Claudio Somaschini. Numerical-experimental analysis of the slipstream produced by a high speed train. *Wind Engineering & Industrial Aerodynamics (ELSEVIER)*, 2019.

[5] G. Tomasini S. Giappino F. Cheli and P. Schito. Windbreaks for railway lines: wind tunnel experimental tests. *Rail and Rapid Transit*, 2015.

[6] CJ Baker SJ Dalley T Johnson A Quinn and NG Wright. The slipstream and wake of a high-speed train. In *Proceedings of the Institution of Mechanical Engineers, Part F: Journal of Rail and Rapid Transit*, volume 215 of *2*, pages 83–99, 2001.

[7] N Gil CJ Baker C Roberts and A Quinn. Passenger train slipstream characterization using a rotating rail rig. *Journal of Fluids Engineering*, 132, 2010.

[8] S. Eichinger. Aerotrain wp3-crosswinds. cfd investigations: validated procedures for assessing aerodynamic coefficients., 2012.

[9] W. Khier M. Breuer F. Durst. Flow structure around trains under side wind conditions: a numerical study. *Elsevier*, (29):179–195, 2000.

[10] Lucy M Schiavetta. *Evaluation of URANS and DES Predictions of Vortical Flows over Slender Delta Wings.* PhD thesis, University of Glasgow, 2007.

[11] J. C. Kok. Resolving the dependence on free-stream values for the k-omega turbulence model. *National Aerospace Laboratory NLR*, 1999.

[12] CEN Management Centre. Railway applications - aerodynamics - part 6: Requirements and test procedures for cross wind assessment. Standard, European Committee for Standardization, Avenue Marnix 17, B-1000 Brussels, 2010.

[13] UNI-Milano. Railway applications - aerodynamics - part 1: Symbols and units. Standard, Ente Nazionale Italiano di Unificazione, Via Battistotti Sassi, 11B 20133 Milano, Italia, 2003.

[14] Jones WP Launder BE. The prediction of laminarization with a two-equation model of turbulence. *Int J Heat Mass Transf*, 15:301–314, 1972.

[15] B.E. Launder and D.B. Spalding. The numerical computation of turbulent flows. *Comp. Methods in App. Mech and Engineering 3*, pages 269–289, 1974.

[16] B.E. Launder and B.I. Sharma. Application of the energy dissipation model of turbulence to the calculation of flow near a spinning disc. *Letters in Heat and Mass Transfer*, pages 131–138, 1974.

[17] EC. TSI. Technical specification for interoperability of the transeuropean high speed rail system. Technical report, Official Journal of the European Communities, 2006.

[18] B. Schulte-Werning. Transaero. *Engineering online library*, Springer, 2002.

[19] M. Sima M. Weise. Aerotrain wp2 - analysis report with measurement results and suggestion for standard measurement technique, 2012.

[20] Mulugeta Biadgo Asress & Jelena Svorcan. Numerical investigation on the aerodynamic characteristics of high-speed train under turbulent crosswind. *Springer*, 22(4):225–234, 2014.

[21] Mengge Yu Rongchao Jiang Qian Zhang and Jiye Zhang. Crosswind stability evaluation of high-speed train using different wind models. *Chinese Journal of Mehanical Engineering*, pages 32–40, 2019.

[22] Ben Diedrichs. Aerodynamic calculations of crosswind stability of a high-speed train using control volumes of arbitrary polyhedral shape. In *BBAA VI International Colloquium on: Bluff Bodies Aerodynamics & Applications*, July 2008.

[23] Yueqing Zhuang & Xiyun Lu. Numerical investigation on the aerodynamics of a simplified high-speed train under crosswinds. *Elsevier*, (5):181–186, 2015.

[24] H.J. Kaltenbach and Deutsche Bahn AG Systemtechnik. *DeuFraKo Project "Aerodynamics in Open Air" (AOA): WP 1 Underfloor Aerodynamics ; Summary Report ; Final Report.* Deutsche Bahn, 2008.

[25] H.J. Kaltenbach P.E. Gautier G. Agirre A. Orellano K.Schoroeder-Bodenstein M. Testa Th. Tielkes. *Assessment of the aerodynamic loads on the trackbed causing ballast projection: results from the DEUFRAKO project Aerodynamics in Open Air (AOA).* Deutsche Bahn, 2008.

[26] P.-E. Gautier T. Tielkes F. Sourget E. Allain M. Grab & C. Heine. Strong wind risks in railways: the deufrako crosswind program. In *Proceedings of the World Congress of Railway Research (WCRR)*, pages 463–475, 2003.

[27] Chris Baker. Special issue: Aerotrain anddynotrain projects. *Journal of RAIL AND RAPID TRANSIT*, 229(6):567–569, 2015.

[28] Sándor Eichinger Mikael Sima Frank Thiele. Numerical simulation of a regional train in cross-wind. *Journal of RAIL AND RAPID TRANSIT*, 229(6):625–634, 2015.

[29] S.Eichinger M.Sima A.Blanco I.Ali. Computational fluid dynamics simulation of rail vehicles in crosswind: Application in norms and standards. *Journal of RAIL AND RAPID TRANSIT*, 229(6):635–643, 2015.

[30] N.Paradot R. Grégoire M. Stiepel A. Blanco M. Sima P. Deeg K. Schroeder-Bodenstein T. Johnson G. Zanetti. Crosswind sensitivity assessment of a representative europe-wide range of conventional vehicles. *Journal of RAIL AND RAPID TRANSIT*, 229(6):594–624, 2015.

[31] Gallagher M. Morden J. Baker C. Soper D. Quinn A. Hemida H. Sterling M. Trains in crosswinds – comparison of full-scale ontrain measurements, physical model tests and cfd calculations. *Journal of Wind Engineering & Industrial Aerodynamics*, 175:428–444, 2018.

[32] M. Bocciolone F. Cheli R. Corradi S. Muggiasca and G. Tomasini. Crosswind action on rail vehicles: wind tunnel experimental analyses. *Journal of Wind Engineering and Industrial Aerodynamics*, 96(5):584–610, 2008.

[33] Wang B. Xu Y.-L. Zhu L.-D. Li Y.-L. Crosswind effects on high-sided road vehicles with and without movement. *Wind Struct. Int. J.*, 18:155–180, 2014.

[34] I.G. Currie. *Fundamental Mechanics of Fluids.* Marcel Dekker, Inc, 2003.

[35] Stephen B. Pope. *Turbulent Flows.* Cambridge University Press, 2000.

[36] H. Tennekes John L. Lumley. *A First Course in Turbulence.* MIT Press, 1972.

[37] Kolmogorov. *The local structure of turbulence in incompressible viscous fluids at very large Reynolds numbers.* Doklady, 1941.

[38] Kolmogorov. *Dissipation of energy in isotropic turbulence.* Doklady, 1941.

[39] Sagaut P. *Large eddy simulation for incompresiible flows. An introduction.* Springer, 2006.

[40] P. R. Spalart W. H. Jou Mikhail Kh Strelets and S. R. Allmaras. Comments on the feasibility of les for wings and on a hybrid rans/les approach. *In Advances in DNS/LES*, 1, 1997.

[41] Reynolds O. *On the dynamical theory of incompressible viscous fluids and the determination of the criterion.* Philos Trans Royal Soc London, 1895.

[42] F.Moukalled L.Mangani M.Darwish. *The Finite Volume Method in Computational Fluid Dynamics. An Advanced Introduction with OpenFOAM and Matlab.* Springer, 2016.

[43] F. R. Menter. Influence of freestream values on k-omega turbulence model predictions. *AIAA Journal*, 30, 2012.

[44] Christopher Rumsey. Nasa langley research centre - turbulence modelling resource.

[45] F. R. Menter. Two-equation eddy-viscosity turbulence models for engineering applications. *AIAA Journal*, 32:1598–1605, 1994.

[46] Apsley D.D. Leschziner M.A. Advanced turbulence modelling of separated flow in a diffuser. *Flow, Turbulence and Combustion*, 63:81–112, 2000.

[47] H. Jasak. *Error Estimation and Analysis for the FInite Volume Method with Application to Fluid Flows*. PhD thesis, Imperial College London, 1996.

[48] *ANSYS FLUENT User Manual*. 25.3.1 Spatial Discretisation.

[49] *OpenFOAM guide*. The SIMPLE algorithm in OpenFOAM.

[50] Jr. John D. Anderson. *Fundamentals of AERODYNAMICS*. McGraw-Hill Series in Aeronautical and Aerospace Engineering, 2011.

[51] Ahmed Osama Mohamed Elhassan MAHGOUB. Numerical study of the vortical flow over a reverse delta wing. Master's thesis, Politecnico di Milano, 2018.

[52] Vivianne Holmen. Methods for vortex identification, 2012.

[53] Russell M. Cummings Scott A. Morton and David R. McDaniel. Experiences in accurately predicting time-dependent flows. *Progress in Aerospace Sciences*, 44:241–257, 2008.